DIVISION OF
FLUID, THERMAL AND AEROSPACE SCIENCES

SCHOOL OF ENGINEERING

CASE WESTERN RESERVE UNIVERSITY

UNIVERSITY CIRCLE • CLEVELAND, OHIO 44106

NASA CR-72893

FTAS/TR-71-62

EXPERIMENTS ON A TURBULENT JET IN A CROSS FLOW

by

Yasuhiro Kamotani and Isaac Greber

NASA CR-72893 FTAS/TR-71-62

Case Western Reserve University

June 1971

ABSTRACT

Results are reported of experiments on turbulent circular jets issuing into a cross flow, both for unheated and heated jets. Longitudinal and transverse distributions of velocity, pressure, temperature, and turbulence intensity are presented.

The velocity distributions depend on the ratio of jet to cross flow momentum flux. The temperature distributions depend also on the density ratio. The jet structure is dominated by a vortex wake which forms behind the jet, which is evident both from the detail measurements and from smoke photographs of the flow. The experiments also indicate that the components of cross flow normal and parallel to the jet trajectory independently control the entrainment rate.

ACKNOWLEDGMENTS

The authors wish to acknowledge the inception of this work by the late Dr. H. K. Wiskind. They also acknowledge the financial support of the National Aeronautics and Space Administration through Grant NGR-36-027-008.

TABLE OF CONTENTS

LIST OF FIGURES

I. INTRODUCTION

In recent years considerable attention has been given to the problem of jets issuing into a subsonic cross flow. This is mainly because it is the basic configuration in many practical situations. In general the point of main interest is different in each case. Main fields of application and their associated problems can be summarized in the following list.

1. V/STOL aircraft use air jets to obtain lift for take-off. During transition flight these jets are bent rearward, which changes the air flow around the aircraft body, causing a loss in lift and instability due to pitching moment. Choosing the number of jets and their locations are the most important problems in order to get maximum performance of the aircraft.
2. A hot stream of gas in a pipe or in a duct can be cooled simply and effectively by injecting jets of cool gas into it. In order to get a desired temperature distribution at a given section downstream of the jets, it is necessary to study the mixing of two flows.
3. A plume leaving a chimney with substantial upward momentum is often bent by a cross wind (bent-over plume). In this air pollution problem it is important to calculate the ground level concentration for a given situation. It is customary to apply a suitable diffusion formula from a certain point at which the upward momentum of the plume is negligible. The analysis of a jet in a cross flow can be applied to find the

flow structure near this point as well as its location.

4. A river with some contaminant materials, flowing into the ocean or the lake with cross current, presents another problem of diffusion. In this case the main interest is in finding the polluted region and the degree of pollution (concentration distribution).

The present study was motivated by the cooling problem. The temperature of hot combustor gas for a gas turbine is generally too high for the material used, and it needs to be cooled. Generally, cooling is done by injecting cool air through holes in the surrounding wall. Although multiple jets are used for effective cooling, a single jet case is treated here as a first step. The results obtained give basic information not only for the combustor cooling problem but also for many other applications.

Quite a few papers have appeared in the last decade concerning the experimental and the analytical studies of a jet in a cross flow. They studied mainly the over-all behavior of the jet such as the jet centerline location. In Chapter 2 these previous works are summarized together with some basic discussions. Compared with such general aspect of the jet, its detail structure has not been thoroughly investigated. Therefore, it was felt that instead of going into the cooling problem directly, it was necessary to investigate first the detail aspect of the jet injected into a cross flow of equal temperature, which is essential in order to understand the mixing process.

To show the jet structure in detail, distributions of velocity, pressure and turbulence intensity were measured at several sections of the jet. The data revealed a complex structure of the jet. The structure was found to be strongly influenced by a pair of counter-rotating eddies which were formed behind the jet. Thus the rotational velocity field was also investigated in detail.

After this unheated jet experiment, the mixing of two flows with different temperature was studied. To do this, the jet was heated above the free stream temperature instead of cooled as in the cooling problem, because experimentally it was easier to get large enough temperature difference by heating. Although buoyancy force acts in the opposite directions in heated and cooled jets, it does not change the general flow characteristics significantly. The jet was heated up to 400°F. Lateral distributions of temperature at several jet sections and the longitudinal distribution along the centerline were measured in detail to study the mixing of two flows. All of the experimental results are presented in Chapter 5. The discussion based on these data is given in Chapter 6.

In addition to these experiments, a flow visualization experiment using kerosene smoke was conducted. The pictures presented in Chapter 7 show clearly the cross-sectional shape of the jet in a cross flow.

II. GENERAL DISCUSSION

1. Brief Review of Previous Work

Since the present flow is the basic configuration in many practical situations, numerous papers have been published. The problems they treated can be classified mainly into three groups. The first group concerns the determination of the jet centerline location either experimentally or analytically. The second group treats the problems relating to V/STOL aircraft. The third group investigates theoretically the rolling-up of a jet due to a cross flow.

Several forms of the jet centerline equation have been suggested. Some of these are empirical, and others are obtained by semi-empirical analyses. The latter usually contain several numerical constants which have to be determined from the experimental data. Some of the early works have been mentioned in Ref. 1. The recent work has been reviewed in Ref. 2 and 3. Some of these works will be mentioned elsewhere in this report. Several jet centerline equations reviewed in Ref. 2 show quite a scatter (see also Fig. 54 of this report). Carlson et al. (Ref. 3) tried to correlate some of the previously published data taking into account the different wind tunnel sizes relative to the jet sizes in the different experiments.

To analyze the jet deflection due to the cross flow, two important factors have to be considered. One is the aero-dynamical force acting on the jet, and the other is the entrainment of the non-turbulent main stream into the jet. Most of the analytical models

consider only the former factor (Refs. 1, 4, 5). As the entrainment idea developed in recent years, it was realized that the effect of the entrained momentum on the jet deflection is more important except for the region close to the nozzle where the aerodynamical force is just as significant (Ref. 6). A few investigators obtained the jet centerline equation by considering the entrainment effect only (Ref. 7).

In applications to V/STOL aircraft, the most important factor is the pressure distribution on the plate surface. Experimental data for the surface pressure distribution were given in several papers (e.g. Refs. 8, 9, 10). Theoretical analysis of the problem has also been presented by some investigators. The calculation made by Wu et al. (Ref. 10) was based on the simple two-dimensional potential flow model, and it gave reasonably satisfactory agreement with the measured wall pressure distribution.

Recently theoretical analyses of the jet rolling-up process have been presented by several authors (e.g. Ref. 11). Their analysis is an extension of the early work by Chang (Ref. 12). Chang considered the time-dependent deformation of the cross-section of the hypothetical circular fluid column in a cross flow. In this analysis the original jet is replaced by a number of vortex filaments distributed along the jet surface; by following the location of these filaments as time goes on, instantaneous cross-sectional shape can be obtained. Since such analysis shows only the potential flow aspect of the interaction of two flows, the

result cannot be compared with the data which are taken usually in a turbulent flow.

Perhaps most directly related to the present work are the experiments of Keffer and Baines (Ref. 6), Callaghan and Ruggeri (Rep. 13, 14, 15), and Jordinson (Ref. 16). Keffer and Baines made measurements in the plane of symmetry in the upstream region ($\bar{x}/D < 10$) for unheated jets. Their experiments tend to show the importance of the momentum ratio in determining the jet trajectory. They also studied entrainment, making an analytical model which is a simple extension of the free jet model. This is satisfactory because they were only concerned with the small $\bar{x}$ region. Callaghan and Ruggeri made measurements using a heated jet. Their measurements also were only in the plane of symmetry, and their jet was rather closely confined because of their small wind tunnel width (3.1 to 7.8 nozzle diameters). Jordinson measured total pressure distributions for the full lateral extent of the jet, not only in the plane of symmetry. Recent developments in most of the problem discussed above are reported in Ref. 17.

To provide an adequate understanding of the behavior of a jet in a cross flow, the present work examines the detailed lateral distributions of velocity, temperature and turbulence intensity, both in the upstream and downstream regions of the jet. Longitudinal distributions of the above quantities, ideas about entrainment, and the role of the vortex motions are deduced from the extensive lateral measurements.

2. Coordinate System

Figure 1 shows the coordinate system adopted in the present work. The Cartesian coordinate system (x , y , z) with the origin at the center of the nozzle exit is convenient for practical applications. The x -axis is the direction of the cross flow, the z -axis is the direction of jet injection, and the y -axis is perpendicular to both. On the other hand for the purpose of analytical study, it is more convenient to use the coordinate which follows the deflected path of the jet. For this, the natural coordinate system based on the mean streamlines is most suitable. However, it is very difficult to determine this system experimentally. The coordinate system (s , η , ζ) adopted here is somewhat similar to the natural one. s is measured along a jet velocity centerline, which is one of the mean streamlines in the jet. The plane normal to this streamline at each point of s is assumed to represent the cross-section of the jet. Therefore the s -axis (jet centerline) can be determined experimentally by connecting points of maximum velocity at each section in the plane of symmetry (xz-plane with $y = 0$). On each normal plane the η -axis is taken to be in the direction of the y -axis from the jet center (thus $y = \eta$), and the ζ -axis is perpendicular to the η -axis.

3. Dimensional Analysis

Because of the complicated configuration of the problem a purely theoretical analysis is very difficult, and it is beyond the scope of the present study. However, it is very useful for the experiment to find important dimensionless numbers by simple dimensional analysis.

Consider a heated (or cooled) jet issuing normally to a uniform flow. As the flow develops the jet becomes turbulent. Some mean quantity $\overline{Q}$ at some point downstream of the nozzle can be considered to be a function of the following quantities:

$$\overline{Q} = (x, y, z, D, U_0, U_j, P_0, P_j, T_j - T_0, \rho_0, \rho_j, \mu, k, C_p)$$

where subscripts 0 and j denote the properties of the cross flow and the jet, respectively. The free stream and the jet are considered to be the same fluids (no subscript for μ , k , C_p). In this analysis, only the case in which both the initial jet and the cross flow are laminar as in the present experiment is discussed. The effect of the surrounding wall is assumed to be negligible. Then important dimensionless groups formed from quantities listed above are expected to be as follows.

$$\frac{\overline{Q}}{\overline{Q}_{ref}} = \left(\frac{x}{D}, \frac{y}{D}, \frac{z}{D}, \frac{U_j D}{\nu}, \frac{U_0 D}{\nu}, \frac{C_p \mu}{k}, \right.$$
$$\left. \frac{U_j^2}{\beta g D |T_j - T_0|}, \frac{\rho_j}{\rho_0}, \frac{U_j}{U_0}, \frac{P_j}{P_0} \right)$$

The length scale for the cross flow has been chosen as D because the cross flow produces wake behind the jet whose charactertic length is D near the nozzle, the region where the wake begins to appear.

Assume

$$Pr \equiv \frac{C_p \mu}{k} = const.,$$

$$Re_j \equiv \frac{U_j D}{\nu} \gg 1, \quad Re_0 \equiv \frac{U_0 D}{\nu} \gg 1.$$

The last two assumptions lead to the conclusion in a free turbulent flow that the viscosity is not important, that is the Reynolds stresses are much larger than the mean viscous stresses. Then we obtain

$$\frac{\overline{Q}}{\overline{Q}_{ref}} = \left(\frac{x}{D}, \frac{y}{D}, \frac{z}{D}, \frac{\rho_j}{\rho_0}, \frac{U_j}{U_0}, \frac{P_j}{P_0}, \frac{U_j^2}{\beta g D |T_j - T_0|} \right). \quad (1)$$

The quantity $\frac{U_j^2}{\beta g D |T_j - T_0|} \equiv Fr$ is called the Froude number which expresses the ratio of the inertia to the buoyancy force in the initial jet.

When $T_j = T_0$ ($\rho_0 = \rho_j$, since in this analysis the two fluids are assumed to be the same kind), equation (1) is simplified to

$$\frac{\overline{Q}}{\overline{Q}_{ref}} = \left(\frac{x}{D}, \frac{y}{D}, \frac{z}{D}, \frac{U_j}{U_0}, \frac{P_j}{P_0} \right). \quad (2)$$

Usually $\rho_o = \rho_d$ so that in this case the only important quantity is the ratio of two velocities.

III. EXPERIMENTAL EQUIPMENT

The main equipment consists of a wind tunnel, an air supply system, a nozzle and measuring probes. An overall sketch of the wind tunnel is shown in Fig. 2, and the details of the setup are shown in Fig. 3. When designing the setup, care was taken to insure the following: 1) uniform, low-turbulent free stream. 2) low-turbulent jet with very uniform and constant exit velocity distribution. 3) sensitive probes for velocity and temperature measurements. 4) accurate probe positioning device.

1. Wind Tunnels

For preliminary measurements a small wind tunnel with 4" x 4" test section was used. It is an open-circuit tunnel with a centrifugal fan driven by a 1 HP DC motor. Using this wind tunnel, the effects of test section walls and the tunnel wall boundary layers on the structure of the jet were investigated. This tunnel was also used for flow visualization experiments.

The main experiment was conducted in a larger wind tunnel which has a 28" x 28" test section and a length of 15'6" (Fig. 2). This tunnel is an open-circuit, suction type tunnel with an axial fan driven by a 53 HP DC motor. This wind tunnel had been used in the Jet Propulsion Lab. at Case Institute of Technology, and was reconstructed for the present experiment. It is a low-speed, low-turbulence wind tunnel, and thus very suitable for this experiment. Fine mesh screens are installed at the intake and serve to make larger eddies into smaller ones which decay faster. Due to

these screens and a high contraction ratio (10.4:1), the turbulence level at the test section is very low (0.4% at 20 $\sim$ 30 ft/sec, the velocity range in which present data are taken), and the velocity profile is very flat. The walls of the test section are made of Plexiglas plates. One side wall has a small door for easy access to the equipment inside the test section.

The jet was injected at a position three feet downstream from the beginning of the test section. The boundary layer thickness at this position was 1-1/2 in. In order to minimize the effect of the tunnel wall boundary layer, the flat plate, made of Plexiglas 17 in. wide and 24 in. long, was placed at a position 2-1/2 inches above the bottom wall, and the nozzle is set flush with this plate. The plate has a wedge-shape nose which is connected smoothly to the flat part. At the injection point, which is 2 inches from the nose, the boundary layer thickness is small compared with the diameter of the nozzle (less than 10%) so that its effect is expected to be negligible.

For the heated jet experiments it is desirable to have constant free stream temperature. Since this is an open-circuit wind tunnel, temperature cannot be controlled and is subject to the outside temperature change. However, the tunnel was placed in a well air-conditioned room, so that the temperature change during any one run of the experiment was within $\pm$ 0.2°F.

2. Nozzle

One of the important factors which control the structure of jet is the velocity profile at the exit of the nozzle. Generally

the velocity profile is not flat in practical cases; however in order to maintain well defined experimental conditions the initial velocity profile was made as flat as possible. For this purpose a specially designed nozzle was used in the present experiment. Its structure is shown in Fig. 4. Six turbulence-reducing screens of various mesh sizes are used, and the contraction part has a carefully designed contour. The contraction ratio is 16:1, and the exit diameter is 1/4". Fig. 5 shows velocity profiles at the exit for various jet speeds. Profiles are very flat over the whole diameter except for the thin boundary layer near the wall. Turbulence level at the exit is 0.3%.

For the heated jet experiment the nozzle was wrapped with asbestos for thermal insulation. The temperature profile at the exit was also found to be very flat.

To see the general behavior of the free jet from this nozzle, distributions of the mean velocity and the turbulence intensity along the jet centerline were measured, and are shown in Fig. 6. It can be seen that the length of the potential core (in which the flow is laminar, and the velocity remains constant) is four times the nozzle diameter. The location of the jet virtual origin (the origin of the self-similar region) is found to be very close to the nozzle exit (0.4 times the nozzle diameter upstream of the nozzle). Beyond $x/D = 8$, the centerline velocity decreases hyperbolically with the distance from this virtual origin, and the velocity profile is expected to be similar.

3. Air Supply System

Air for the jet was supplied by a 100 HP, two-stage compressor which can supply 402 CFM of air. Since air pressure of the compressor varies in the range between 80 and 100 PSI, it was necessary to design a suitable air control system in order to get constant velocity at the exit of the nozzle. The schematic of the system is shown in Fig. 7. Pressure fluctuation is reduced first by the pressure regulator to the order of $\pm$ 1/4 in. of water. This fluctuation is further reduced by the flowrate regulator so that the fluctuation of the flow rate is within $\pm$ 0.5% of the set value. The flowrate was measured by a Fisher and Porter rotameter.

For the hot jet experiment, air was heated by a heating tape wrapped around a steel pipe of 1-1/2 in. diameter. Using this heating tape it was possible to make jet temperature at the nozzle exit up to 400°F at the maximum flowrate.

4. Probes

Hot Wire and Anemometer

The hot wire probe is made from brass tubing of 1/4 in. diameter and 26 in. long with wire supporting tips made of bronze needles (Fig. 8). The diameter of the hot wire is 0.00015 in., and it is made from 90% platinum-10% rhodium Wallaston wire. The wire is etched in a thin column of nitric acid. The etched portion is about 0.045 in. long. The end of the hot wire probe is connected by a Cannon connector to the wire which leads to the

input of the hot wire anemometer set. A constant-current hot wire set, Shapiro and Edwards Model 50, was used in the experiment. The set consists of an amplifier, resistance bridge, potentiometer, mean square output meter and square wave generator, as shown in Fig. 9. The potentiometer allows one to measure the wire current up to one hundredth of a milliamp, which makes accurate velocity measurement possible. The time constant of the hot wire was about 450 microseconds, so that for the measurements of turbulence intensity and energy spectrum, the compensation circuit was applied to compensate forthe thermal inertia of the wire.

Pressure Probes

Total pressure was measured by a Kiel total head probe which is insensitive to pitch and yaw angles up to about 40 degrees. Where space is limited near the nozzle, a total head tube made from a hypodermic needle of 0.028 in. diameter was used (Fig. 8). Static pressure was measured by a Pitot static tube made from a hypodermic needle. It has two static pressure holes of 1/64 in. diameter at the positon 7 times tube diameter downstream from a rounded nose.

In a turbulent flow both total and static pressure measurements are subject to errors due to the lateral turbulent motion. Errors are not small in the present experiment, and this problem is discussed in the next chapter.

Temperature Probe

Temperature was measured by an Iron-Constantan thermo-couple

supported by a brass tube of 1/4 in. dia. and 26 in. long (Fig. 8). The diameter of the tip contact is 1/16 in.

Yaw Angle Meter

For the measurement of the mean flow direction, a small sensitive yaw angle meter was used. This is made of two hypodermic needles of 0.028 in. diameter with bevelled open ends. The flow angle can be determined by rotating the meter until pressures measured by the two tubes become equal. To measure three-dimensional flow direction, usually four tubes are used. But this increases the size of the probe and the rotating device becomes more complicated. In the present experiment the flow angles were measured in two planes to get three-dimensional flow direction.

In a turbulent flow the measurement is affected by the Reynolds stress, which is discussed in the next chapter.

Probe Positioning Apparatus

In the experiment most data were obtained by point by point measurements using various probes. Thus it was necessary to use an accurate probe positioning apparatus. The one used was a three-dimensional manipulator manufactured by Brinkmann Instrument. It can traverse 4, 3, and 3 in. in each direction, and can rotate the probe in the vertical plane. In order not to disturb the flow, the positioning device was put outside of the test section as shown in Fig. 2.

5. Other Equipment

Micromanometer

Pressure was measured by a Meriam micrometer Model 34 FB2 TM reading in thousandths of an inch of water pressure.

Microvolt-ammeter

The thermo-couple was connected to a microvolt-ammeter (Keithley Instruments, Type 150A). Since this is a sensitive instrument, it is very difficult to measure the mean temperature in a highly turbulent flow, because the instrument follows the fluctuations. To damp out large fluctuations R-C circuit was connected to the meter.

Wave Analyzer

Energy spectra of turbulence were measured by a General Radio wave analyzer Model 1900A. This has a frequency range of 0 to 55,000 cps and three bandwidths of 3, 10 and 50 cps. The input was taken from the amplifier of the hot wire set. Accuracy of the measurement is $\pm$ 3% of the indicated value up to 50 KC.

III. EXPERIMENTAL PROCEDURE

1. General

The present experiment consists of two parts. The first one is the investigation of an unheated jet in a cross flow, in which distributions of velocity, pressure and turbulence intensity are measured. The next one is for a heated jet, in which the temperature distribution is measured in detail.

In the unheated jet experiment, the most important variable is the velocity ratio U_j/U_o . In the heated jet case we have one more variable ρ_j/ρ_o . In many occasions these two variables are coupled and appear as a single parameter $\rho_j U_j^2/\rho_o U_o^2$ which is called the momentum ratio. Since most of the previous works treated the unheated jet cases, the term 'effective velocity ratio R' which is the square root of the momentum ratio is used in this report for the purpose of making it easy to compare the data in both experiments.

The value of R can be chosen arbitrarily, but to cover the practically important range, three cases $R \approx 4$, 6, 8 were investigated inboth heated and unheated jet experiments. These nominal values of R correspond to using the free stream speed upstream of the plate as the cross flow speed. Since the free stream speed above the plate is a few percent higher than that ahead of the plate, the actual values of R appropriate to the experiment are slightly lower than the nominal values. The nominal and actual values of R , along with the corresponding free stream

and jet speeds for the unheated jet experiment, are as follows.

R (nominal)	4	6	8
R (actual)	3.91	5.80	7.73
U_o (ft/sec)	30.7	25.8	20.7
U_j (ft/sec)	120	150	160

For simplicity, the nominal values will be quoted hereafter. The above combinations of speed were chosen so that differences in both jet and cross flow speeds for three cases were small.

For the heated jet experiment, only jet speeds were varied according to the jet temperature (density) keeping cross flow speeds constant. Experimental conditions of this case are summarized in Table I. Settings of both heating current and flow rate meter were determined by trial and error at first to get desired values of $\rho_j U_j^2$. For high temperature jets it took about two hours to achieve an equilibrium temperature. Care was taken to have constant jet velocity temperature and cross flow speed throughout any one run of the experiment. Detail procedures for two cases (unheated and heated) are explained below.

2. Unheated Jet Experiments

Jet Centerline

First, the location of jet centerlines was measured for R = 4, 6, 8. In addition, the experiment was done also for $R \simeq 10$. These profiles are important not only for practical reasons but also for defining the coordinate system. Experimentally

the centerline profile can be obtained by connecting points of maximum velocity in the plane of symmetry at each section of the jet. As shown in the next chapter the velocity is not necessarily maximum at the jet center of each section. This method of determining the jet centerline is inevitably trial and error, because the normal section of the jet cannot be specified until the centerline profile is known. In the present experiment normal planes to the centerline were determined by a step by step method in which, starting from the horizontal plane near the nozzle (jet was injected vertically upward), each normal plane was approximated by extrapolating the previously determined centerline.

The point of maximum velocity at each section was found both by the hot wire and by the total head tube (Kiel probe). Both results agreed very well. Since the velocity along the centerline decays much faster than the one in a free jet it is very difficult to determine the jet centerline beyond $s/D = 25$.

Velocity Distribution

For each momentum ratio, the mean velocity distributions were measured at several sections of the jet by the hot wire. Since the mean velocity changes its direction mainly in the xz-plane (the plane parallel to the cross flow), the hot wire was set normal to this plane. It is known that a hot wire measures the velocity component normal to it. The mean flow direction measurement (which is explained later in the chapter) shows that the change of the flow direction in the xy -plane is relatively

small except in the small region where the rotational velocity is large. Therefore the velocity measured in the manner described above is expected to be close to the magnitude of the actual velocity (the difference is about 3% for 15 degrees change in the xy-plane).

The velocity was measured point by point traversing the hot wire according to the coordinate defined above. In order to see the detail distribution, it was necessary to measure at 60 $\sim$ 100 points for each section depending on the actual size of the jet. This was a very cumbersome procedure, but since the actual size of the jet was small, it was impossible to insert a rake without disturbing the flow very much. An automatic traversing device in an inclined plane was not easy to design, and was given up for the present experiment.

In the present procedure it took about two hours to finish one section. Therefore the important problem was the 'drifting' of the hot wire calibration curve on which the velocity calculation was based. This drifting was made small by warming the wire for a rather long time (about 1.5 hours) just before the data were taken. Also, in order to minimize the error during the experiment the drifting of the wire was checked in a certain interval by measuring the free stream velocity, and the calibration curve was corrected accordingly. The overheat ratio of the wire was set at 0.3. Care was taken to have a very straight calibration curve in the operating range. Fig. 10 shows the examples of

the hot wire calibration curve.

The velocity measured by the hot wire is not exactly equal to the actual velocity in a highly turbulent flow. The relation between the measured and the true values is given by the equation (Ref. 18),

$$\bar{U}_{meas} \simeq \bar{U}\left(1 - \frac{1}{4}\frac{\overline{u^2}}{\bar{U}^2} + \frac{1}{2}\frac{\overline{v^2}}{\bar{U}^2}\right)$$

where u is the longitudinal velocity fluctuation and v is the lateral fluctuation. This correction was not done in the experiment, because the turbulence level is rather low in the jet, as shown in the next chapter.

Mean Flow Direction

Using a small yaw meter the mean flow directions were measured at points where the mean velocities were known. As has been explained in the previous chapter, this yaw meter was made of two hypodermic needles so that it can determine the flow direction only in one plane. Therefore in order to measure the three-dimensional flow direction as in the present case, it is necessary to measure in two planes which are perpendicular to each other. In the present experiment flow directions were measured in the xz-plane and the xy-plane. To determine the mean velocity vector at each point, calculations are necessary using the magnitude of the velocity measured by the hot wire and flow directions in two perpendicular planes. Referring to Fig. 11, their relations are given by

$$\bar{U}^2 = \bar{U}_m^2 \left(\sin^2\alpha' + \frac{\cos^2\alpha'}{\cos^2\beta'} \right)$$

$$\tan\gamma' = \tan\alpha' \tan\beta' \cos\beta' \qquad (3)$$

where notations should be clear from the figure. When β' is small, $\bar{U} \doteqdot \bar{U}_m$ as explained in the previous section.

The purposes of the flow direction measurement are to calculate the mass and the momentum fluxes across each section of the jet, and also to obtain the distribution of the rotational velocity (the velocity component parallel to the normal plane). Thus it is necessary to know velocity components normal and parallel to the jet cross section. They are given by (Fig. 12)

$$\left.\begin{aligned} \bar{U}_n &= \bar{U}_m \cos(\alpha' - \theta) \\ \bar{U}_p^2 &= \bar{U}_m^2 \left[\sin^2\alpha' + \frac{\cos^2\alpha'}{\cos^2\beta'} - \cos^2(\alpha' - \theta) \right] \\ \tan\delta &= \frac{\cos\alpha' \tan\beta'}{\sin(\alpha' - \theta)} \qquad -\pi \le \delta \le \pi \end{aligned}\right\} \qquad (4)$$

where θ is the angle of inclination of the jet centerline (or the value of α' at the center), and δ is the angle between $\bar{U}_p$ and the parallel component of the cross flow velocity. Although the flow in the jet has been assumed to be parallel to the jet centerline at each section, in the region away from the center the flow becomes parallel to the free stream. Consequently,

in order to see the rotational velocity field in the vortex region (which is of major interest here) one has to project the velocity on the plane normal to the path of the vortex core. This can be done simply by replacing θ in Eq. (4) by the angle determined from the path of the vortex core.

It can be shown (Ref. 19) that the behavior of the yaw meter is expressed by the equation

$$\frac{\overline{P_1} - \overline{P_2}}{\frac{1}{2}\rho \overline{U}^2} = C\left(1 + \frac{\overline{u^2}}{\overline{U}^2} + \frac{1}{2}\frac{\overline{v^2}}{\overline{U}^2}\right)\sin\Theta + C\frac{\overline{uv}}{\overline{U}^2} \qquad (5)$$

where P_1 and P_2 are pressures measured by two tubes of the meter, Θ is the angle between the mean flow direction and the yaw meter, and $\overline{uv}$ is the Reynolds stress. The above equation shows that even if $\Theta = 0$, $\overline{P_1}$ and $\overline{P_2}$ are not necessarily equal in a turbulent flow with shear. Since the turbulent jet is a typical shear flow, this yaw meter gives an error depending on the value of the Reynolds stress at the measuring point. In a free jet the maximum value of $-\overline{uv}/\overline{U}^2$ is about 0.02, so that the maximum error in Θ is about one degree. In the present experiments the local mean velocity is much larger than the one in the free jet because of the convective velocity U_o. Thus the error in Θ is expected to be much smaller than the above estimate.

Since this procedure of mean flow direction measurement is more painstaking than the velocity measurement, in order to save

labor it was decided to measure the flow direction only in the half of the normal plane, assuming that the flow is symmetric with respect to the center-plane. The equipment was carefully set up so that the flow was almost symmetric, as shown in the next chapter.

Since to calculate the mean velocity vector it is necessary to measure three quantities (speed and two angles) at one point, care was taken to place the probe at exactly the same point for each measurement.

Pressure Distribution

At present there is no reliable way to measure static pressure in a highly turbulent flow. An ordinary Pitot static probe suffers appreciable error due to lateral velocity fluctuations. The correction of the measured value to obtain the true value of the static pressure is complicated in the sense that it depends on the lateral turbulence intensity and also on the ratio of the average eddy size of turbulence to the diameter of the Pitot tube. In the present experiment another problem is the alignment of the probe, since the mean flow direction changes very much at different points. Therefore the static pressure was not measured, but was calculated from the values of the total pressure and the speed. A Kiel total head probe was used for the total pressure measurement. This probe is particularly convenient when the exact flow direction is unknown. Similar to the Pitot static probe, the measured values should be corrected in a

turbulent flow. The correction formula is given by

$$\overline{P}_{t,meas} = \overline{P}_s + \left(1 + \frac{\overline{u^2}}{\overline{U}^2} + \frac{\overline{v^2}}{\overline{U}^2} + \frac{\overline{w^2}}{\overline{U}^2}\right) \tfrac{1}{2} \rho \overline{U}^2 \qquad (6)$$

where both v and w are laterial velocity fluctuations. Since $\overline{v^2}$ and $\overline{w^2}$ were not measured, the measured values of $\overline{P}_t$ were not corrected. But the error is expected to be small because the turbulence level is rather low in the flow due to the convective velocity .

Turbulence Intensity Distribution

The distribution of the turbulence intensity in the normal plane was measured by the hot wire. Since the wire was set normal to the xz -plane as in the velocity measurement, the turbulence intensity measured in this way gives the fluctuation level in the direction of $\overline{U}_m$. However it is expected to be very close to the intensity in the direction of the mean velocity vector .

The constant-current hot wire system which was used in the present experiment is not appropriate for measurement in a highly turbulent flow, because of the non-linearity of the hot wire response. It is supposed to be accurate in a flow with the turbulence intensity less than 10%. As shown in the next chapter the maximum intensity observed was 22% in the present case, but in the most of the region the intensity was less than or slightly larger than 10%. Error is 10 $\sim$ 15% if the turbulence intensity is about 20%.

The wire overheat ratio was 0.3 as in the velocity measurement, and the wire response was compensated for thermal inertia in order not to lose the energy of the high frequency fluctuation.

Energy Spectrum

The turbulence energy spectra were measured at a few points in one section of the jet, and they were compared with the spectrum at the corresponding position in a free jet.

The output of the hot wire was first amplified and compensated, then sent to the wave analyzer. The mean square output voltage of the wave analyzer at frequency f_c is given by

$$\overline{e^2_{out}} = \phi(f_c)\,\Delta f$$

where Δf is the filter bandwidth and $\phi(f_c)$ is the energy/cps at $f = f_c$. The actual spectrum $E(f)$ of the velocity fluctuation is calculated from the relation

$$E(f) = \frac{\phi(f)}{(GS)^2}$$

where G is the transfer function of the hot wire set, and S is the sensitivity of the hot wire.

Since

$$\int_0^\infty E(f)\,df = \overline{u^2}$$

then

$$\frac{E(f_c)}{\overline{u^2}} = \frac{\phi(f_c)}{\int_0^\infty \phi(f)\,df} = \frac{\overline{e_{OUT}^2}(f_c)}{\int_0^\infty \overline{e_{OUT}^2}(f)\,df} \qquad (7)$$

This is a convenient form of presenting the energy spectrum. The filter bandwidth Δf of 3 cps was used in the experiment.

3. Heated Jet Experiments

Jet Velocity Centerline

As in the unheated jet measurements, the jet velocity centerline location was measured by the hot wire and the total head probe. When the jet temperature is very high, the effect of density changes cannot be neglected. Since the hot wire responds to the 'mass velocity' ρU , the mean electric current through the wire (for a constant current set) corresponds to the value of $\overline{\rho U}$. Separating velocity and density into mean and fluctuating parts, we have

$$\overline{\rho U} = \bar{\rho}\,\bar{U} + \overline{\rho' u} \ .$$

Therefore the point of maximum $\overline{\rho U}$ does not necessarily correspond to the point of the maximum velocity. Neglecting the correlation between density and velocity fluctuation which is very small usually, it is still necessary to know the mean density (or temperature) distribution in order to find the point of maximum $\bar{U}$. It was found that this correction was very small because the density change was smaller than the velocity near the center. In this respect the measurement

by the total head probe is better, because it can detect the variation of ρU^2 (the static pressure is almost uniform in the jet). However, since the sensitivity of the manometer was limited, the total head probe was used mainly in the upstream region.

Temperature Centerline

The point of the maximum temperature in one section does not coincide with the maximum velocity point, so that one must define separately the centerline for the temperature distribution in a manner similar to the jet velocity centerline. Temperature was measured by the IC thermo-couple. The temperature centerline location was obtained by connecting points of maximum temperature in the plane of symmetry at each jet cross section which is already specified by the jet velocity centerline.

Temperature Distribution

The temperature distributions were measured at several sections of the jet for R = 4 and 8. The data were taken at 60 $\sim$ 100 points in one section, and they were connected smoothly to get uniform contours of constant temperature. The thermo-couple was connected to the micro-volt meter to measure the small temperature difference. The fluctuation of the reading was made small by the use of the additional RC circuit. Temperature distribution at each section was measured up to the point where the temperature is equal to the mean of the maximum and the free stream temperature. Beyond this point the measurement becomes difficult due to the large fluctuation. The temperature at the

nozzle exit was checked and kept constant throughout any one run of the experiment.

V. RESULTS OF MEASUREMENTS

1. Unheated Jet Experiments

Fig. 13 shows the jet velocity centerline location for the effective velocity ratios R = 4, 6, 8 and 10. These profiles can be correlated by a single curve

$$\frac{z}{D}\left(\frac{U_o}{U_j}\right)^{0.94} = 0.623\left(\frac{x}{D}\right)^{0.445} + 0.290 \qquad (8)$$

as shown in Fig. 14. The constant in the right hand side represents the effect of the potential core. The power for U_o/U_j was found by trial and error. The power for x/D and other numerical constants were determined by drawing smooth fitting curves. The error of the measurement increases as we go downstream, because the velocity distribution becomes very flat near the center. The estimated error in the centerline location near the most downstream section measured was $\pm$ 3%.

Using the coordinate system determined from the jet velocity centerline obtained above, the distributions of the velocity at several jet sections for R = 4, 6, 8 were measured, and results are shown in Figs. 15 through 18. Strictly speaking, these are the distributions of $\bar{U}_m$ instead of $\bar{U}$. Although $\bar{U}$ can be calculated from $\bar{U}_m$ according to Eq. (3), the difference is small, and it is not important in order to observe the jet structure. The results are presented in the form of contours of the non-dimensionalized velocity difference $\tilde{u}$ which is defined as

$$\tilde{u} = \frac{\bar{U} - U_o}{\bar{U}_{max} - U_o} \quad .$$

Although the use of $\tilde{u}$ is just a matter of convenience, at far downstream sections where the jet velocity is almost parallel to U_o it is possible to classify the flow configuration as

$$0 < \tilde{u} \leq 1 \qquad \text{jet region}$$
$$\tilde{u} < 0 \qquad \text{wake region} \quad .$$

At upstream sections the directions of two velocities $\bar{U}$ and U_o are different so that it is not simple to distinguish between jet and wake.

Since the velocity $\bar{U}$ is composed of the axial velocity $\bar{U}_n$ (normal to the jet cross section) and the velocity $\bar{U}_p$ (parallel to the jet section), it is important to separate these two components. After the mean flow directions were measured in two planes at each point, $\bar{U}_p$ and σ were calculated according to Eq. (4). The distributions of $\bar{U}_p$ are shown in Figs. 19, 20, 21. The data were taken in one half of the plane, because the flow is almost symmetric with respect to the centerplane. Fig. 22 shows the rotational velocity field in the developing region (of the rotational motion) for $R = 8$. Figs. 23, 24, 25 show the rotational velocity field at downstream sections for $R = 4, 6, 8$. In these figures the velocities $\bar{U}_p$ and $\bar{U}_r$ are non-dimensionalized

by U_o , which appears to be the appropriate scale, because the rotational motion is induced by the cross flow.

One of the important features in the study of a turbulent jet is the analysis of the mass flux increase which is directly related to the entrainment of the surrounding non-turbulent fluid by the turbulent flow. In order to calculate the mass flux through the normal plane at each section, it is necessary to know the distribution of the normal velocity $\bar{U}_n$. $\bar{U}_n$ can be calculated from $\bar{U}_m$ according to Eq. (4). Then similar to $\tilde{u}$, the dimensionless quantity $\tilde{u}_n$ for the normal velocity is defined as

$$\tilde{u}_n = \frac{\bar{U}_n - U_{on}}{\bar{U}_{n,max} - U_{on}}$$

where $U_{on} = U_o \cos\theta$ is the normal component of the cross flow velocity. In Figs. 26, 27 and 28 the contours of constant $\tilde{u}_n$ are shown. In these figures only the jet region is considered for the purpose of the mass flux calculation. The use of the quantity $\tilde{u}_n$ is more convenient than the previously defined $\tilde{u}$, because $\tilde{u}_n$ does not include the rotational velocity whereas $\tilde{u}$ is related to both axial and rotational velocities. The calculation of $\bar{U}_n$ requires the measurement of the flow direction only in one plane, as can be seen from Eq. (4), which simplifies measurements and calculations compared with those of $\bar{U}_p$. This made it possible to measure the distributions of $\bar{U}_n$ at a larger number of sections than were possible for $\bar{U}_p$, and measurements of $\bar{U}_n$ at several sections are necessary to study

the mass flux change with distance. In order to study the mass flux increase in a turbulent region from the mean velocity distribution, it is necessary to define the 'edge' of the turbulent region. Following Keffer and Baines (Ref. 6), the jet boundary is defined as the surface where the normal velocity excess ($\bar{U}_n - U_{on}$) is 10% of the maximum value at a given section; that is, the turbulent region is where $0.1 \leq \tilde{u}_n \leq 1$. Then the mass flux can be calculated by integrating $\bar{U}_n$ over this region. The momentum flux can be calculated in a similar way. Fig. 29 shows the result of the mass flux calculation. For the entrainment analysis in Chapt. 6, the momentum fluxes in the x and z directions are calculated by decomposing $\bar{U}_n$ into both directions. Fig. 30 shows the z -momentum flux distribution.

The velocity distribution along the jet centerline is shown in Fig. 31. The ordinate was chosen as the inverse of the non-dimensionalized (by U_j) velocity $\bar{U}_c$ in order to see clearly the hyperbolical decrease of $\bar{U}_c$ near the nozzle. For comparison, free jet data are shown in the same figure. The data were taken in the free from the same 1/4 in. nozzle with the initial velocity U_j = 120 ft/sec. In each case the virtual origin (of the flow near the nozzle in cases of the jet in the cross flow) can be found by extrapolation of the straight part as done in the figure.

The distributions of the total pressure were measured at a few sections just to compare with Jordinson's data (Ref. 16). One of the present results is shown in Fig. 32. Notice that the data were taken not on the plane normal to the jet centerline,

but on the plane normal to the cross flow (yz -plane), similar to Jordinson. The static pressure distribution at the same position is shown in Fig. 33. The values of the static pressure were calculated form the values of the total pressure and the velocity measured by the hot wire. At several points the static pressure was measured by the Pitot static probe with its axis aligned in the mean flow direction at each point. Both results for the static pressure agreed within the experimental error.

Figs. 34 and 35 show the distributions of the turbulence intensity relative to the maximum velocity $\bar{U}_{max}$ at the section for R = 4 and 8. The hot wire gives the quantity $\sqrt{\overline{u^2}}/\bar{U}$ (intensity relative to the local velocity), however the distribution of $\overline{u^2}$ itself is more interesting because it shows the distribution of the kinetic energy of turbulence.

To see the more detail structure of turbulence, the energy spectra were measured both at the center of the jet and at the point of maximum velocity (center of the vortex motion) at the section x/D = 23 for R = 8. The results are shown in Fig. 36. The energy spectrum of turbulence in the free jet at the corresponding position is also shown in the same figure for comparison. The figure shows the slightly different structure of turbulence in two jets.

2. Heated Jet Experiments

To see the similarity of the jet structure with respect to the momentum ratio, the jet velocity centerline locations were

measured in the heated jets for R = 4 and 8. The result is presented in Fig. 37. The figure shows that the velocity centerline location of the heated jet coincides with that of the unheated jet as long as the momentum ratio is kept constant. The initial jet temperature above the free stream temperature was 75°F and 320°F. The velocity ratio and the density ratio for each case are listed in Table 1.

Figs. 38 and 39 show the profiles of the temperature centerline (locus of the maximum temperature in the plane of symmetry) of heated jets in comparison with jet velocity centerline profiles for R = 4 and 8. From these figures it is clear that the temperature centerline location cannot be correlated by the momentum ratio alone.

Similarly to measurements of velocity distributions, temperature distributions were measured at several sections both in the mildly heated jet and in the high temperature jet. The results are presented in Figs. 40 through 47. They show the contours of the dimensionless coefficient $\bar{\theta}$ which is defined as

$$\bar{\theta} = \frac{\bar{T} - T_o}{\bar{T}_{max} - T_o} \quad .$$

The location of the maximum temperature at a given section is not necessarily in the plane of symmetry as is also true for the velocity distribution. Unlike velocity, temperature is a scalar quantity so that only one dimensionless temperature has to be

defined. The above choice of θ is convenient, as is seen to vary from 0 to 1 at any one section.

One important use of the measurements of temperature distributions is that it is possible to investigate the jet structure at the far downstream position where it is no longer possible to measure the velocity distribution. In the present experiment the data were taken at several positions up to $x/D = 70$ for the high temperature jet ($T_j - T_o = 320°F$). For this jet the effect of buoyancy cannot be neglected. It is possible to see the effect on the jet structure by comparing temperature distributions of the highly heated jet with those of the mildly heated jet. This is discussed in the next chapter. For the large value of x, which is measured along the jet velocity centerline, x was determined by extrapolating the centerline which was neasured up to about $x/D = 25$. The normal plane for large x was taken to be the vertical plane normal to the cross flow (yz-plane), since the angle of inclination of the centerline was very small in that region.

Fig. 48 shows the distribution of the maximum and the centerline temperature along x in jets with the initial temperature $T_j - T_o = 320°F$ for $R = 4$ and 8. For $R = 4$, the maximum and the centerline temperature are identical.

The figure also shows the temperature distribution in the free jet with $T_j - T_o = 330°F$. It is known that in a free jet the temperature excess ($\overline{T}_{max} - T_o$) decreases inversely with the distance from the virtual origin just as velocity. For the jet

in the cross flow the same behavior as the free jet is expected for small ξ where the jet still retains the characters of the free jet. In Fig. 49 the inverse of the dimensionless temperature excess is plotted as the ordinate so that the hyperbolic change can be seen clearly. Also in this way it is easy to find the virtual origin. The higher temperature curves in Fig. 49 are simply replots of the data of Fig. 48.

Fig. 50 is a plot similar to Fig. 49, but for the downstream region. Here one finds that $(\bar{T}_{max} - T_0)^{-1.3} \propto (\xi - \xi_0)$. This means that the distribution of the temperature along ξ can be expressed by the relation

$$\left(\frac{\bar{T}_{max} - T_0}{T_j - T_0}\right) \propto \left(\frac{\xi}{D} - \frac{\xi_0}{D}\right)^{-0.77} \qquad (9)$$

where ξ_0 represents the location of the virtual origin of the temperature distribution for large ξ, which is different from the one found for the distribution for small ξ.

From distributions of temperature at several sections of the jet, one can see the lateral spread of temperature with distance. To show this quantitatively, the half-value radius $r_{1/2}$ was introduced. $r_{1/2}$ is defined as the effective radius of the area ($S_{1/2}$) occupied by the contour of $\bar{\theta} = 0.5$ where the temperature excess ($\bar{T} - T_0$) is 50% of its maximum value ($\bar{T}_{max} - T_0$) at a given section, namely

$$r_{1/2} = \sqrt{\frac{S_{1/2}}{\pi}} \quad .$$

$r_{1/2}$ is analogous to the half-value radius defined for the circular jet. When the temperature distribution is similar at each section as in a free jet, the use of $r_{1/2}$ as a characteristic length scale in the lateral direction is very convenient. In the present case the temperature distribution is almost similar so that the above defined $r_{1/2}$ is expected to represent the lateral spread of temperature in the jet. Fig. 51 shows the distributions of $r_{1/2}$ with the distance x in jets with $T_j - T_0$ = 320°F for R = 4 and 8. Free jet data are also shown. In fig. 52 the distribution of $r_{1/2}$ in jets with different initial temperature are shown. The heat spreads linearly near the nozzle as in the free jet. However, in the far downstream region it seems that it spreads with a certain power of x. This power was found in the same way as the temperature distribution along x. Fig. 53 shows that in the far downstream region the temperature spreads as

$$\frac{r_{1/2}}{D} \propto \left(\frac{x}{D} - \frac{x_0}{D}\right)^{0.36} \tag{10}$$

where the value of x_0 is not exactly equal to but close to the value given in Eq. (9).

VI. DISCUSSION OF RESULTS

1. Jet Centerline

According to the dimensional analysis in Chapter II, there are two non-dimensional numbers, namely U_j / U_0 and ρ_j / ρ_0, which are important in the problem of a jet in a cross flow, when the buoyancy force is negligible. From a physical consideration it is known that the deflection of the jet is predominantly determined by one dimensionless quantity, $\rho_j U_j^2 / \rho_0 U_0^2$ (the momentum ratio).

In order to check the importance of the momentum ratio experimentally, it is necessary to conduct an experiment using a heated (cooled) jet or using two different types of fluid. However, if two densities differ very much, the buoyancy force becomes important and complicates the analysis.

Eq. (8) in Chapter V which was obtained by correlating the data taken inthe present unheated jet experiment shows the importance of the velocity ratio. From the heated jet experiment, however, it is clear that the momentum ratio is indeed the significant factor to determine the jet deflection (Fig. 37). Although the effect of buoyancy is not negligible for the high temperature jet, the centerline location can be correlated by the momentum ratio alone, at least in the range of temperature used in the experiment. One then expects that the deflection angle of the jet is determined mainly by the ratio of the jet momentum flux in the Z -direction to the momentum flux in the

x -direction.

When the buoyancy force is not negligible, the jet centerline tends to shift upward (if $\rho_j < \rho_0$). But this tendency is compensated by the increase of the momentum flux in the x -direction resulting from the increased rate of entrainment due to the decrease of the jet density (this is discussed more in a later section). Therefore, it is difficult to distinguish the effect of buoyancy from the study of the jet centerline location.

Eq. (8) can be written in the form (even when $\rho_j \neq \rho_0$)

$$\frac{z}{D} = R^{0.94}\left[0.623\left(\frac{x}{D}\right)^{0.445} + 0.290\right]$$

or

$$\frac{z}{D} - \frac{z_0}{D} = 0.623\, R^{0.94}\left(\frac{x}{D}\right)^{0.445} \qquad (8)'$$

where $z_0/D = 0.29\, R^{0.94}$ represents the point from where the deflection of the jet starts, and is often called the effective source of the jet (not to be confused with the virtual origin of the jet). For $R \geq 6$, this point nearly coincides with the end of the potential core. Since for $R \leq 4$, the potential core itself deflects, the two points do not coincide. Thus, if R is increased, z_0 should approach to a value equal to the length of the free jet potential core, so that the above relation between z_0 and R is true only in a certain range of R . The

general case is discussed in the next section. For practical purposes consideration of the effective source is not convenient. For this reason most empirical formulas of the jet centerline set the origin at $\bar{Z} = 0$. If the jet deflection is assumed to start at $\bar{Z} = 0$, the present data give the following equation:

$$\frac{\bar{Z}}{D} = 0.89\, R^{0.94} \left(\frac{X}{D}\right)^{0.36} . \qquad (11)$$

Comparison of Eq. (8) (or Eq. (11)) with other published data is presented in Fig. 54. These data were taken by Jordinson (Ref. 16), Keffer and Baines (Ref. 6), Margason (Ref. 2), Storms (Ref. 20) and Ivanov (Ref. 1). The empirical equation of the centerline obtained from those data is given in the form

$$\frac{\bar{Z}}{D} = A R^{a} \left(\frac{X}{D}\right)^{b}$$

where A , a , b are numerical constants. The value of " a " given by the above investigators ranges from 0.67 to 1.0, and the value of " b " from 0.33 to 0.39. This wide scatter of data is attributable to the differences in experimental conditions. The major factors seem to be the initial conditions of jet and the wind tunnel size. The jet initial conditions (velocity profile, pressure, turbulence level) are not given in most of the papers. The sizes of the wind tunnels used by the above investigators are summarized Ref. 2. According to the investiga-

tions by Carlson et al. (Ref. 3), the wind tunnel size in the present experiment as well as in others is large enough so that its effect on the jet path is negligible. From the analysis of the free jet it is known that the jet structure becomes independent of the initial condition after some distance downstream from the nozzle. However, the centerline location of the jet in a cross flow at a given section is affected by the upstream condition. So far there is no systematic study about the effects of the jet initial conditions on the jet path. Since these conditions in the present experiment are close to the standard ones (flat velocity profile, low turbulence level), the centerline location is about the middle of other data as can be seen in Fig. 54.

Due to the complexity of the problem, there is no purely theoretical calculation of the centerline location available. Several semi-empirical formulas have ben derived. Vizel and Mostinski (Ref. 4) calculated the deflection of the centerline from the ratio of the jet momentum flux in the Z -direction (assumed constant) to an estimate of the pressure force acting in the X -direction. McAllister (Ref. 7) used a similar method, but instead of the estimated pressure force he used an estimate of the momentum flux in the X -direction which is brought into the jet by the entrained fluid. In addition to special assumptions contained inthe estimates, both analyses finally require that a pair of numerical constants be determined from the experiments, which of course makes it easier to fit the derived formulas to

the data.

As for the temperature centerline, its location is different from that of the jet velocity centerline. As can be seen in Figs. 38 and 39, unlike the jet velocity centerline location the momentum ratio alone cannot correlate the temperature centerline location. For a given momentum ratio, increasing jet temperature causes less penetration of the temperature centerline. In order to find the important factors which control the temperature field, it was tried to correlate the temperature centerline location of heated jets with various combinations of velocity and density. The results are presented in Fig. 55. The temperature centerline location is found to be represented by a single curve

$$\frac{Z}{D} = 0.73 \left(\frac{\rho_j}{\rho_0}\right)^{0.63} \left(\frac{U_j}{U_0}\right)^{1.04} \left(\frac{X}{D}\right)^{0.29} . \qquad (12)$$

This combination of density and velocity ratios does not mean much physically. It is necessary to find the dimensionless quantities which are more important in the problem. Since the temperature field is strongly related to the velocity field, the momentum ratio is expected to be one important factor to determine the temperature centerline location. As mentioned above the momentum ratio alone cannot correlate the data. To find another quantity, one has to understand why the temperature centerline shifts with increasing jet temperature while the jet centerline is fixed (for a given momentum ratio). As is explained in

detail in the next section, when the jet temperature is increased, the strength and the size of the vortex motion are increased. Thus, more heat is transferred into the vortex region, and more concentration of heat around the vortex center results. The temperature centerline does not mean much physically but it merely represents the over-all penetration of heat into the cross flow. Therefore its location is strongly affected by the location of the vortex center, especially when much heat is concentrated in the vortex region. Thus, as the jet temperature is increased for a given momentum ratio, the vortex center moves away from the jet center (due to the increased size of the vortex motion), and consequently the temperature centerline shifts downward. Such increased activity of the vortex motion seems to be attributed to the increased rate of entrainment. Ricou and Spalding (Ref. 21) found that in a free jet the rate of entrainment is related to the density ratio ρ_j / ρ_o . Thus it is expected that increasing jet temperature (decreasing jet density) causes more entrainment, which activates the vortex motion. Besides the jet density, the velocity U_j and the kinematic viscosity ν_j are changed when the jet temperature is changed while keeping the same momentum ratio. As has been discussed in the dimensional analysis (Chapter II), the flow structure is assumed to be independent of the viscosity since the Reynolds number is very large. As for U_j , it is increased when T_j is increased. But its change is rather small (inversely proportional to the square

root of the density change), and its effect on the vortex motion seems to be less important compared with the density effect. The buoyancy force also increases the vortex motion. However, this seems to be a secondary effect in the present experiments, because the temperature difference is already small at the position where the buoyancy force becomes important to the vortex motion. Consequently Eq. (12) is better written in the form

$$\frac{Z}{D} = 0.73 \left(\frac{\rho_j U_j^2}{\rho_0 U_0^2}\right)^{0.52} \left(\frac{\rho_j}{\rho_0}\right)^{0.11} \left(\frac{X}{D}\right)^{0.29} \qquad (12)'$$

Unlike the jet velocity centerline, the temperature centerline starts deflecting from a point very close to the nozzle, so that it was unnecessary to find an effective source of the Z coordinate corresponding to Z_0 for the jet centerline.

2. Detail Structure of Jet Velocity Field

Right at the exit of the nozzle the jet is considered to be potential flow, because of the low turbulence intensity and very thin boundary layer. Due to the very steep velocity gradient at the edge of the jet, the flow is very unstable, which causes the development of the free shear layer (called mixing layer). The mixing layer thickness increases with distance, and the potential flow region (called potential core) disappears after some distance from the nozzle. In the potential core the velocity remains essentially constant. Except for the small momentum ratio

($R \leq 4$), the potential core is deflected very little by the cross flow. For a free jet this core length depends on the jet Reynolds number, boundary layer thickness at the exit, and turbulence level. For a jet in a cross flow it has been found from the experiments that the core length decreases with decreasing momentum ratio. The reason for this is that the mixing layer spreads faster when there is cross flow, because of the tangential stress induced by the cross flow. The relation between the core length and the velocity ratio (for simplicity, the case $\rho_j = \rho_0$ is considered) can be obtained as follows. First, consider the free jet. The relation between the spreading angle of the mixing layer ε_0 and the core length ℓ_0 is given by (see Fig. 56)

$$\tan \varepsilon_0 = \frac{D/2}{\ell_0} = \frac{D}{2\ell_0} . \tag{13}$$

A jet in a cross flow is subjected to the additional shear stress which acts tangentially to the jet cross-section. The increase of the spreading velocity of the mixing layer (entrainment velocity) due to this tangential stress is assumed to be proportional to the characteristic tangential velocity scale, which is chosen to be the cross flow velocity. Then the increase of the spreading angle is proportional to U_0 / U_j, since the boundary between the mixing layer and the potential core is moving with a velocity nearly equal to U_j. Denoting the additional

spreading angle by ε' which is assumed to be much smaller than ε_0, we obtain

$$\tan\varepsilon = \tan(\varepsilon_0 + \varepsilon') \doteq \tan\varepsilon + \tan\varepsilon' = \frac{D}{2\ell_0} + C\frac{U_0}{U_j}$$

where C is a constant. Therefore the core length is given by

$$\frac{\ell}{D} = \frac{1}{2\tan\varepsilon} = \frac{1}{\frac{D}{\ell} + 2C\frac{U_0}{U_j}} \qquad (14)$$

This relation is compared with the data taken by Pratte and Baines (Ref. 22) in Fig. 57. In their experiment $\ell_0/D = 6.4$ and $C = 0.36$. As can be seen in the figure Eq. (14) agrees very well with the data. Kronauer (Ref. 23) obtained exactly the same relation by correlating his experimental data. He gave $\ell_0/D = 6.0$ and $C = 0.67$.

After this initial region, the jet becomes fully turbulent, and the jet deflection commences. In this region of the flow the important features are the distortion of the jet cross-section and the formation of the vortex wake behind the jet. The distortion is mainly due to the pressure distribution around the jet and the entrainment. The jet spreads to the side of lower pressure. Since this spread-out region has smaller axial momentum than the region near the center, it is deflected more by the pressure drag and the entrained momentum in the cross flow direction. Consequently the jet cross-section has the shape of a crescent. This deforma-

tion is also influenced by the vortex motion in the wake when it becomes strong. It is well known that behind a cylinder placed normally to a uniform stream a pair of counter-rotating 'standing eddies' are formed in the Reynolds number range $6 < Re_d < 40$. If the Reynolds number is increased more, eddies shed from the cylinder alternately, forming the familiar Karman vortex street in the wake region. Very similar to this situation, a pair of eddies are formed behind the jet soon after the jet leaves the nozzle. These eddies do not shed, however, because of their strong interaction with the jet; instead they acquire axial momentum from the jet, and move along the jet path. These eddies are somewhat similar to a 'vortex-pair'. After the formation the development of the vortex motion is controlled by such factors as the normal component of the cross flow-velocity, the shape of the jet cross-section (which acts to block the cross flow) and the jet initial velocity (not including the case $\rho_j \neq \rho_o$). For a given velocity ratio (for a given jet path and a given jet cross-sectional shape), increasing the cross flow velocity causes faster development of the vortex motion, but this is compensated by the increased jet velocity (to keep R constant) which gives less time for the development. Therefore, the development of the vortex motion is expected to be controlled by the velocity ratio. As the velocity ratio is increased, the jet experiences a larger normal component velocity of the cross flow at a given distance from the nozzle, because the jet is

deflected less. Consequently the strength of the vortex is larger for larger R (Figs. 23, 24, 25). Initially the vortex strength increases with distance. However, viscosity acts to retard this motion so that the vortex strength reaches its maximum at a certain distance from the nozzle, and starts decaying thereafter.

Fig. 15 shows that for R = 4 the jet cross-section is not much altered by the vortex motion, and that this vortex wake strongly interacts with the ordinary wake (which is formed by the cross flow separation from the jet in the region near the nozzle) since the height of the jet centerline is low. For larger R, the jet is swept around into the wake region due to the strong vortex motion (Figs. 16, 17, 18).

After the initial region the jet still retains the general characteristics of a free jet for some distance, as evidenced by the hyperbolical decay of the velocity along the jet centerline (Fig. 31). But, the vortex strength grows rapidly, and its influence on the jet structure increases. This region may be called the transition region. The jet centerline has very large curvature in this region.

In the far downstream region, the jet centerline becomes nearly parallel to the cross flow, and the velocity excess in the jet (the velocity defect in the wake) is very small. The small velocity excess makes it difficult to study the jet structure from velocity measurements. However, it is possible to investigate

this region by measuring temperature distributions in the heated jet, or by using flow visualization techniques.

Near the end of the transition region, the vortex motion nearly ceases developing, but it decays much slower than the axial velocity excess so that the vortex motion dominates the flow field in the far downstream region.

Although the vortex motion is weak for $R = 4$, it is strong enough to retain the crescent-shaped jet cross-section for quite a long distance, and then as the vortex motion decays, this shape is destroyed gradually by diffusion. For larger momentum ratios, more axial momentum is convected by the rotational velocity toward the vortex region from the region around the jet center. Consequently the point of maximum velocity shifts from the jet center to the vortex center after some distance from the nozzle. By the time the development of the vortex motion is almost finished, most of the axial momentum is in the vortex region. As the vortex activity decays, this concentrated momentum in the vortex region diffuses in the turbulent region due to turbulent transport, and the distribution becomes more uniform.

Temperature Field

In the initial region the temperature at the center remains constant. The core length of the temperature is shorter than that of the velocity because the thermal boundary layer is a little thicker than the velocity boundary layer at the nozzle exit. At the end of initial region, the temperature distribution has very

flat contours.

In the transition region, at first the centerline temperature decays inversely with the distance measured from the virtual origin, and then decays more slowly (Fig. 49). Due to the diffusion of temperature into the wake region, the centerline temperature decays faster than the temperature in a free jet. In spite of the deformation of the jet cross-section, the temperature spreads linearly at first as in the free jet, and then more slowly. This situation is similar to the jet in a co-axial uniform stream. When the jet temperature is increased (the jet density is decreased), the centerline temperature decays faster because of the increased entrainment of the outside cold fluid (Fig. 49). The effect of the jet temperature on the jet spreading is not so simple. Increasing the jet temperature means increasing the jet velocity to keep the momentum flux $\rho_j U_j^2$ constant ($\rho_o U_o^2$ is kept constant in these experiments at any one momentum ratio). Therefore although the lateral spreading rate is increased, so is the axial velocity. This is the reason why the effect of the jet temperature change on the jet spreading is not so apparent in Fig. 52 as on the temperature decay, shown in Fig. 49.

Contours of constant temperature have more rounded shape than those of constant velocity, since temperature diffuses more readily into the wake region than the momentum. This difference between the turbulent transport of heat and momentum can be seen

clearly for R = 4. As the momentum ratio increases, more heat concentrates around the vortex center. The relation between the degree of such concentration and the vortex activity is quite apparent for R = 8 when temperature distributions at several sections are compared. Up to about x/D = 25, the heat concentration in the vortex region continues to increase (Figs. 40, 41). According to the rotational velocity measurement (Figs. 22, 25), at x/D = 23 the vortex activity has already passed its peak (the rotational velocity is larger at x/D = 12.5 than at x/D = 23). After the peak up to around x/D = 25, the rotational velocity is still large enough to be able to resist the diffusive action of turbulence and keeps convecting heat into the vortex region. Then as the vortex motion decays, the heat is diffused, and the temperature distribution becomes more uniform in the turbulent region (Fig. 42).

For a given momentum ratio, as the jet temperature increases more heat is convected into the vortex region (compare Figs. 41 and 44), which indicates the increased vortex activity. This is because of the increased entrainment, as has been explained in the section on the jet centerline.

In the far downstream region constant temperature contours become circular for R = 4, but later they become slightly oval-shaped, which shows the existence of the vortex motion at very far downstream positions (Figs. 46, 47). For R = 8 as explained above the balance between the turbulent transport and the convection by the vortex motion changes the temperature distri-

bution.

It is interesting to note that in the far downstream region the maximum temperature excess ($\bar{T}_{max} - T_0$) changes with distance as (Eq. (9))

$$\frac{\bar{T}_{max} - T_0}{T_j - T_0} \propto \left(\frac{z}{D} - \frac{z_0}{D}\right)^{-0.77}.$$

Also, the temperature profile spreads as (Eq. (10))

$$\frac{r_{1/2}}{D} \propto \left(\frac{z}{D} - \frac{z_0}{D}\right)^{0.36}.$$

The configuration of the flow in the far downstream region is qualitatively similar to the free jet in a coaxial uniform stream. For a jet in a parallel stream it can be shown from the similarity analysis (Ref. 18) that the asymptotic variations of ($\bar{T}_{max} - T_0$) and $r_{1/2}$ are given by

$$\frac{\bar{T}_{max} - T_0}{T_j - T_0} \propto \left(\frac{z}{D} - \frac{z_0}{D}\right)^{-2/3}$$

$$\frac{r_{1/2}}{D} \propto \left(\frac{z}{D} - \frac{z_0}{D}\right)^{1/3}. \qquad (15)$$

Compared with this, the temperature in the jet in a cross flow decreases slightly faster, and also the jet spreads a little faster. This slight increase of the spreading rate appears to be due to the vortex motion which increases the entrainment rate.

Despite the gradual change of temperature distribution around the center of the turbulent region as explained above, the main jet structure remains almost similar as evidenced by the close similarity to the jet in a parallel stream.

In the far downstream region, the lateral spread of temperature in the plane of symmetry is predominantly determined by the axial convection and the lateral diffusion. As the rotational motion decays, the lateral convection by the rotational velocity becomes negligible compared with the axial convection. In the direction normal to the plane of symmetry (η -direction) the temperature is relatively uniform, so that diffusion in that direction is assumed to be negligible. Therefore, in analogy to the jet in a parallel stream, the temperature distribution in the plane of symmetry is expected to remain similar in the far downstream region.

Mathematically, the balance between the axial convection and the lateral diffusion is expressed as

$$U_0 \frac{\partial}{\partial \xi}(\bar{T}-T_0) = \frac{\partial}{\partial \zeta}\left[D_T \frac{\partial}{\partial \zeta}(\bar{T}-T_0)\right] \qquad (16)$$

where D_T is the eddy diffusivity in the ζ -direction, and ζ is measured from the temperature center. Using the results obtained above, one can assume

$$\frac{\bar{T}-T_0}{\bar{T}_c-T_0} = f(\tau) \quad \text{or} \quad \bar{T}-T_0 = f(\tau)\,\xi^{-m}$$

$$D_T = g(\tau)\,\xi^{-n}, \qquad \tau = \zeta\,\xi^{-m}$$

where m and n are constants. Substitution of these relations into Eq. (16) gives

$$U_0(-m\xi^{-m-1}f - m\xi^{-m-1}\tau f') = \xi^{n-3m}(g'f' + gf'') \tag{17}$$

Putting $n = 2m - 1$, Eq. (17) becomes

$$U_0(-mf - m\tau f') = g'f' + gf'' \tag{18}$$

If one can assume $g = \text{const.} \equiv C$ as in cases of a free jet and a jet in a parallel flow, Eq. (18) becomes

$$Cf'' + mU_0\tau f' + mU_0 f = 0 \tag{19}$$

Using boundary conditions,

$$f = 1 \quad \text{at} \quad \tau = 0$$

$$f \to 0 \quad \text{as} \quad \tau \to \pm\infty,$$

the solution of Eq. (19) is

$$f \equiv \frac{\bar{T} - T_0}{\bar{T}_c - T_0} = \exp\left(-\frac{mU_0}{2C}\tau^2\right). \tag{20}$$

The values of m and C are expected to be a function of the momentum ratio and the density ratio. However, Eq. (20) shows that by using a suitable lateral length scale, it is possible to obtain a universal temperature profile, and that the profile is very much like the Gaussian error curve.

The experimental data presented in Fig. 58 show that this is indeed the case. The data were taken in the far downstream region ($x/D > 15$) for R = 4 and 8 with ($T_j - T_o$) ranging from 50°F to 320°F. $\ell^+_{1/2}$ and $\ell^-_{1/2}$ are the values of ζ (measured from the temperature center) at which $\bar{T}$ is equal to 1/2($\bar{T}_c + T_o$). The figure shows that in the positive ζ region temperature falls slightly faster than the Gaussian curve near the outer edge. In the negative ζ region the lateral temperature distribution is almost Gaussian. This slower decrease in the negative ζ region is due to the limited space between the jet and the bottom plate. In any case, the temperature distribution seems to be represented by a single curve. Practically this result is important because the temperature distribution in the plane of symmetry gives the common basis for comparing the over-all mixing of a hot (cool) jet and a cross flow.

Turbulence

Measurements of velocity and temperature distributions give very useful information about the structure of the jet. However, it is important to understand that both distributions are very

much influenced by the turbulence structure of the jet. It is known that in a free turbulent flow the transport of quantities such as momentum, temperature and turbulence energy are related to the double structure of the turbulence (large eddies and small energy-containing eddies). The large eddies whose scales are comparable to the width of the flow, distort the bounding surface between the turbulent and the non-turbulent flow, and thus control the entrainment process. These large eddies contain smaller scale eddies. Most of the turbulence energy is distributed among these small eddies (energy-containing eddies). The turbulent transport by the large eddy motion is considered to be convective, whereas the transport by small eddies is the gradient-type diffusion. The turbulent transport of a certain quantity can be influenced predominantly by either one of those features of turbulence, or by both. In the present experiments the vortex motion in the jet appears to be large eddy motion. It can be seen by comparing distributions of velocity and temperature (especially for $R = 4$) that the transport of temperature is more strongly influenced by the vortex motion (or large scale eddies) than the transport of velocity. The transport by large eddies tends to make the distribution of any quantity uniform in the turbulent region, as evidenced by the large uniform temperature region inthe middle for $R = 4$ (Fig. 47). For large momentum ratios the velocity distribution is affected by the vortex motion, but this must be considered differently from the

large eddy activity. When the strength of the vortex is very large, it is no longer large eddy motion; rather it is a part of the mean flow field.

Figs 34 and 35 show that the distribution of turbulence energy is very much like that of temperature, which means that the transport of turbulence energy is also strongly influenced by the convective motion of the vortex wake. It is known that the turbulence energy is nearly constant inside the turbulent region except near the bounding surface. Therefore the measured time-mean value of the turbulence intensity at any point depends mainly on this constant value and also on the intermittency factory γ ; namely we have

$$\overline{q^2} = \gamma \, \overline{q_0^2}$$

where $\overline{q^2}$ is the measured turbulence kinetic energy per unit volume, and $\overline{q_0^2}$ is its value in the turbulent region. The turbulence is assumed to be almost isotropic in the present experiments so that $\overline{q^2} \simeq \frac{3}{2} \overline{u^2}$. Since $\overline{q_0^2}$ is known to be almost constant in the turbulent region, the distribution of $\overline{u^2}$ (Figs. 34, 35) nearly represents the distribution of the intermittency factor. Generally γ is unity well inside the turbulent region. In the present case γ is expected to be almost unity at the point when $\overline{u^2}$ is maximum, and this point is considered to be the center of the turbulent region (which includes both jet and wake) as opposed to the previously defined jet center which has not as much physical meaning.

It is important to measure the turbulence energy distribution among eddies of different size for studying the structure of the isotropic turbulence, because the theory can predict some form of the energy spectrum in a certain range of the wave number which can be tested by the experiment. The energy spectrum is not measured very often in a turbulent shear flow, but it helps in understanding the detail structure of turbulence. Fig. 36 shows a compariosn of energy spectra measured in a free jet and in a jet in a cross flow for R = 8. The spectrum of a free jet decreases according to - 5/3 power of frequency (or wave number) in a certain range of frequency. This region is called the inertial sub-range which is usually observed in isotropic turbulence with high turbulence Reynolds number, and this form of the spectrum can be explained by dimensional analysis for isotropic turbulence. Also, in a shear flow this - 5/3 power is observed in a rather wide range of frequency. This is mainly because eddies are usually isotropic in the higher range of frequency regardless of the anisotropicity of the energy-containing eddies (so called local-isotropy). The energy spectra of a jet in a cross flow measured at the center of the jet at the center of the vortex motion have slightly smaller power (- 1.75 power) than - 5/3 in the inertial sub-range. The spectral form of the energy containing eddies at the vortex center (which is very close to the center of the turbulent region as explained above) is very similar to the one at the center of the free jet, but the former decreases

faster in a higher wave number range, which indicates less dissipation of the turbulence energy. Compared to the spectrum at the vortex center, the one at the jet center has less energy in the energy-containing range, and more energy in the inertial sub-range.

3. Entrainment Analysis

An important feature of a free turbulent flow is the existence of a sharp boundary between turbulent and non-turbulent regions. Across such a boundary the random vorticity jumps from zero value in the non-turbulent region to non-zero value in the turbulent region (actually this vorticity change takes place in a very thin layer, the so-called viscous super-layer). Due to this sharp vorticity gradient, the vorticity diffuses into the non-turbulent region through the action of the viscosity. Once the vorticity is diffused, the strength of the vorticity associated with the velocity fluctuation is increased due to the stretching caused by the local mean rate of strain, and thus the originally non-turbulent region becomes fully turbulent. In this way the turbulent front moves forward into the non-turbulent region, and consequently the flow rate in the turbulent region increases with distance. This process is called entrainment. Since this entrainment process is very important in studying the structure of a free turbulent flow, it has been given much attention in recent years. It is known that the detail process of entrainment is influenced not only by the local flow conditions but also by the whole flow

structure. Thus its study involves all kinds of problems encountered in the general study of turbulence structure. For this reason, the detailed entrainment process is not well understood. The recent stage of its study can be seen in Ref. 24. According to Townsend (Ref. 25) and others, it is possible to calculate the entrainment rates for the flows with structural similarity such as jets, wakes and turbulent boundary layers without referring to the detailed process. Thus, the object of the present analysis is to study the entrainment rate for the jet in a cross flow assuming its similarity of the flow structure.

In an axisymmetric flow the rate of increase of the mass flux in the turbulent region is given by

$$\frac{dm_T}{d\xi} = 2\pi \rho_0 r_T^* \frac{dr_T^*}{d\xi} \bar{U}_b \tag{21}$$

where m_T is the mass flux in the turbulent region (assumed to be non-dimensionalized) at a given section, r_T^* is the radius of the turbulent region, and $\bar{U}_b$ is the axial velocity at which the boundary is moving. Or using a simpler form

$$\frac{dm_T}{d\xi} = 2\pi \rho_0 r_T^* \bar{U}_e \tag{22}$$

where $\bar{U}_e$ is the velocity at which the turbulent front is advancing into the non-turbulent region, and it is called the entrainment velocity which represents the entrainment rate. The relation (22)

can be applied to the present problem as long as r_T^* is considered to be the effective radius such that $r_T^* = (S_T/\pi)^{1/2}$ where S_T is the area occupied by the turbulent region. In the present experiment neither m_T nor r_T^* was measured, so that the velocity cannot be calculated directly from Eq. (22). The exact value of $\overline{U}_e$ is not of interest, but its variation with distance is of interest in this analysis. Therefore, if it is possible to measure m and r^* which are proportional to m_T and r_T^*, respectively, at each section, the behavior of $\overline{U}_e$ can be studied. To do this, the jet boundary has been defined in Chapter 5 so as to measure m and r^* from the mean velocity distribution.

In a circular jet the integration of the axial velocity over a cross section gives m_T^* itself, and in a region of similarity the lateral length scale such as the half-value radius for the velocity distribution represents the behavior of r_T^*. For a circular jet in a coaxial uniform stream, the situation is not simple. The integration of the velocity over a given section is not convergent. The integration of the velocity excess converges, but its value does not mean much physically. In ths sense the situation is the same for wakes and turbulent boundary layers. Therefore it is necessary to define the boundary to get quantities related to m_T and r_T^*, as has been done in the present work. For the jet in a parallel stream the flow configuration near the nozzle is very similar to a free jet as long as the

jet initial velocity is very much larger than the free stream velocity. Thus, the measured m and r^* (by defining the jet boundary) are expected to be proportional to m_T and r_T^* as in the free jet case. In the far downstream region where the velocity excess is very small compared with the free stream velocity, the velocity excess distribution is expected to have similarity structure. Since in this region the velocity is almost equal to U_0 (free stream velocity) everywhere, m and r^* are related by

$$\frac{m}{m_T} \doteq \frac{\pi r^{*2} U_0}{\pi r_T^{*2} U_0} = \left(\frac{r^*}{r_T^*}\right)^2 \qquad (23)$$

where the ratio r^* / r_T^* is expected to be constant because of similarity. In between the two regions there is no simple relation between m and m_T, r^* and r_T^*.

In the present experiements, velocity data were taken in the regions corresponding to the intermediate and downstream regions of the jet in a parallel stream. Although the flow configuration of the present experiment is much more complicated than the jet in a parallel stream the velocity distributions show nearly similar patterns at each section. Thus, in analogy to the jet in a parallel stream the measured mass flux (shown in Fig. 29) is assumed to represent m_T, and so is r_T^*. The entrainment velocity $\bar{U}_e$ calculated from measured m and r^* according to Eq. (22) is presented in Fig. 59.

In flows with similarity structure the entrainment velocity is known to be a constant fraction of the mean velocity variation at a given section, namely

$$\bar{U}_e = E\,(\bar{U}_{max} - U_o) \tag{24}$$

where the constant of proportionality E is called the entrainment constant. In these cases one can think of two fluids (turbulent and non-turbulent) flowing in the same direction. However, in the present case the two fluids are not parallel. Thus, it seems necessary to take into account the flow direction in the relation like Eq. (24). In fact, the value of E calculated from measured $\bar{U}_e$ and $\bar{U}_{max}$ according to Eq. (24) is too large compared with the value for the free jet, and in spite of the nearly similar flow structure, E changes very much with distance (it varies from 0.15 to 0.39 between x/D = 7 and 23 for R = 8, whereas in the free jet E = 0.045). the important thing is that in the present problem the rate of strain field (which controls the entrainment process as explained above) is different from the case of two parallel streams. The rate of strain field should be decomposed into the parallel (to the jet path) component and the normal component. Notice that the length of the potential core of the jet in a cross flow can be obtained by the same consideration as explained in the previous chapter. Also, the normal component of the cross flow velocity is different from the

parallel part in the sense that it strongly influences the vortex motion. This vortex motion controls the bounding surface in a similar way to large eddies, and thereby plays a role in the entrainment process. Thus similar to Eq. (24) the entrainment velocity in the present problem is expected to be related to the velocity variations in two directions through the relation

$$\bar{U}_e = E_1 (\bar{U}_{max} - U_0 \cos\theta) + E_2 U_0 \sin\theta . \quad (25)$$

The second term of the right hand side of the above equation represents the effect of the normal component of the free stream. Since it is known that the entrainment process is influenced by the whole flow structure, the two right hand side terms of Eq. (25) are not likely to be completely independent. This suggests that for a given velocity ratio (in this analysis only the case $\rho_j = \rho_0$ is considered for simplicity) the values of E_1 and E_2 are nearly constant, assuming similarity of the flow-structure, but these values are different for the different velocity ratios.

Fig. 59 shows that Eq. (25) gives the variation of $\bar{U}_e$ with very good accuracy using the constant values of E_1 and E_2. The angle θ has been determined from the jet centerline profile. The values of E_1 and E_2 used in the figure are

R	E_1	E_2
4	0.070	0.320
6	0.061	0.242
8	0.067	0.182

These precise values may not be important, since $\bar{U}_e$ was not measured directly, nor calculated from Eq. (22) using m_T and r_T^*. The important fact is that constants E_1 and E_2 exist. As can be seen in the velocity distributions for R = 4, the wake region occupies the larger part of the turbulent region so that measured m which is the mass flux in the jet (the region where $\bar{U}_n > U_{on}$) is considered to be a small fraction of m_T. However, for R = 8 the jet region occupies nearly the whole turbulent region. Thus, the values of E_1 and E_2 given above for R = 8 are probably close to the actual values.

Eq. (22) can be considered as an over-all continuity equation across a jet cross-section. In addition to this we have momentum equations in two directions, namely in the axial direction (ξ -direction) and in the normal direction (ζ -direction). Denoting the representative flow direction at a given cross-section by θ (which is assumed to be equal to the angle of inclination of the jet centerline), and assuming that momentum changes only because of entrainment, the rate of change of momentum inthe axial direction is given by:

$$\frac{dM}{d\bar{z}} = U_0 \cos\theta \frac{dm}{d\bar{z}} \tag{26}$$

where M is the momentum flux across the jet section. Similarly the rate of change of momentum in the normal direction is given by:

$$M \frac{d\theta}{d\bar{z}} = -U_0 \sin\theta \frac{dm}{d\bar{z}} . \tag{27}$$

By solving the above equations, the following relations among m, M, and θ can be obtained:

$$U_0 (m - m_r) = \frac{M_r}{\tan\theta} \tag{28}$$

$$\frac{M}{M_r} = \frac{1}{\sin\theta} \tag{29}$$

$$\left(\frac{M}{M_r}\right)^2 = 1 + \frac{U_0^2}{M_r^2} (m - m_r)^2 \tag{30}$$

where m_r and M_r are the values of the mass and the momentum flux at the effective source of the jet. Eq. (30) which shows the relation between M and m, is compared with the data in Fig. 60. As the momentum ratio increases, the curve approaches that of the free jet, which appears in the figure as a straight line $M/M_r = 1$.

In Eq. (28) the term ($m - m_r$) represents the increase of the mass flux due to the entrainment, so that assuming the entrained fluid has the average velocity U_0 , the term U_0 ($m - m_r$) represents the increase of the momentum flux in the x -direction, namely

$$M_x = U_0 (m - m_r) . \tag{31}$$

In Fig. 61 this relation is checked using the experimental values of M_x and m . The figure shows that for small $\bar{x}$, M_x is substantially larger than the entrained momentum. The difference is due to the pressure force. In the far downstream region the effect of the pressure force seems to be negligible.

In formulating Eqns. (26) and (27) the effect of the pressure field has been completely neglected. As a result of this assumption the momentum flux in the z -direction is expected to remain constant without any force acting in that direction. As explained above, the momentum flux increase in the x -direction is due to both the entrained momentum and the pressure force for small $\bar{x}$. Therefore, it is expected that the z -momentum flux decreases especially in the region near the nozzle. The data show the gradual decrease of the z -momentum flux with distance from the nozzle (Fig. 30). In that figure the absolute value of M_z is not important, especially for R = 4 and 6, because M_z is calculated only in the jet region neglecting the z -momentum

in the wake region. Such decrease of M_z is partly due to the definition of the jet region, but mainly due to the effect of the pressure. In the Appendix the pressure effect is estimated by considering the pressure distribution on the jet surface.

Assuming that the z -momentum approaches a constant value after some distance from the nozzle where the pressure force is no longer important, the equation for the jet path is given from Eq. (28) as

$$\tan\theta = \frac{dz}{dx} = \frac{M_r}{U_o(m-m_r)} . \tag{32}$$

Using the relation

$$ds = \sqrt{1+\left(\frac{dz}{dx}\right)^2}\, dx$$

Eq. (32) becomes

$$M_r \frac{d^2z}{dx^2} + U_o \frac{dm}{ds}\left(\frac{dz}{dx}\right)^2\left[1+\left(\frac{dz}{dx}\right)^2\right]^{1/2} = 0 . \tag{33}$$

The boundary conditions for the above differential equation are

$$\left.\begin{array}{l} z = 0 \\ \dfrac{dx}{dz} = 0 \end{array}\right\} \quad \text{at} \quad x = 0$$

where the effective source is assumed to be at the origin within the accuracy of this analysis (so that also $M_r \fallingdotseq M_{jo}$). In

In order to solve Eq. (33) it is necessary to know $dm/d\xi$ which cannot be given at present by theory alone as may be clear from the expression of $dm/d\xi$ given in Eq. (22). Therefore, the analytical derivation of the centerline equation is always semi-empirical. Using experimental data for $dm/d\xi$, Eq. (33) can be solved for small ξ and large ξ. Since there are several analyses available concerning the jet centerline location near the nozzle, Eq. (33) is not solved for small ξ here. Instead, it is tried to solve Eq. (33) in the far downstream region using the information obtained from the temperature measurements.

When ξ is very large, we have $\xi \fallingdotseq x$, and Eq. (33) becomes

$$M_{j0} \frac{d^2z}{dx^2} + U_0 \frac{dm}{dx} \left(\frac{dz}{dx}\right)^2 = 0 \quad . \tag{34}$$

According to Eq. (10) the area of the turbulent region for large ξ varies as $x^{0.72}$. Since the velocity is almost equal to U_0 everywhere in this region, the mass flux increases as $U_0 x^{0.72}$, that is

$$m = K D^2 U_0 \left(\frac{x}{D}\right)^{0.72}$$

$$\therefore \quad \frac{dm}{dx} = K' D U_0 \left(\frac{x}{D}\right)^{-0.28} \tag{35}$$

where K' is a constant, but its value is different for the different momentum ratios. Substituting Eq. (35) into Eq. (34), and using the boundary conditions, the solution is given by

$$\frac{z}{D} = \frac{2.0}{K'} R^2 \left(\frac{x}{D}\right)^{0.28} \tag{36}$$

where $R = U_j/U_0$. The power of 0.28 is exactly equal to the value obtained by Pratte and Baines (Ref. 22) from the study of a flow-visualization experiment. In the present experiment, too, the profile of the temperature cneterline for large $\frac{x}{D}$ has the power very close to 0.28 (Figs. 62).

VII. FLOW VISUALIZATION EXPERIMENT

1. Introduction

In fluid mechanics as well as in other fields, visual observation is the most convincing way of understanding what is really happening, especially when the situation is rather complicated. However, we are very often plagued by problems involved in making good flow visualization. The main problems are the selection of a proper tracer, the method of its injection into the flow, and obtaining good photographs.

In the present experiment kerosene smoke was used as tracing gas, because it is easy to produce it continuously, and the smoke is clear to see. Although the smoke is not so toxic, it is necessary to have proper ventilation of the room. Another trouble was that kerosene smoke condensed everywhere in the pipe line, and this caused fluctuation of smoke pressure. This situation was improved by putting drains at proper positions. The smoke was injected into the same nozzle that was used in the main experiment.

Although both side views and cross-sectional views of jet are interesting, cross-sectional views are particularly important to help elucidate the jet structure, and therefore cross-sectional views were taken at a number of downstream sections. Illuminating the cross-section of the jet by light from a thin slit, pictures of cross-sectional views were taken. The equipment used for this experiment, procedures and results are explained below.

2. Equipment

Smoke generator

The structure of the smoke generator is shown in Fig. 63. The smoke obtained from this generator is premixed with air so that the pressure and the flow rate of the smoke can be varied, which is convenient for the present experiment. Kerosene is heated above its boiling point in an evaporator which is made from a glass tube with a coiled heater. The kerosene vapor is then mixed with cool air, and becomes oversaturated. Thus small drops of kerosene are formed which can be seen as smoke. The flow rate of air can be adjusted and is measured by a flowmeter. Generally the increase of the flow rate after the air is mixed with kerosene vapor is negligible. The liquid kerosene level is kept constant in an evaporator so that the amount of smoke generated is controlled by the temperature of the heater.

Wind Tunnel

For convenience of taking pictures a small wind tunnel with 4 x 4 in. test section was used. The test section is 22 in. long, and is made of Plexiglas plates. The turbulence level of the free stream was 0.3%. The jet was injected at a position 2 in. downstream from the beginning of the test section. At this position the boundary layer thickness was about half of the nozzle diameter. Although this affects the detail structure of jet, it does not change the overall structure significantly. Likewise the effect of test section walls is not negligible, but it is not so important

for this experiment as long as the momentum ratio is small.

Camera and Apparatus for Illumination

Pictures were taken with a Polaroid camera with close-up lens. Its fastest shutter speed was 1/300 of a second which was a little too slow for taking pictures of nearly instantaneous structure of the jet from the side, but fast enough to see the cross-sectional structure.

For illumination of the jet cross-section, an apparatus was made by putting a 1000 W projection lamp in the box with a slit in front. The slit gap was adjustable so that the gap can be made wide enough to give sufficient illumination yet narrow enough to be able to see the cross-sectional view.

3. Experimental Procedure

Because of the limited space in the wind tunnel test section, the experiment was conducted only for the case $R = 4$ ($\rho_j \doteqdot \rho_o$). When side views were taken, the free stream velocity U_o was kept at 5 ft/sec. The jet was illuminated from the top, and the camera was put about 3 feet from the side wall. The method of illumination and camera position for taking cross-sectional pictures are shown in Fig. 64. The velocity U_o was 10 ft/sec in this case. The slit gap and the shutter speed were determined by trial and error, which was made easy by the use of the Polaroid camera. The amount of smoke injected was about 5% of the total jet flow rate. This is thick enough to see the smoke clearly, yet thin enough not to cause change of the jet structure.

4. Results

Fig. 65 shows the general structure seen from the side. A close look at the region near the nozzle is shown in Fig. 66. Cross-sectional pictures were taken at x/D = 2, 5, 20, 70. They are shown in Figs. 67 through 70. Two pictures at each position are shown in order to see the difference in the jet structure at different instant.

For the purpose of observing the vortex motion in the jet more clearly, a picture was taken of a laminar jet which is shown in Fig. 71. Since the jet velocity was too small, no data were taken for this case.

5. Discussion of Results

In the previous chapters we have seen that the jet structure determined from velocity, temperature or pressure distributions are different from each other. Therefore pictures taken here should be interpreted as showing the jet structure drawn from the concentration distribution of kerosene particles. Compared with the temperature distribution at the corresponding position, it can be seen that the concentration distribution is very similar to the temperature distribution.

Fig. 65 shows the convoluted boundary between turbulence and non-turbulent region. In spite of the narrow space in the test section, the jet still has upward motion at the end of the test section.

Fig. 66 gives a close look at the potential core and the

initial region of the jet. Before the end of the potential core, the jet is already deflected. The length of the potential core was found to be 1.7 D from the velocity measurement.

At $\bar{z}/D$ = 2 the jet cross-section is flattened and has a crescent shape (Fig. 67). A small amount of smoke goes into the separated wake. At $\bar{z}/D$ = 5 the size of the jet is increased very much, and two distinct wakes are visible (Fig. 68). According to the heated jet experiment, contours of constant temperature at $\bar{z}/D$ = 20 (Fig. 46) are nearly circular; the smoke picture (Fig. 69) shows a distinct hollow at the bottom. The reason for this is that the instantaneous structure of the jet is not always symmetric with respect to the center-plane, as can be seen by comparing two pictures at each section. The symmetry plane inclines in a random manner, so that low temperature (low concentration) in the hollow region is averaged out and does not show up in the mean distribution. The cause of this random inclination may be the unbalance in the strength of two vortices. At $\bar{z}/D$ = 70 (Fig. 70) two vortex regions are clear, and the shape is almost similar to the one at $\bar{z}/D$ = 20.

Unlike other pictures the vortex motion shown in Fig. 71 is laminar. The jet is bifurcated as it goes downstream. Such bifurcation did not occur in the main experiment because of the strong interaction between two vortex wakes.

In this flow visualization experiment, a question arises con-

cerning the behavior of kerosene particles which have larger size and weight than air. How much can they follow the streamlines of air? Considering horizontal motion with gravity acting downward, the kerosene particles have steady downward motion, the velocity of which can be estimated from the balance between the gravity force and the upward drag. Using the Stokes law of drag acting on a sphere in a slow uniform stream, one obtains the relation

$$\frac{4}{3}\pi R_0^3(\rho-\rho_a)g = 6\pi\mu R_0 V$$

where R_0 is the average radius of kerosene particles, ρ_a and ρ are densities of air and kerosene, respectively, and V is the steady downward velocity (the terminal velocity). Then V is give by

$$V = \frac{2}{9}\frac{R_0^2(\rho-\rho_a)g}{\mu} \fallingdotseq \frac{2}{9}\frac{R_0^2\rho g}{\mu}$$

Substituting R_0 = 10 microns and suitable values for ρ , μ (of air) and g , the downward velocity V turns out to be 3.3×10^{-2} ft/sec, which is negligible compared with either U_0 or the average rotational velocity in the jet. Along the curved streamline the effect of the centrifugal force is important. When a kerosene particle moves along a curved streamline it suffers larger centrifugal force than air with the same velocity, so that it does not follow the streamline exactly. Assume that the kerosene particle deviates

from the streamline with the average velocity V' normal to the streamwise velocity U . Again using the Stokes drag law, we have

$$\frac{4/3\,\pi R_0^3 \rho U^2}{r'} = P - 6\pi\mu R_0 V' \qquad (37)$$

where P is the total pressure force acting on the particle, and r' is the radius of curvature of the kerosene particle path. Consider a lump of air which occupies the same volume as a kerosene particle, and has the same velocity U . Then we have

$$\frac{4/3\,\pi R_0^3 \rho_a U^2}{r} = P' \qquad (38)$$

where r is the radius of curvature of the streamline. Since V' is expected to be small, assume $r = r'$ and $P = P'$. Then Eqs. (37) and (38) give

$$\frac{V'}{U} = \frac{2}{9}\frac{R_0^2}{\mu}(\rho - \rho_a)\frac{U}{r} \doteq \frac{2}{9}\frac{R_0^2\rho}{\mu}\frac{U}{r}. \qquad (39)$$

In the present problem, r is minimum at the nozzle exit (neglecting the effective source). For simplicity assuming a parabolic profile of the jet centerline expressed by

$$\frac{x}{D} = KR^{-2}\left(\frac{z}{D}\right)^2 \quad (K \doteq 4.0)$$

the minimum value of r is given by

$$r_{min} = \frac{DR^2}{2K} \quad .$$

Therefore from Eq. (39) V'_{max} is given as

$$\frac{V'_{max}}{U} = \frac{4K}{9} \frac{R_o^2 \rho U_j}{\mu D R^2} \tag{40}$$

Substituting R_o = 10 microns, R = 4, U_j = 5 ft/sec, D = 1/4 in., and appropriate values for ρ (of kerosene), μ (of air) into Eq. (40), V'_{max} turns out to be

$$\frac{V'_{max}}{U} = 1.2 \times 10^{-5} \quad .$$

Although this is a rough estimate, it can be concluded that the deviation of kerosene particles from curved streamlines of air are negligible. Notice that the above analysis is applicable to a laminar case. What this result means for a turbulent case is that particles are convected by the mean flow field of air. The fluctuating velocity causes the diffusion of particles.

VIII. SUMMARY AND CONCLUSIONS

Several aspects of jets in a cross flow were studied mainly experimentally. The problems discussed herein are: the penetration of jets into the cross flow (jet centerline location), the penetration of heat (temperature centerline location), the detail measurement of velocity and temperature distributions at several jet cross-sections, the measurement of rotational velocity distributions, study of the turbulence structure of jets, the analysis of the entrainment rate and finally the flow visualization experiment.

The measurement of the jet centerline location in both heated and unheated jets shows the importance of the momentum ratio in the experiments. The detail measurement of velocity distributions reveals the marked change of the jet structure with the momentum ratio. Such factors as the deformation of the jet cross-section and the development of a vortex wake behind the jet (both are interrelated) contribute to produce complex patterns of the velocity distribution. The vortex motion grows stronger with increasing momentum ratio. In heated jets, this vortex motion is also influenced by the density ratio of two fluids. As the rotational velocity increases, more momentum, heat and turbulence energy are transported into the vortex region. The vortex activity attains its peak in the region where the jet centerline has large curvature, and decays rather slowly thereafter. The distributions of temperature and turbulence energy are more

strongly influenced by this rotational velocity field than are the distributions of velocity.

The structure of turbulence in the present experiments is different from that in other flows in the sense that the activity of large scale eddies are augmented by the vortex motion, and thus their energy is no longer negligible compared to that of energy-containing eddies. To see how much this different turbulent structure and also the rather complicated flow configuration influence the entrainment process, the entrainment rate was calculated from the data obtained here. It was found that the normal component of the cross flow velocity affects the entrainment rate in a manner nearly independent of the axial component of cross flow.

Several conclusions are drawn from the present study of the jet in a cross flow.

1. The jet centerline location is determined solely by the momentum ratio. The penetration of heat is controlled by both the momentum ratio and the density ratio. The buoyancy effect does not appear to be important within the density differences and in the flow region studied.
2. The velocity distributions show that the jet structure is more complicated than was hitherto known. The best previous description of the structure was in the work of Jordinson (Ref. 16), in which the structure was

determined by total pressure distributions. The jet structure is strongly influenced by the momentum ratio as well as the density ratio for the heated jet, and this is expected to be true also for the cooled jet.

3. Both temperature distributions and smoke pictures show that the vortex motion dominates the flow field in the far downstream region.
4. The jet deflection is determined mainly by the ratio of the momentum flux in the direction of jet injection to that in the cross flow direction. The momentum flux in the direction of jet injection decreases slightly because of the pressure force on the jet but this decrease does not appear to be very important to the jet deflection.
5. The increase of the entrainment rate as compared with a free jet is largely due to the normal component of the cross flow velocity.

LIST OF REFERENCES

1. Abramovich, G.N.: The Theory of Turbulent Jets, M.I.T. Press, 1963.

2. Margason, R.J.: "The Path of a Jet Directed at Large Angles to a Subsonic Free Stream," NASA TN D-4919, 1968.

3. Carlson, C.W., Hsu, J.J., and Meyers, C.A.: "The Penetration and Mixing of Air Jets Directed Perpendicular to a Stream," ASME Report, 1968.

4. Vizel, Ya.M. and Mostinskii, I.L.: "Deflection of a Jet Injected into a Stream," J. of Eng. Phys., Vol. 8, No. 2, 1965.

5. Shandorov, G.S.: "Calculation of a Jet Axis in a Drifting Flow," NASA TT F-10, 638, 1966.

6. Keffer, J.F. and Baines, W.D.: "The Round Turbulent Jet in a Cross-Wind," J. of Fluid Mech., Vol. 15, 1963.

7. McAllister, J.D.: "A Momentum Theory for the Effects of Cross Flow on Incompressible Turbulent Jets," Ph.D. Dissertation University of Tennessee, 1968, also quoted in Ref. 17.

8. Vogler, R.D.: "Interference Effects of Single and Multiple Round or Slotted Jets on a VTOL Model in Transition," NASA TN D-2380, 1964.

9. Wooler, P.T., Burghart, G.H., and Gallagher, J.T.: "Pressure Distribution on a Rectangular Wing with a Jet Exhausting Normally into an Airstream," J. of Aircraft, Vol. 4, No. 6, 1967.

10. Wu, J.D., McMahon, H.M., Mosher, D.K., and Wright, M.A.: "Experimental and Analytical Investigations of Jets Exhausting Into a Deflecting Stream," AIAA Paper No. 69-223, 1969.

11. Soukup, S.M.: "Potential Flow Aspects of the Cross-Sectional Deformation of Jet Configurations in Cross-Flow," MS Thesis, University of Tennessee Space Institute, 1968, also quoted in Ref. 17.

12. Chang, H.: "Aufrollung eines Zylindrischen Strahles durch Querwind," Doctoral Dissertation, Univ. of Göttingen, 1942.

13. Callaghan, E.E. and Ruggeri, R.S.: "Investigation of the Penetration of an Air Jet Directed Perpendicularly to an Air Stream," NACA TN-1615, 1948.

14. Callaghan, E.E. and Bowden, D.T.: "Investigation of Flow Coefficient of Circular, Square and Elliptical Orifices at High Pressure Ratios," NACA TN-1947, 1949.

15. Callaghan, E.E. and Ruggeri, R.S.: "A General Correlation of Temperature Profiles Downstream of a Heated Jet Directed Perpendicularly to an Air Stream," NACA TN-2466, 1951.

16. Jordinson, R.: "Flow in a Jet Directed Normal to the Wind," R.& M. No. 3074, British A.R.C., 1958.

17. NASA Special Report: "Analysis of a Jet in a Subsonic Crosswind," NASA SP-218.

18. Hinze, J.O.: "Turbulence, An Introduction to Its Mechanism and Theory, McGraw-Hill, New York, 1959.

19. Kamotani, Y.: "Measurement of Turbulence Quantities by Pressure Probes," MS Thesis, Case Western Reserve Univ., 1968.

20. Storms, K.R.: "Low-Speed Wind Tunnel Investigation of a Jet Directed Normal to the Wind," Rep. 885, Univ. of Washington Aeronaut. Lab., 1965.

21. Ricou, F.P. and Spalding, D.B.: "Measurements of Entrainment by Axisymmetrical Turbulent Jets," J. of Fluid Mech., Vol. 11, Part 1, 1961.

22. Pratte, B.D. and Baines, W.D.: "Profiles of the Round Turbulent Jet in a Cross Flow," J. of Hydraulics Div, Amer. Soc. of Civil Eng., Vol. 92, No. HY6, 1967.

23. Kronauer, R.: "The Behavior of Jets in Cross Flow," Boeing Scientific Res. Lab., TM No. 56, 1968.

24. Townsend, A.A.: "Entrainment and the Structure of Turbulent Flow," J. of Fluid Mech., Vol. 41, part 1, 1970.

25. Townsend, A.A.: "The Mechanism of Entrainment in Free Turbulent Flows," J. of Fluid Mech., Vol. 26, part 4, 1966.

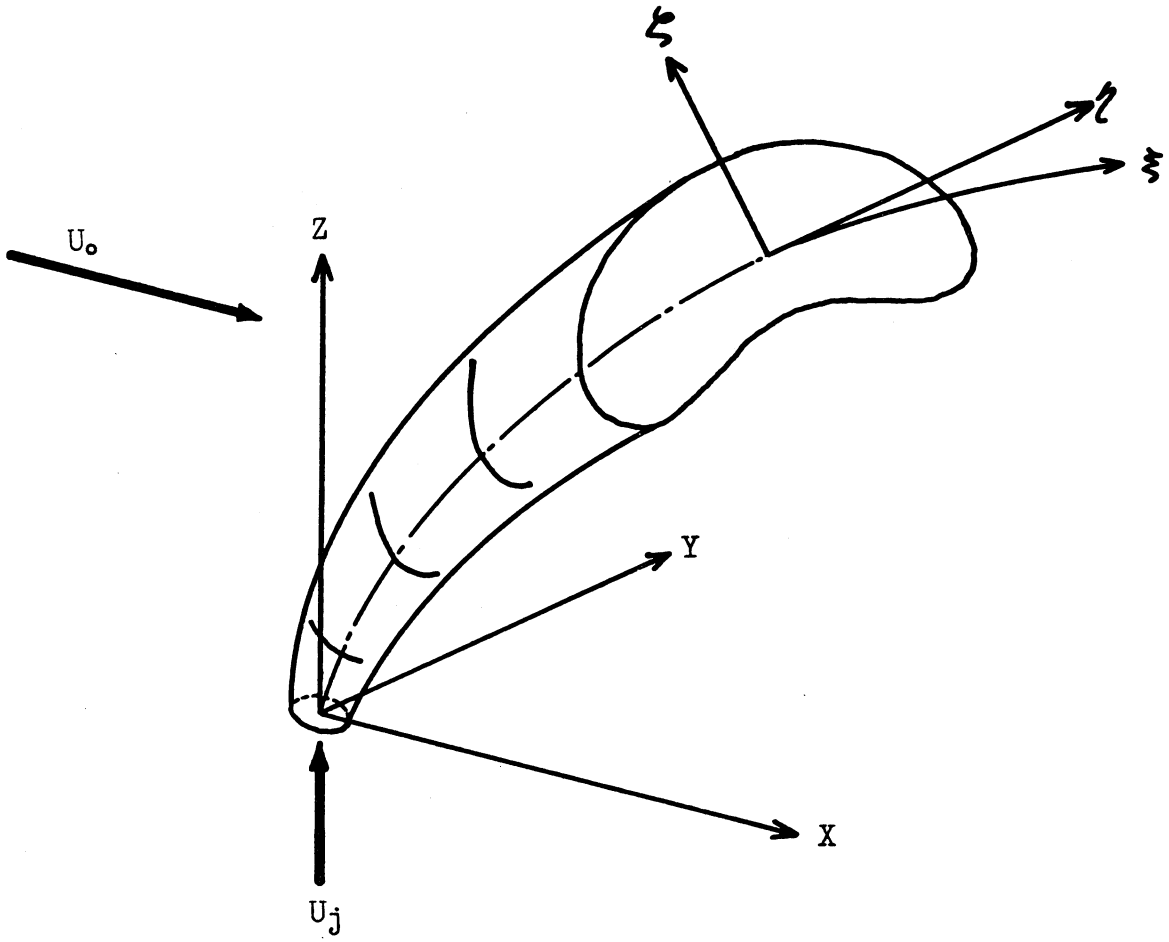

Figure 1. Coordinate System

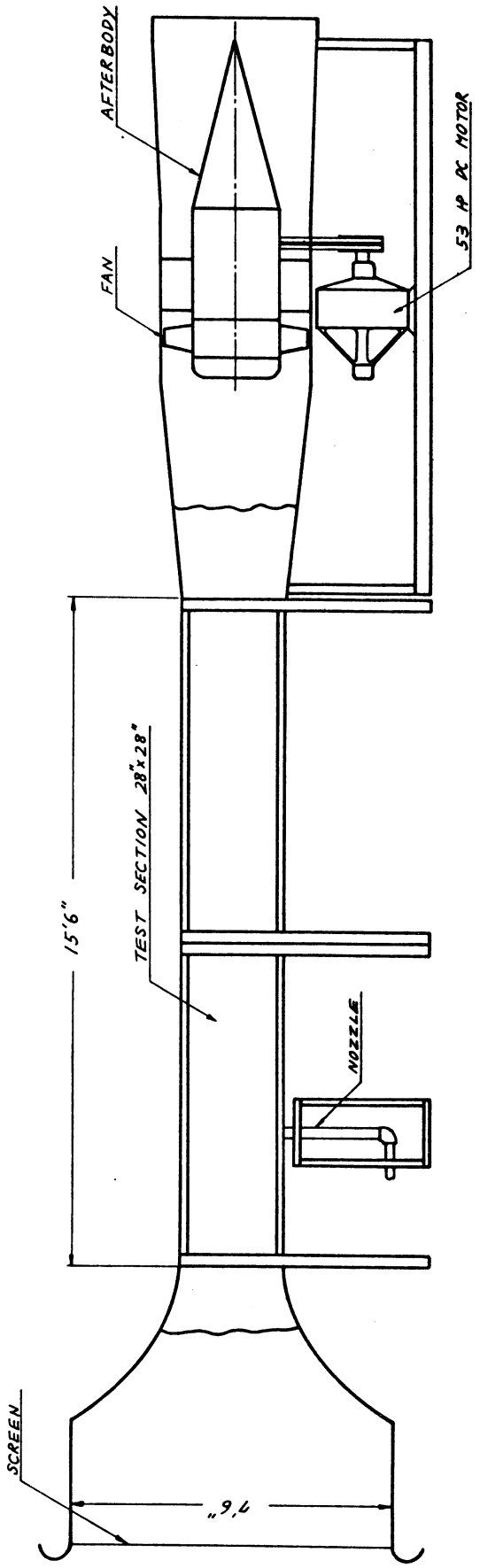

Figure 2. Sketch of Wind Tunnel

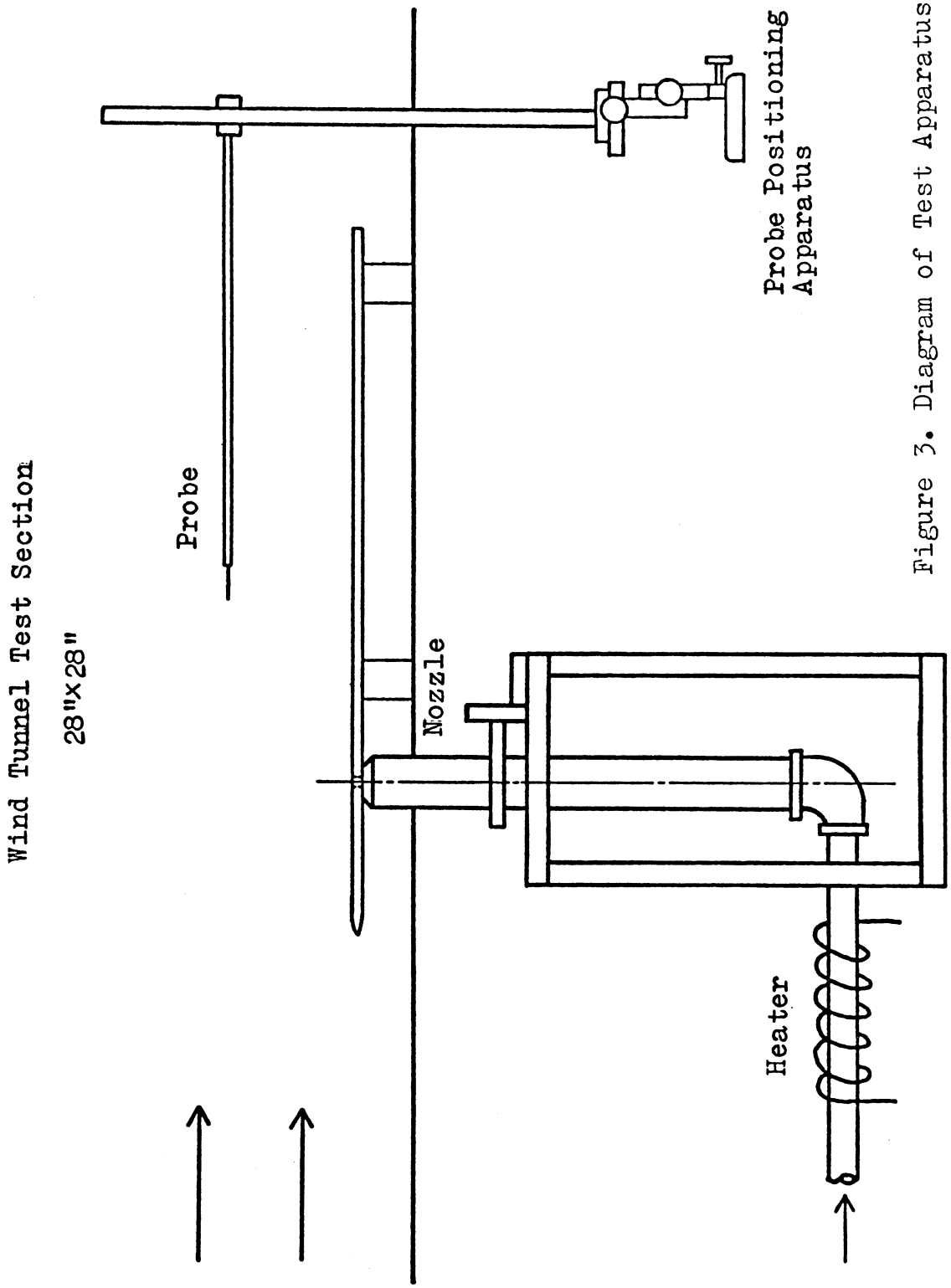

Figure 3. Diagram of Test Apparatus

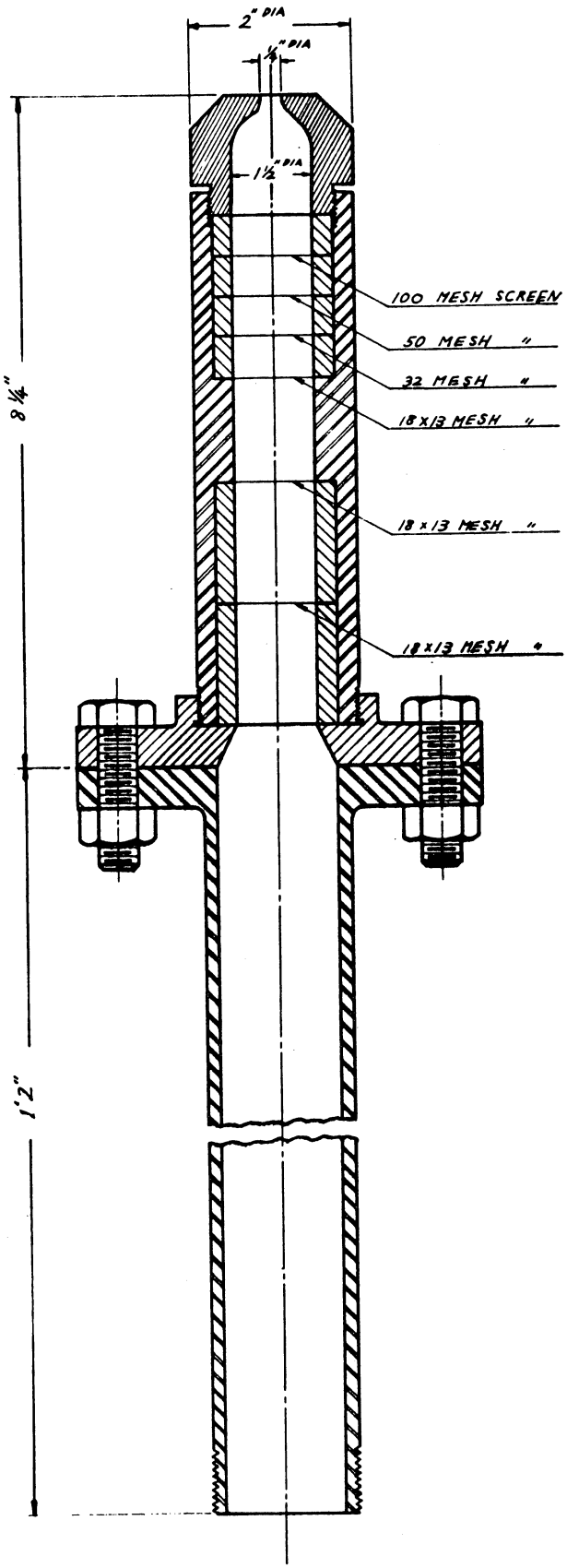

Figure 4. Structure of Nozzle

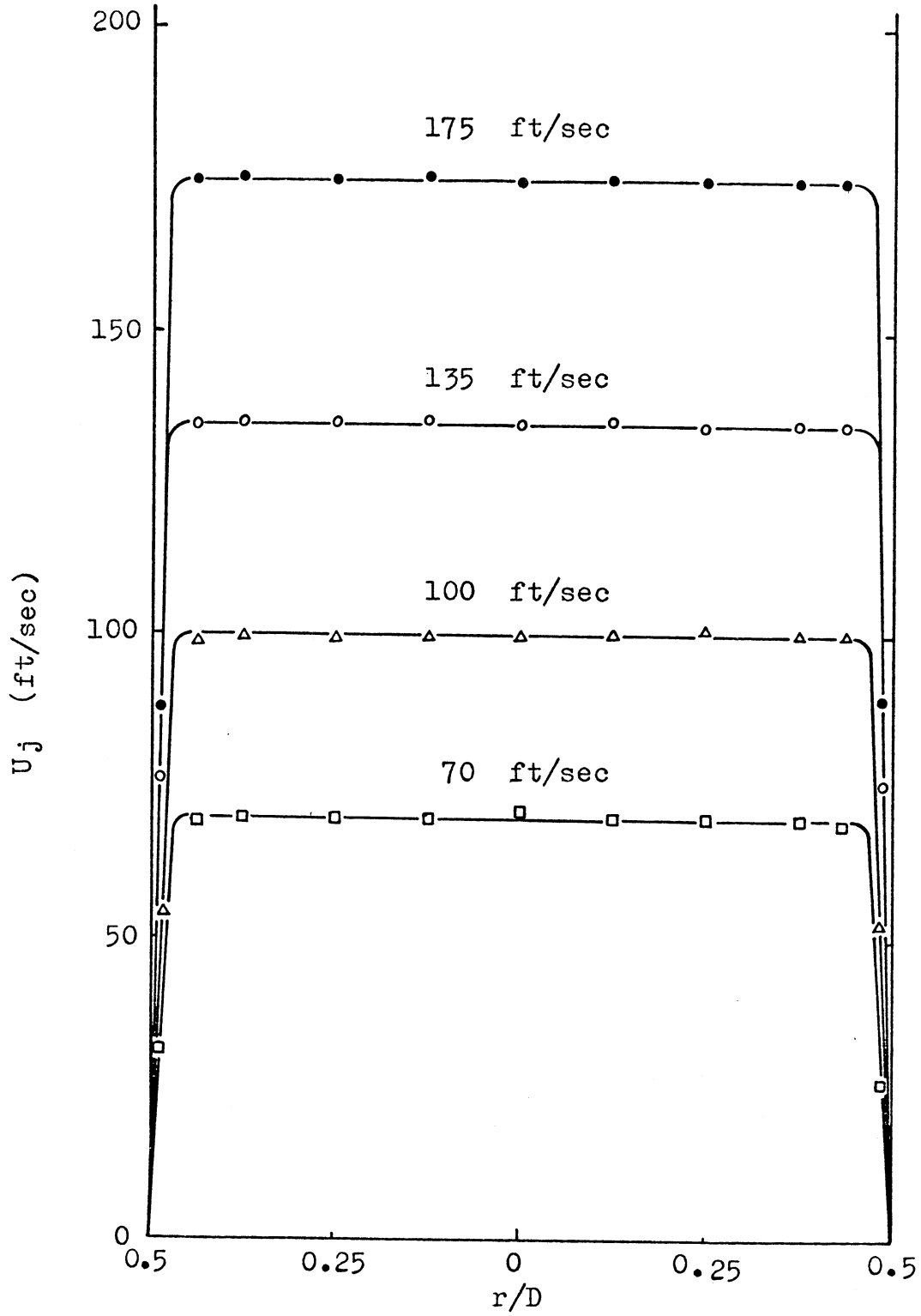

Figure 5. Initial Velocity Profiles of Jet

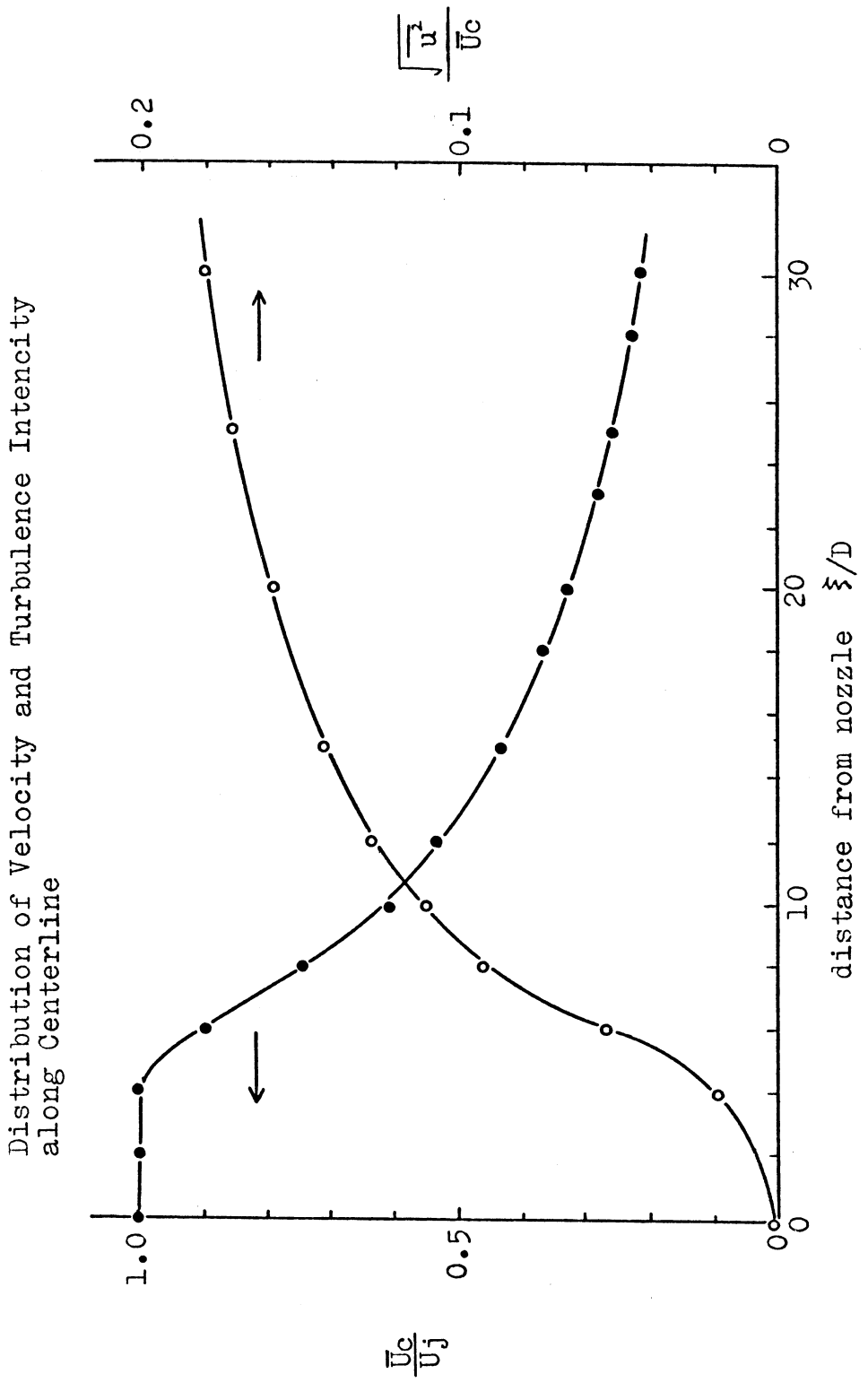

Figure 6. Behavior of Free Jet from 1/4 in. Nozzle

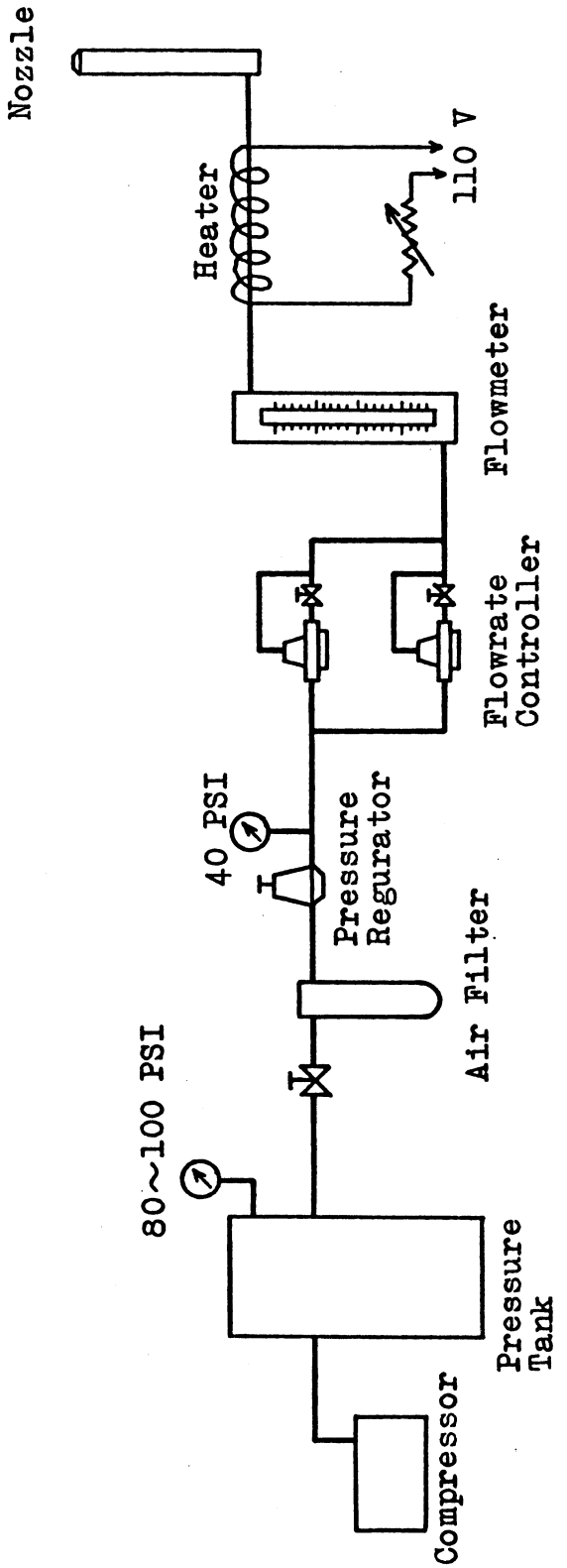

Figure 7. Air Supply System

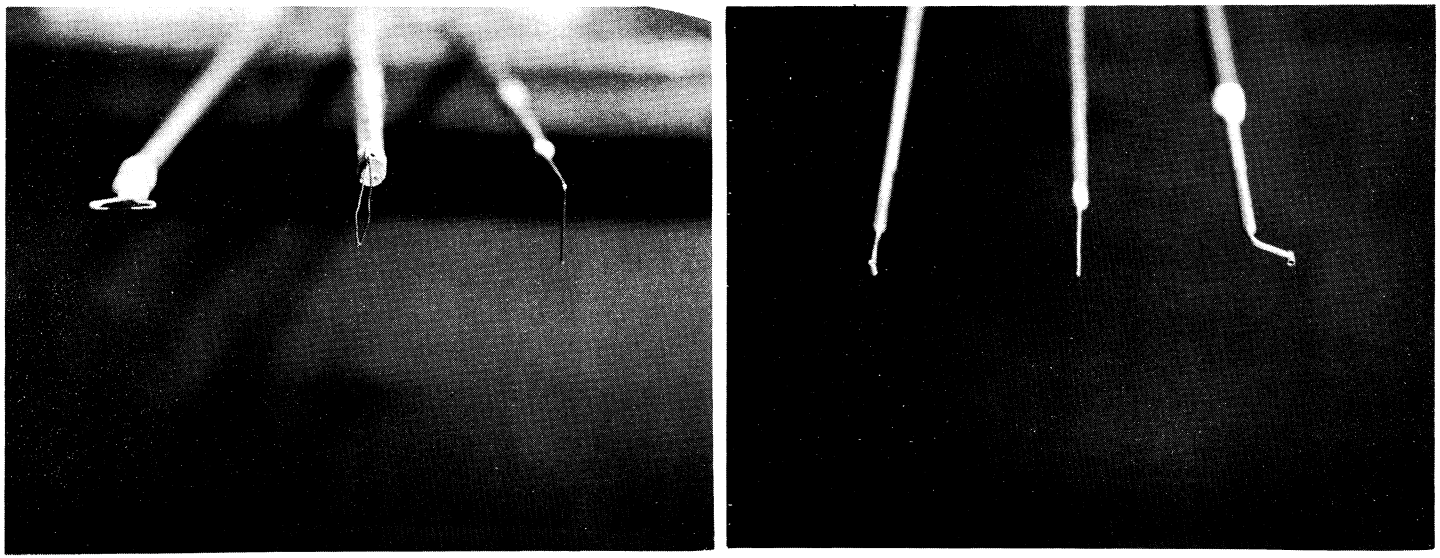

From left to right:
1. Hot Wire
2. Thermocouple
3. Total Head Tube
4. Kiel Total Head Probe
5. Pitot Static Tube
6. Kiel Total Head Tube

Figure 8. Measuring Probes

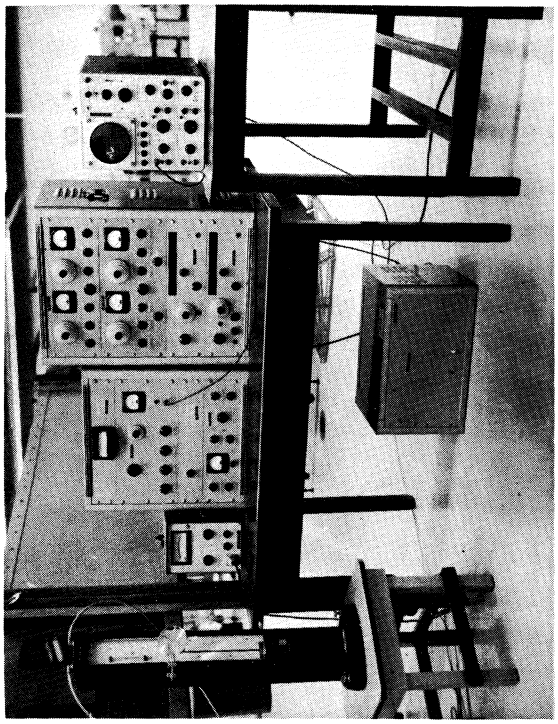

Figure 9. Constant-Current Hot Wire Set

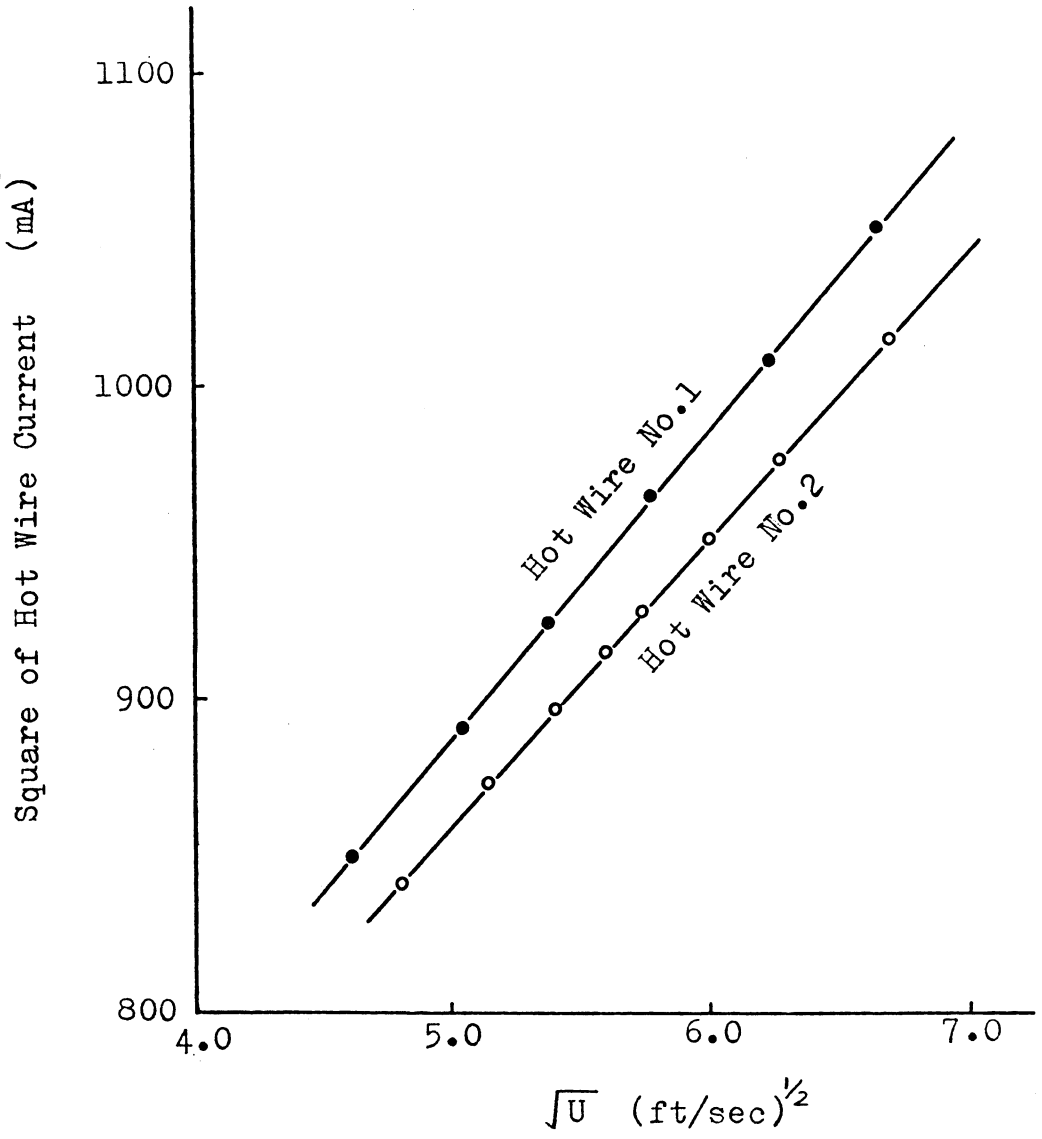

Figure 10. Examples of Hot Wire Calibration Curve

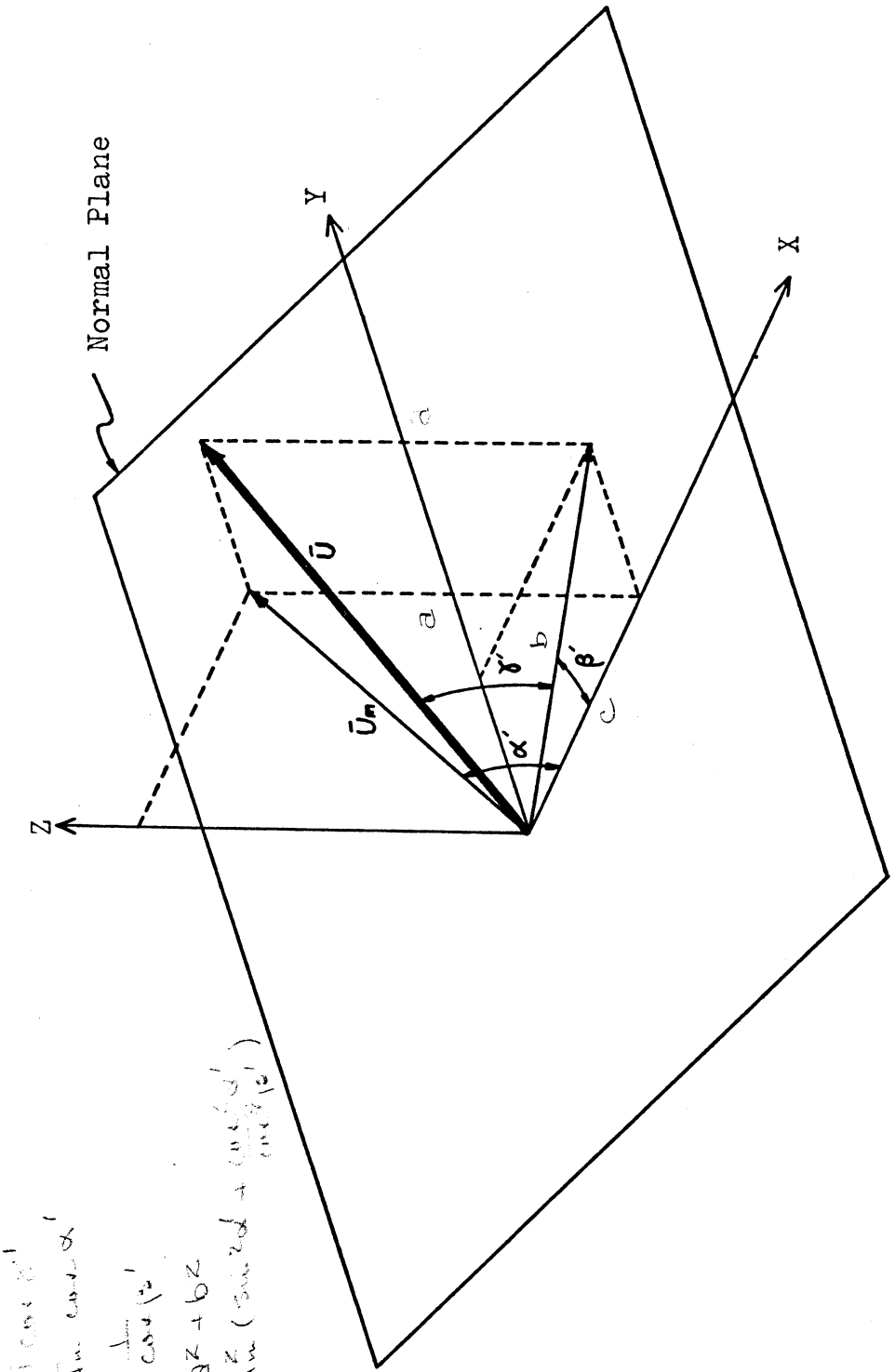

Figure 11. Diagram of Flow Direction Coordinates

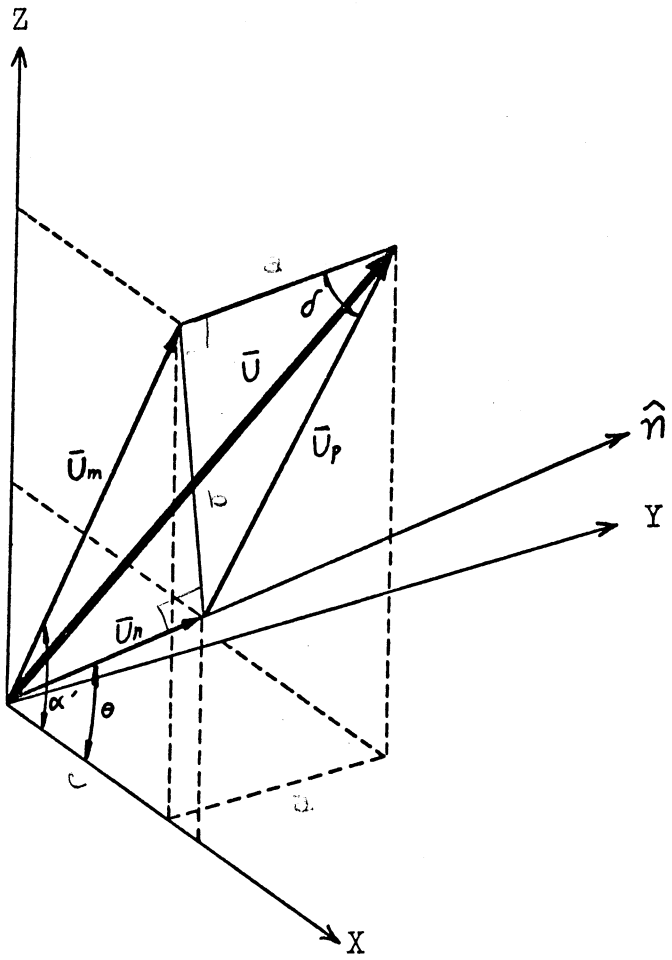

Figure 12. Normal and Parallel Velocity Components

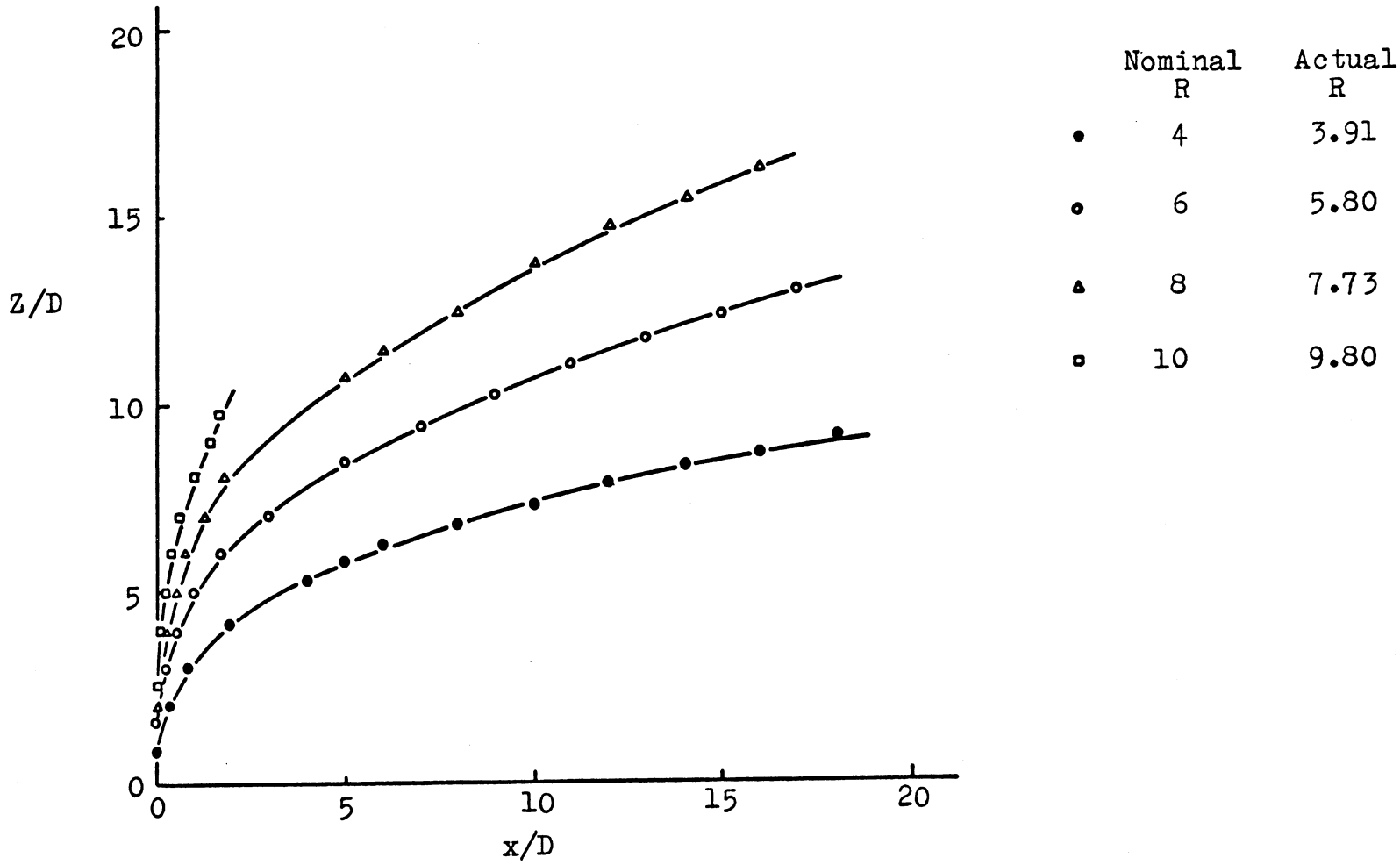

Figure 13. Location of Jet Velocity Centerline

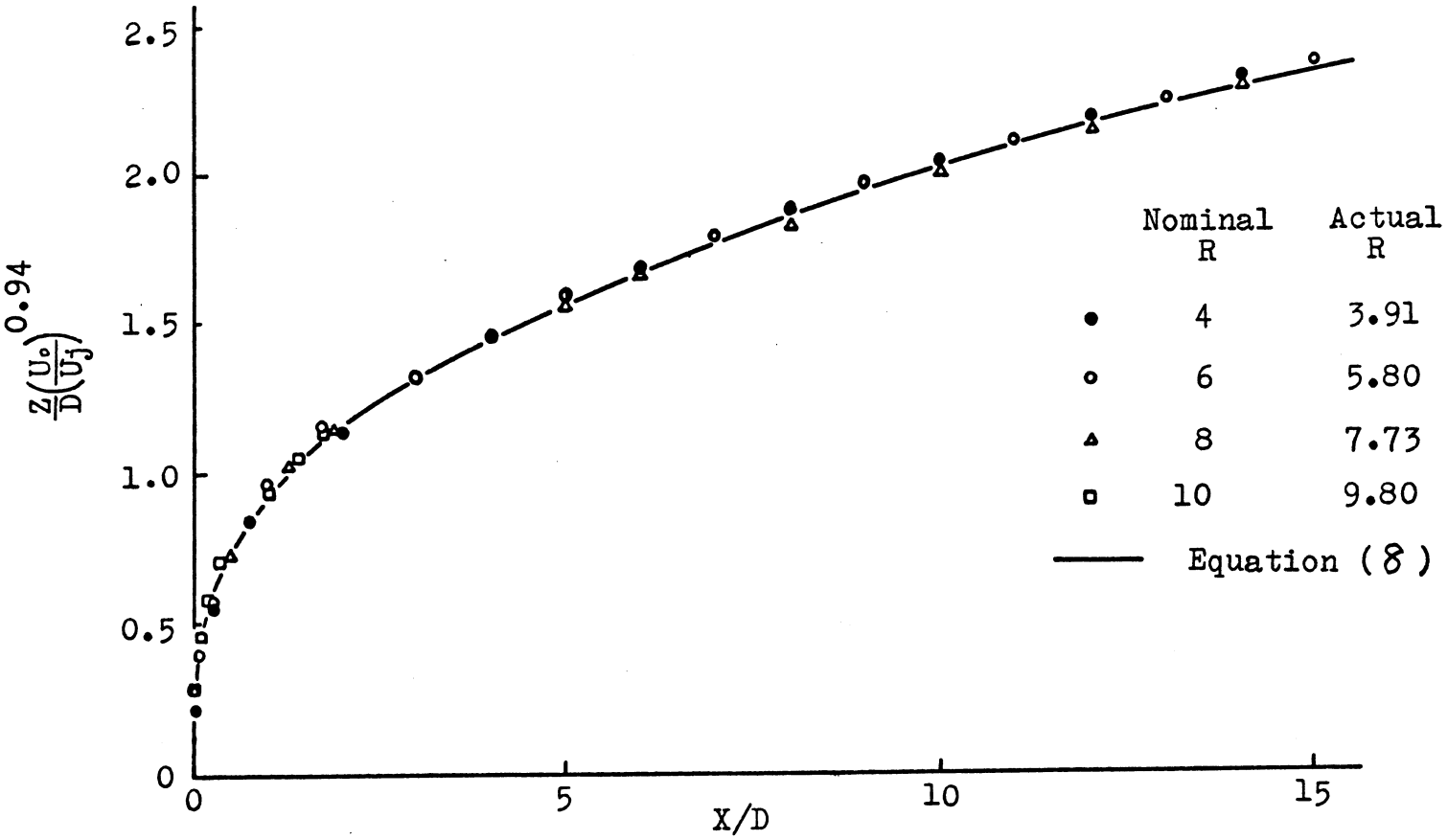

Figure 14. Correlation of Jet Velocity Centerline Location

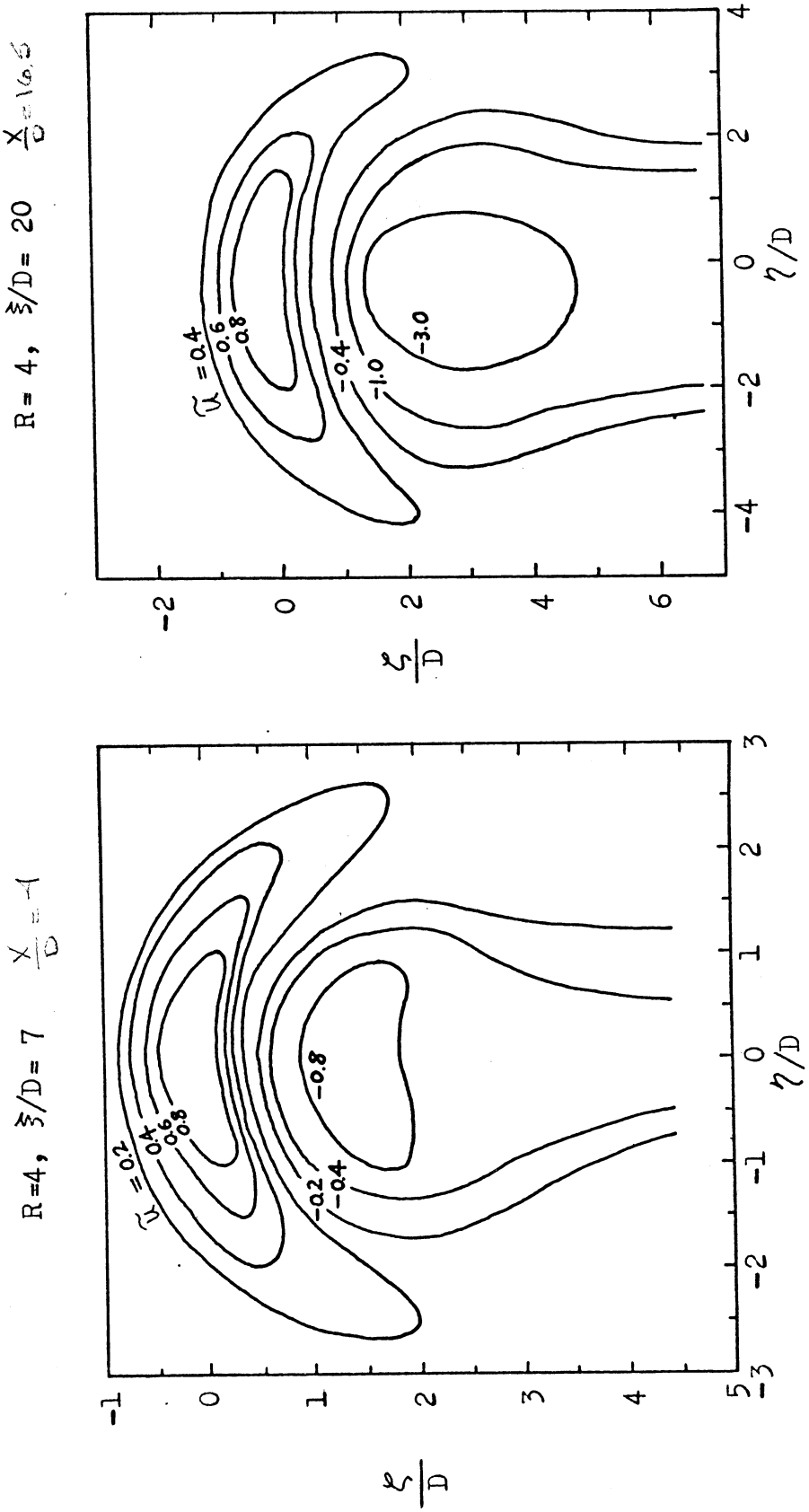

Figure 15. Contours of Constant Velocity

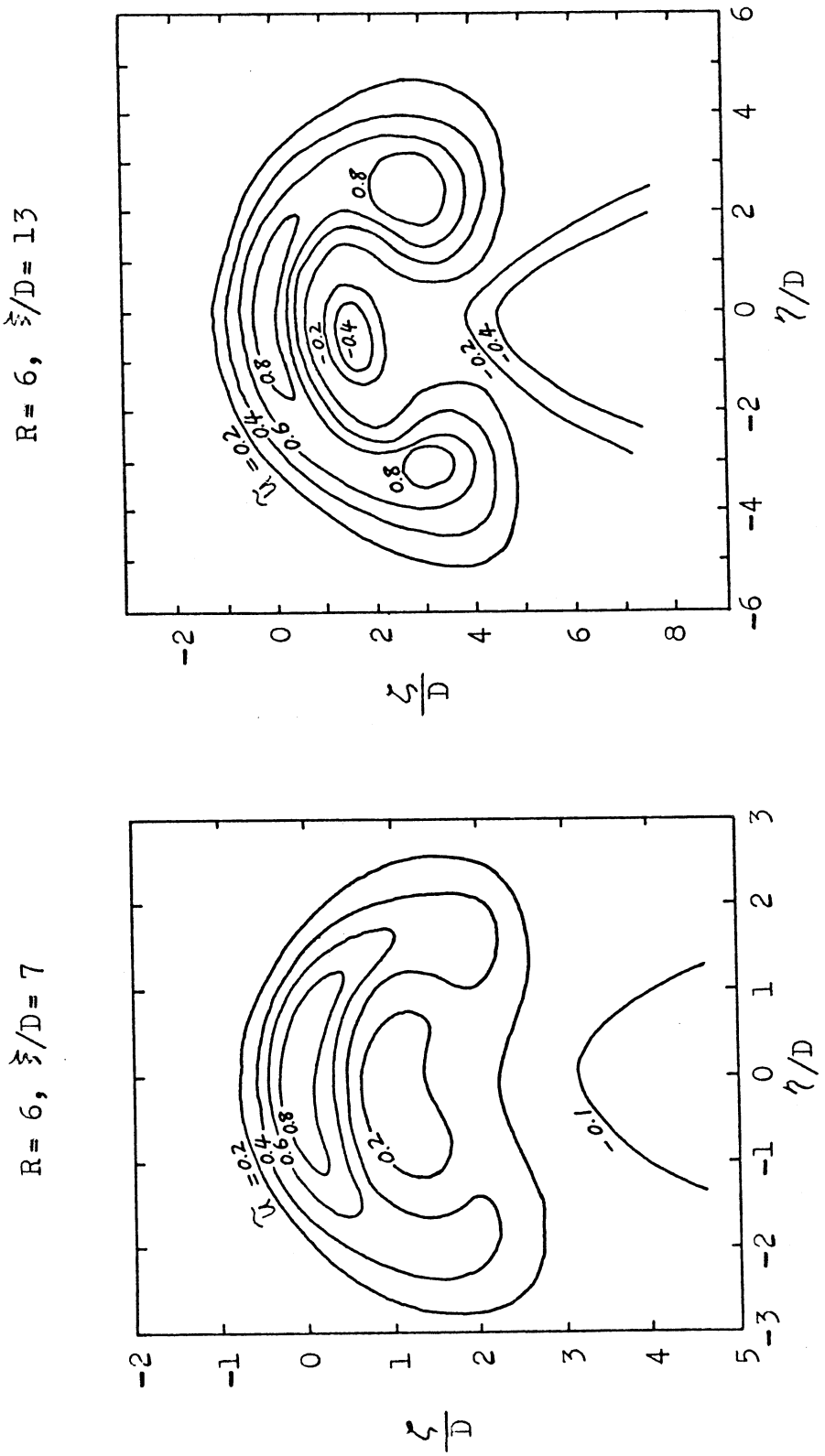

Figure 16. Contours of Constant Velocity

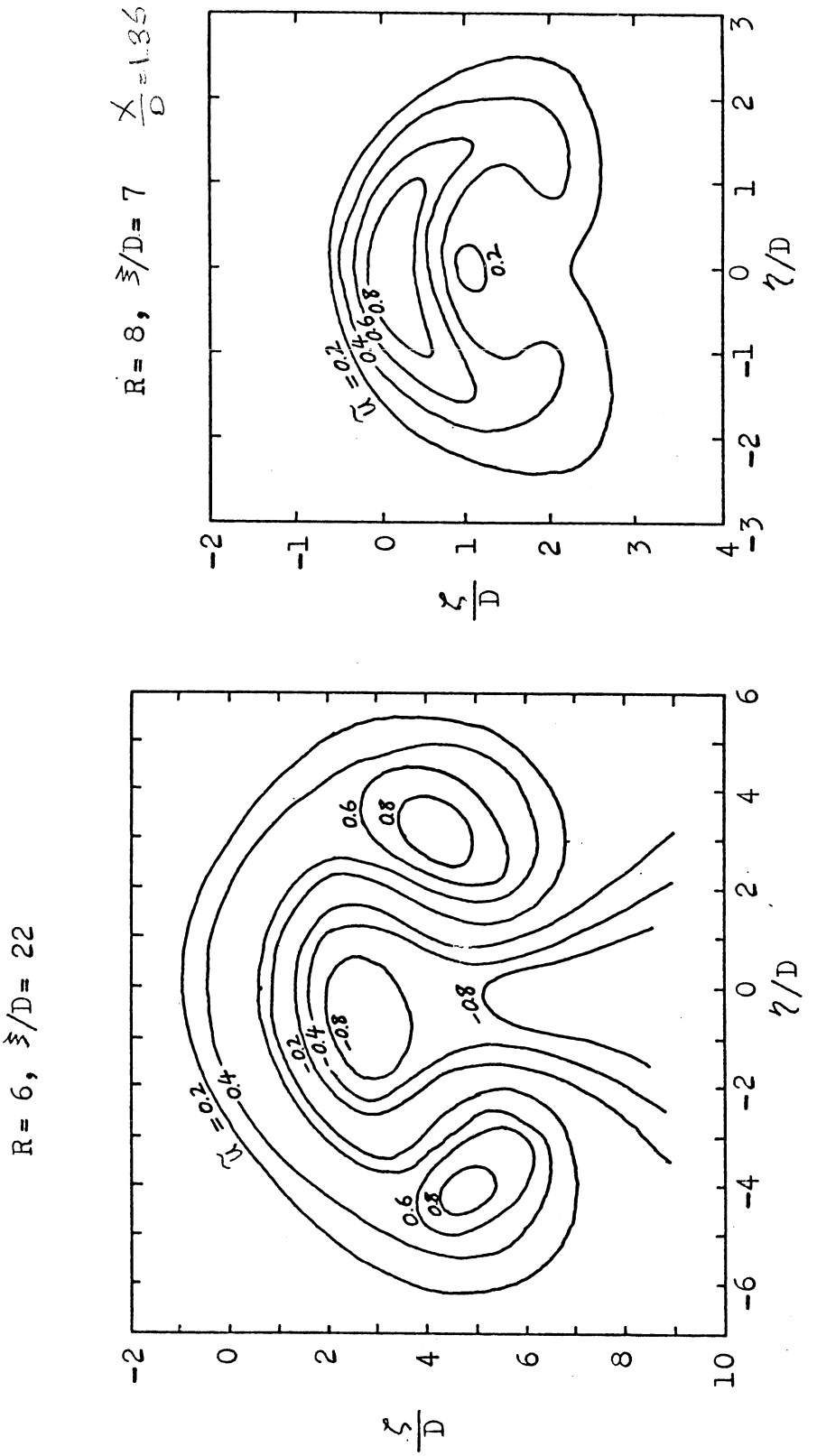

Figure 17. Contours of Constant Velocity

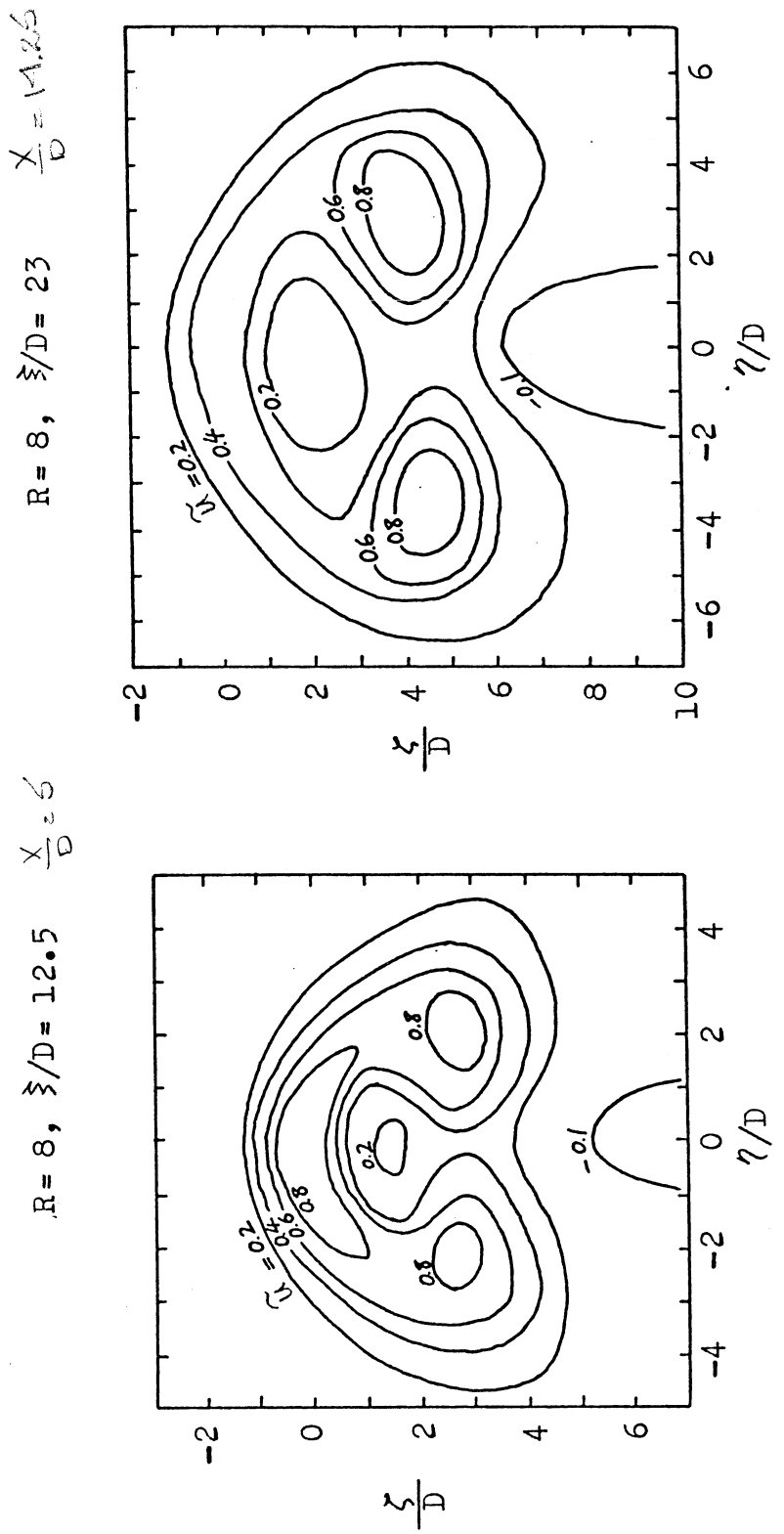

Figure 18. Contours of Constant Velocity

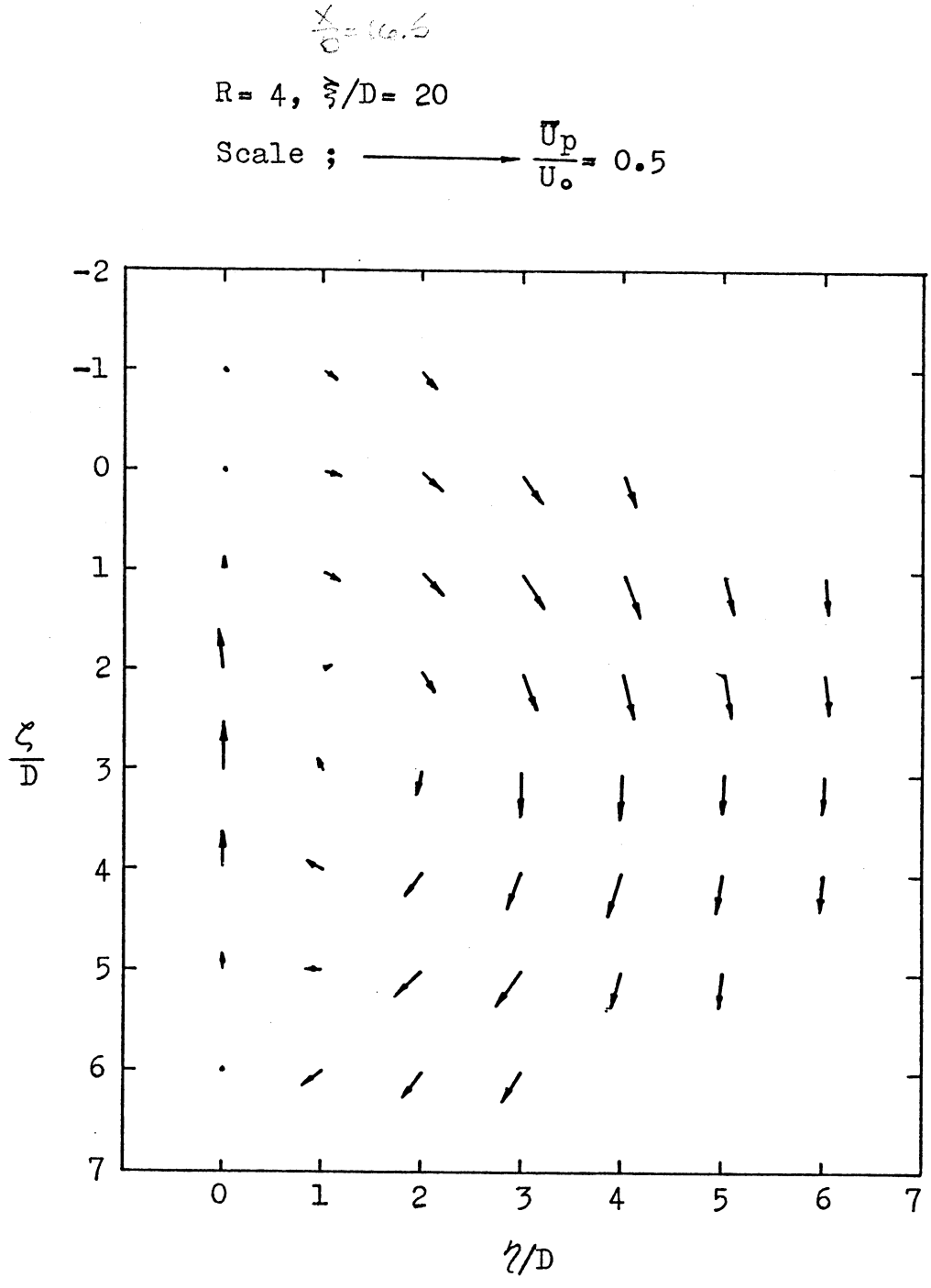

Figure 19. Projection Of Velocity Vectors on Normal Plane

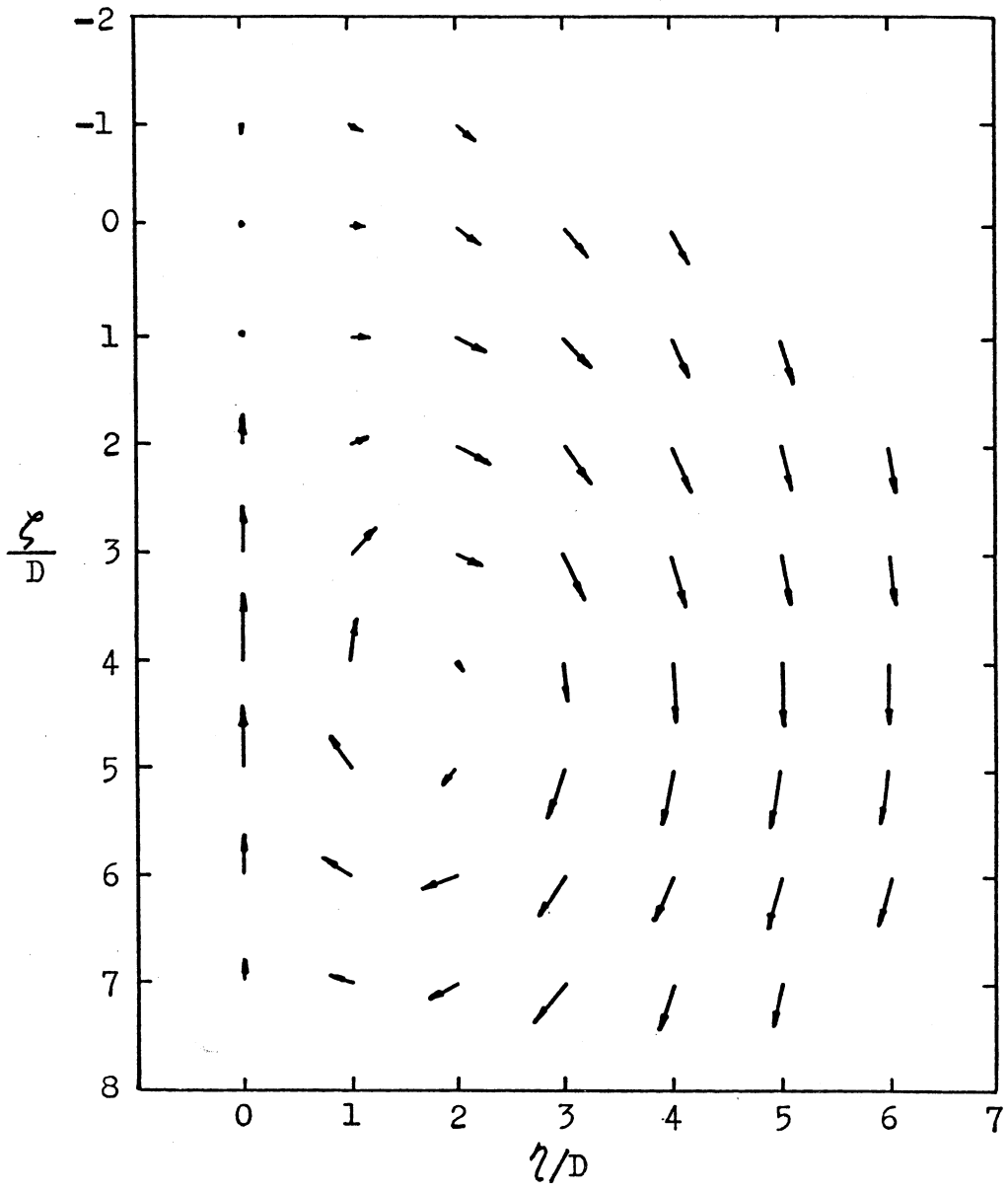

Figure 20. Projection of Velocity Vectors on Normal Plane

$\frac{x}{D} = 14.25$

R= 8, $\bar{x}/D = 23$

Scale ; ⟶ $\frac{\bar{U}_p}{U_o} = 0.5$

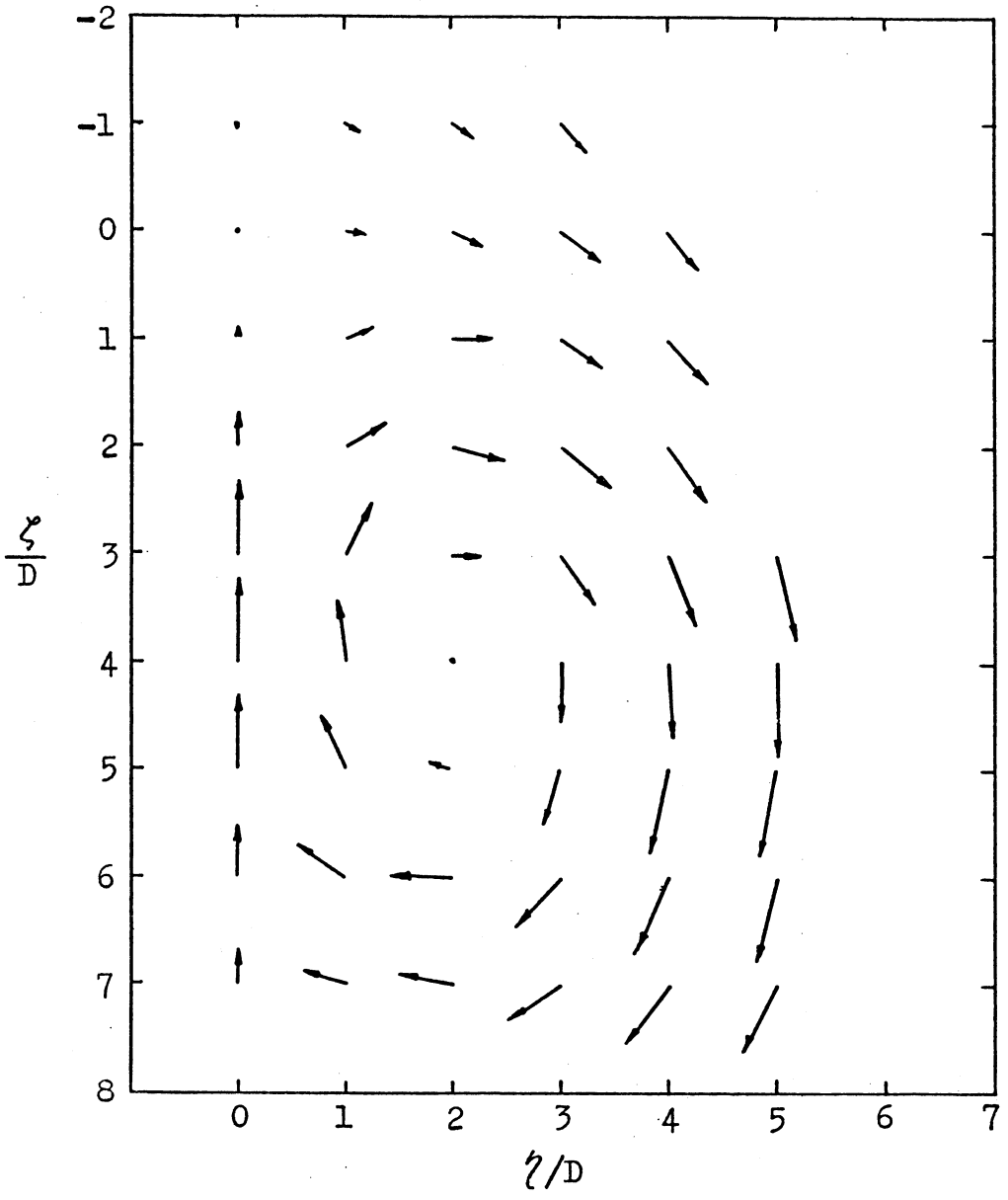

Figure 21. Projection of Velocity Vectors on Normal Plane

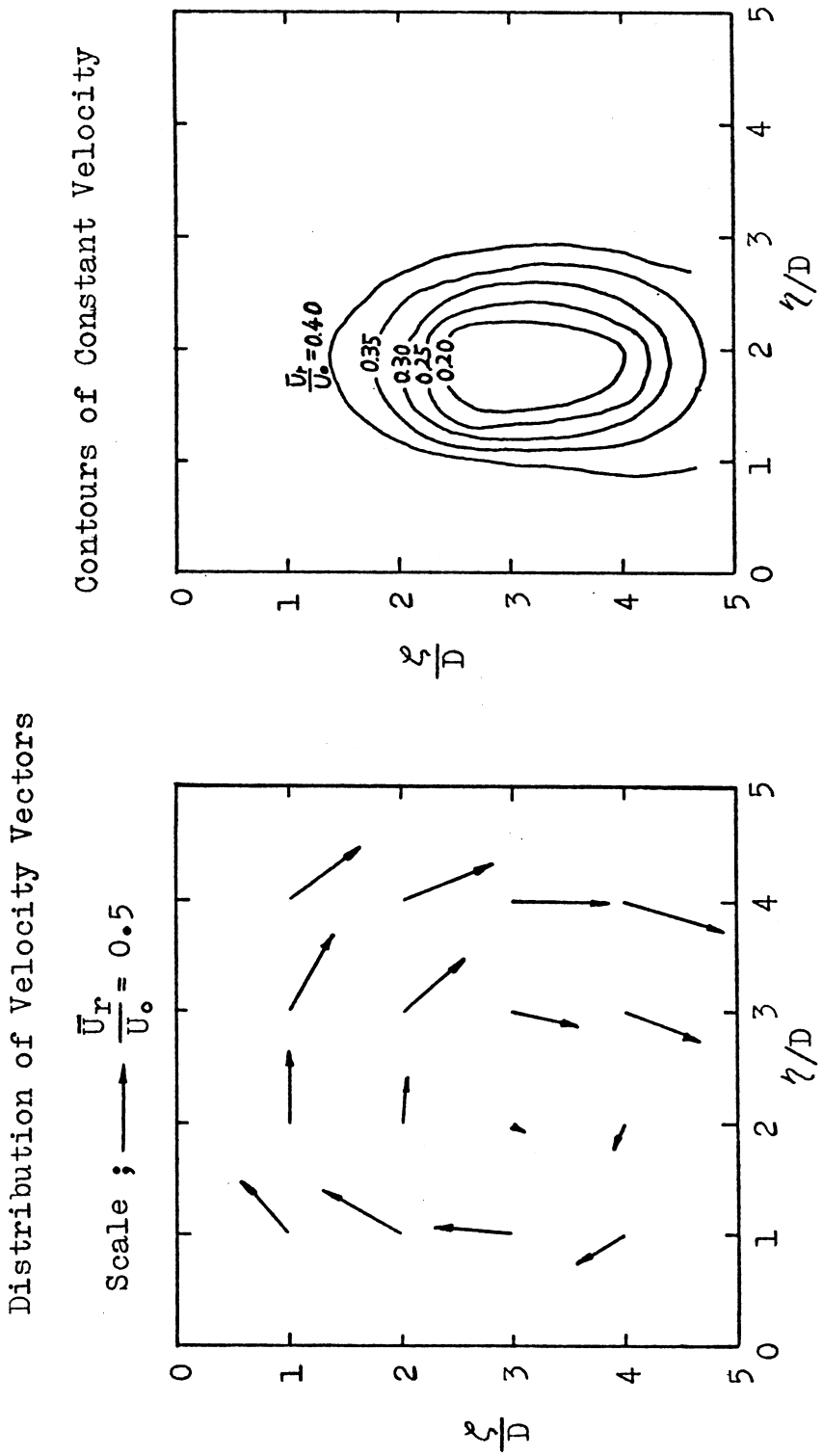

Figure 22. Rotational Velocity Field in Vortex Region

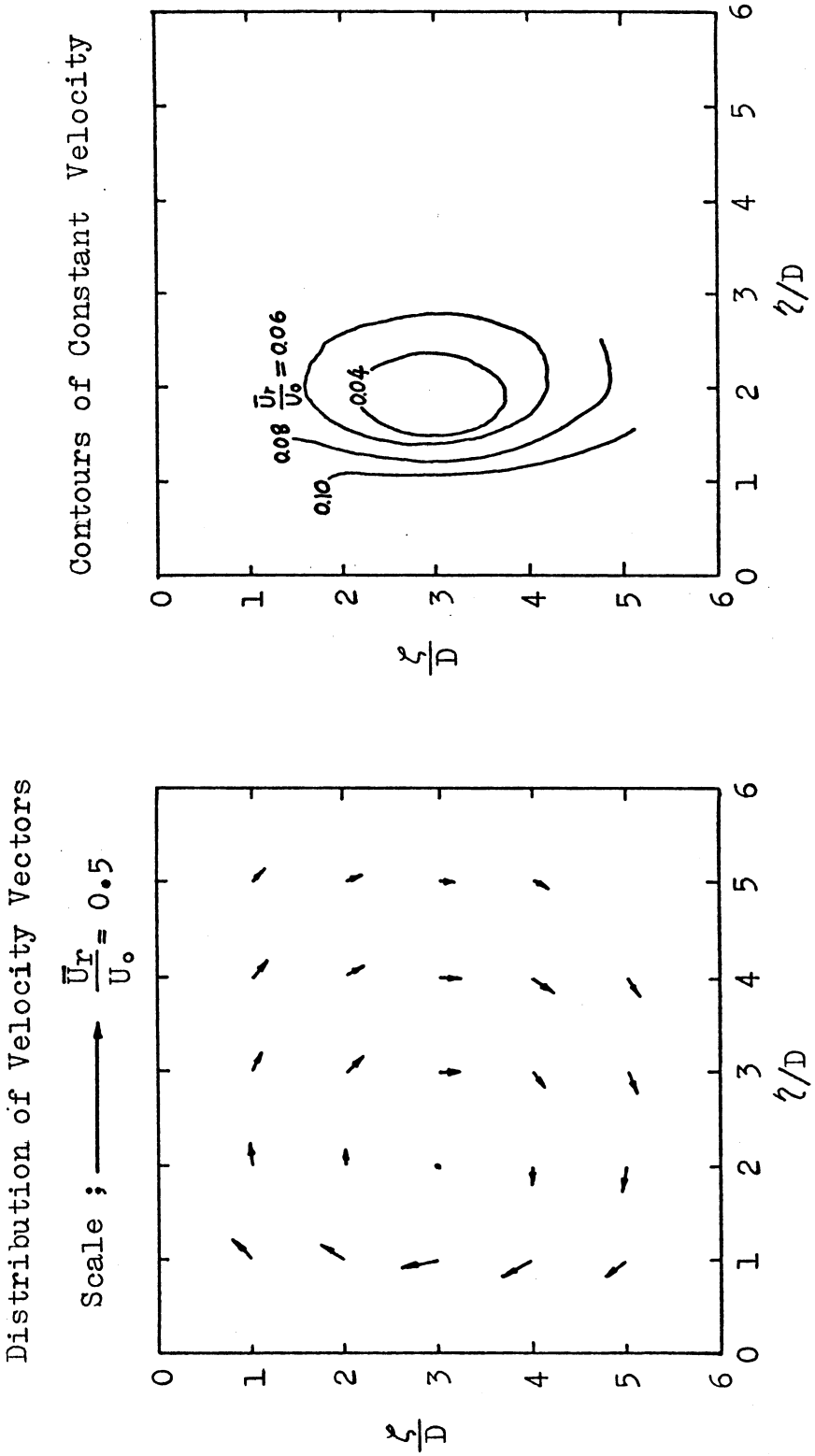

Figure 23. Rotational Velocity Field in Vortex Region

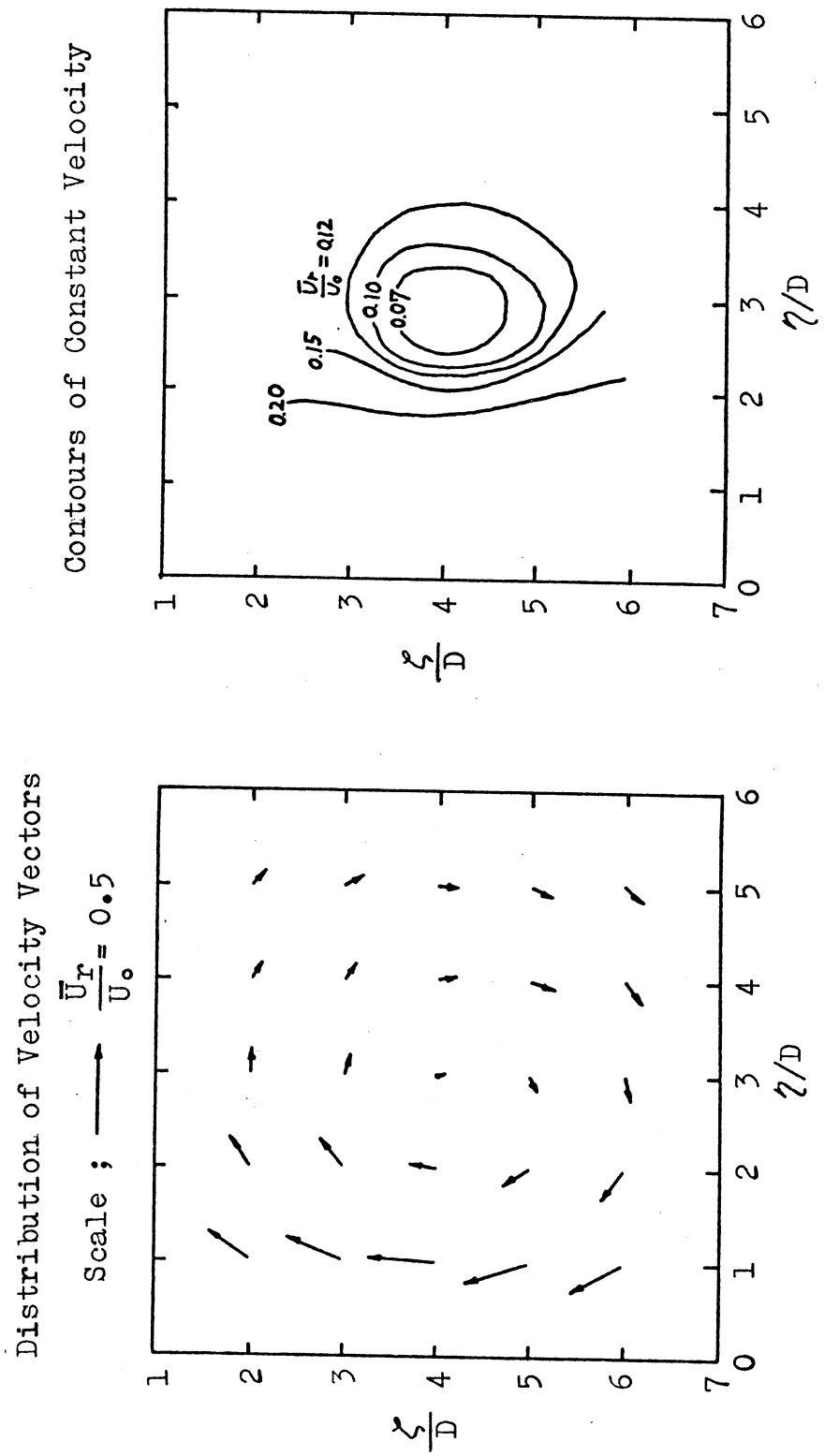

Figure 24. Rotational Velocity Field in Vortex Region

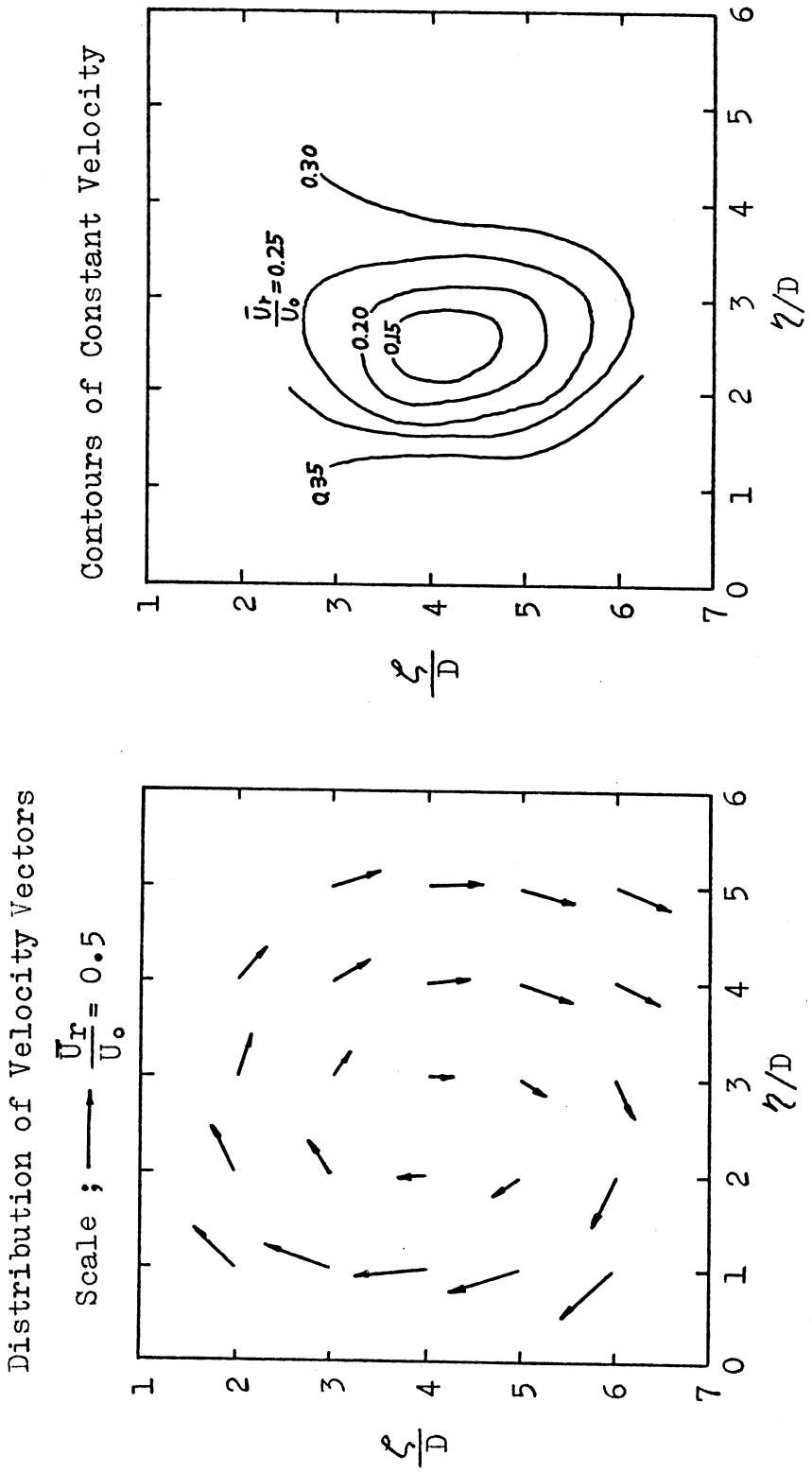

Figure 25. Rotational Velocity Field in Vortex Region

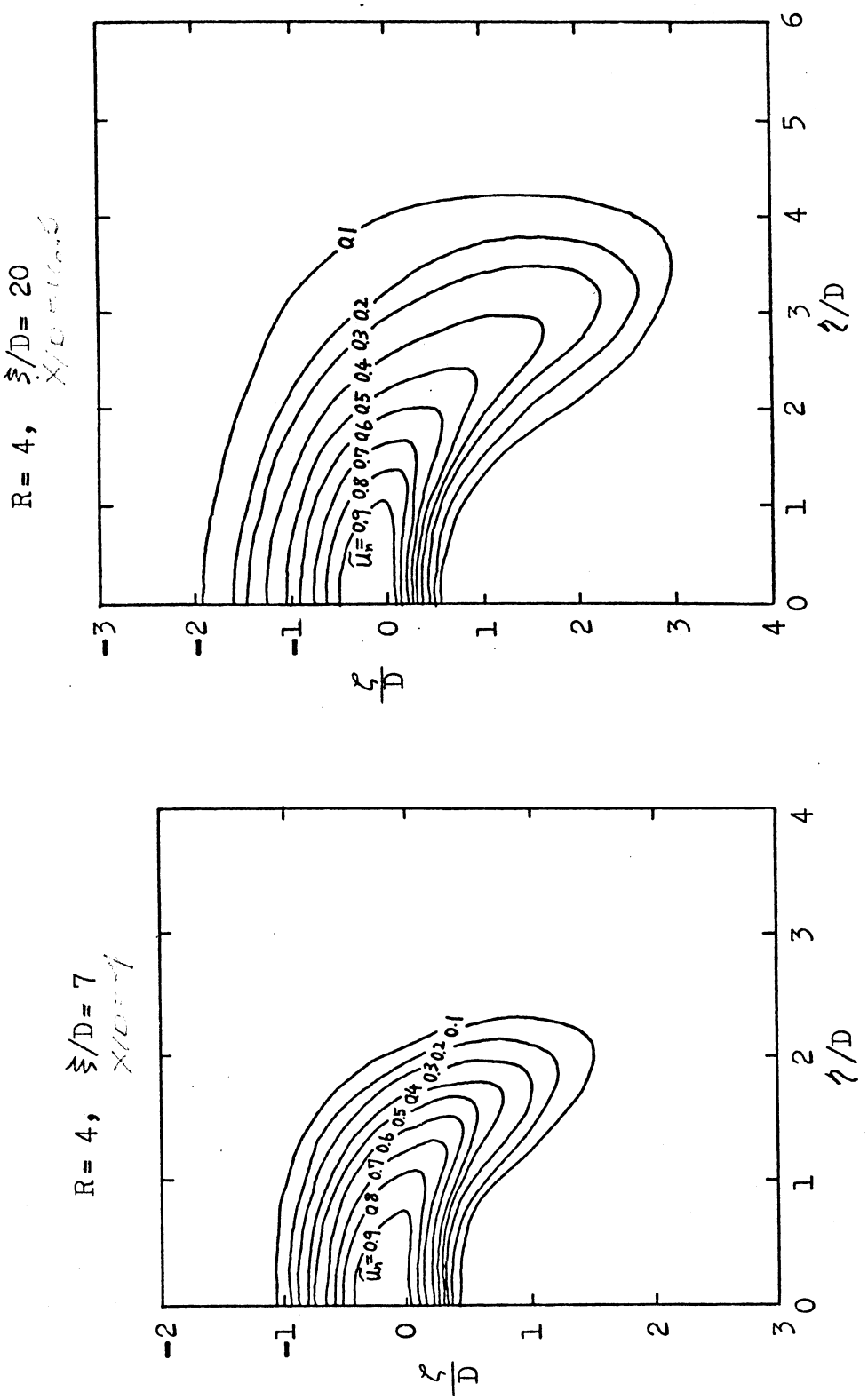

Figure 26. Contours of Constant Normal Velocity

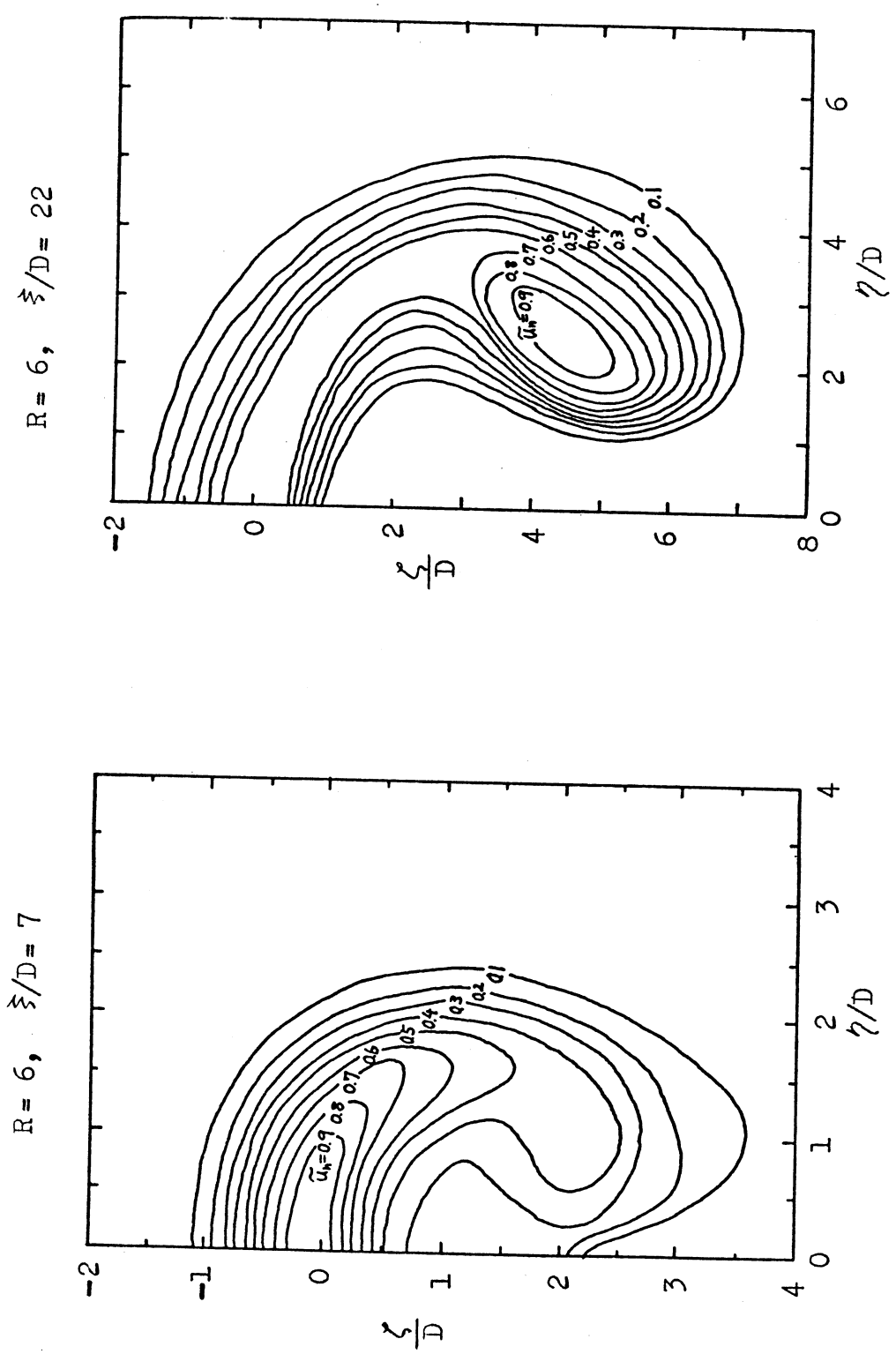

Figure 27. Contours of Constant Normal Velocity

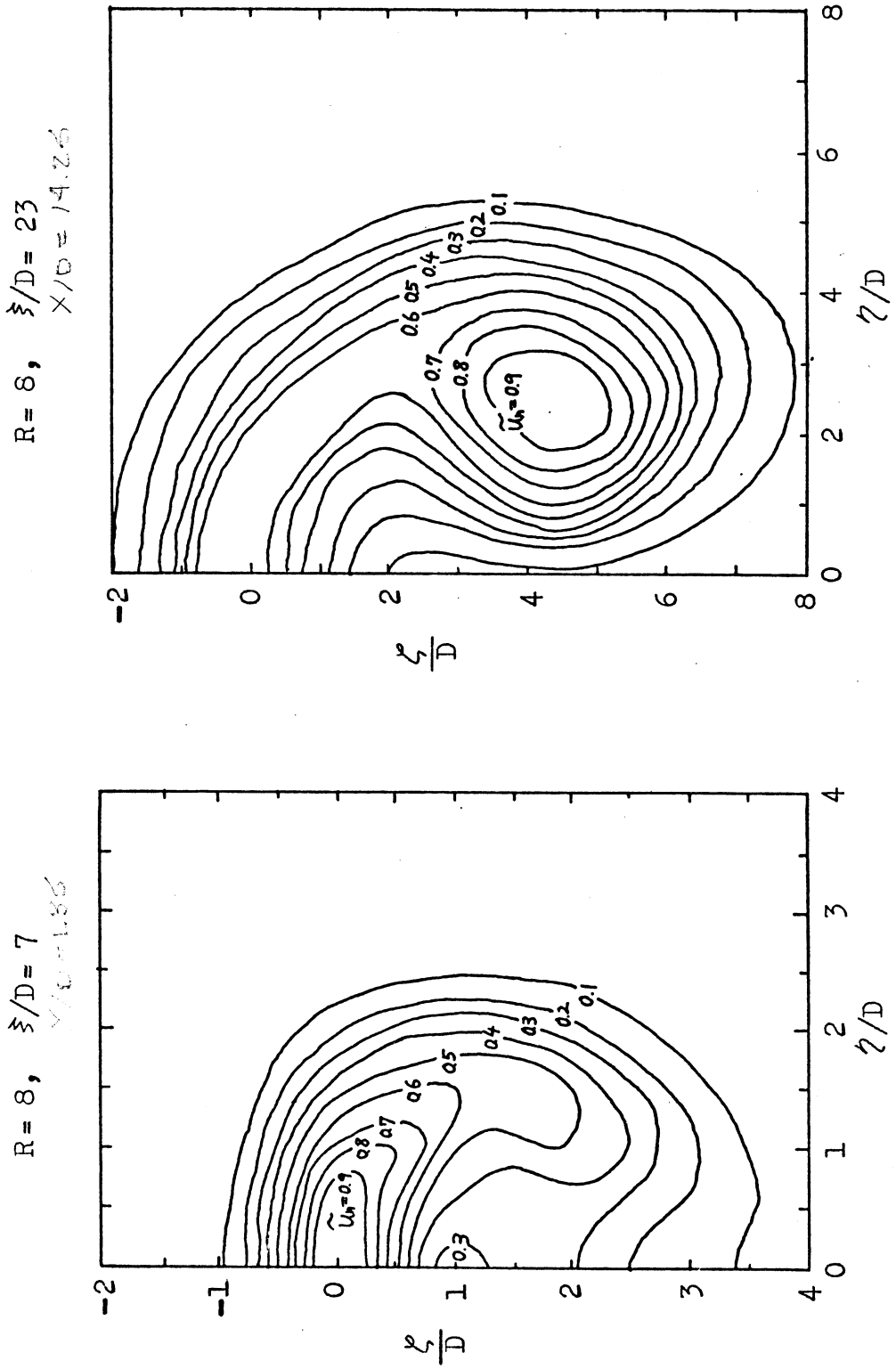

Figure 28. Contours of Constant Normal Velocity

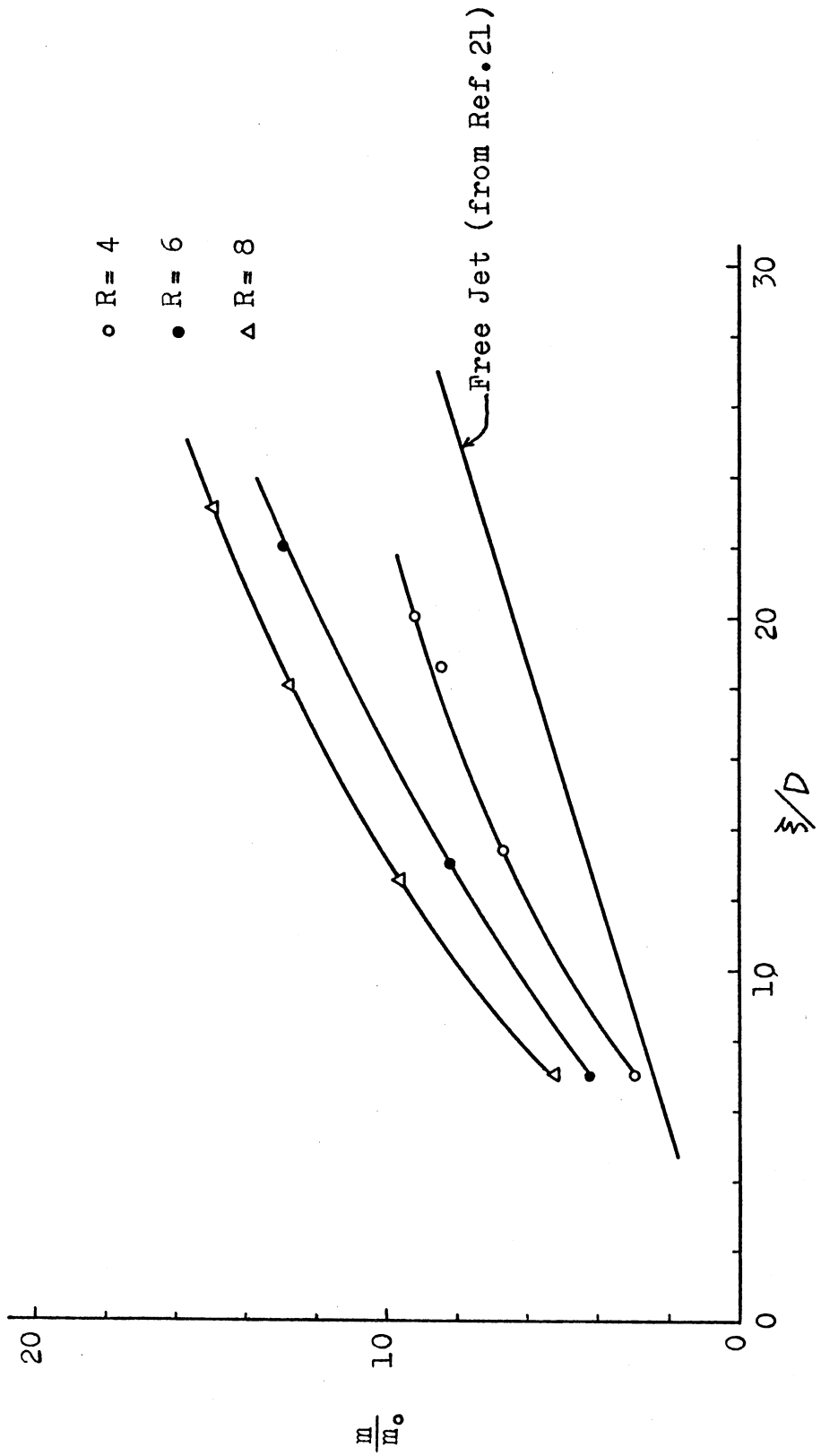

Figure 29. Mass Flux in Jet

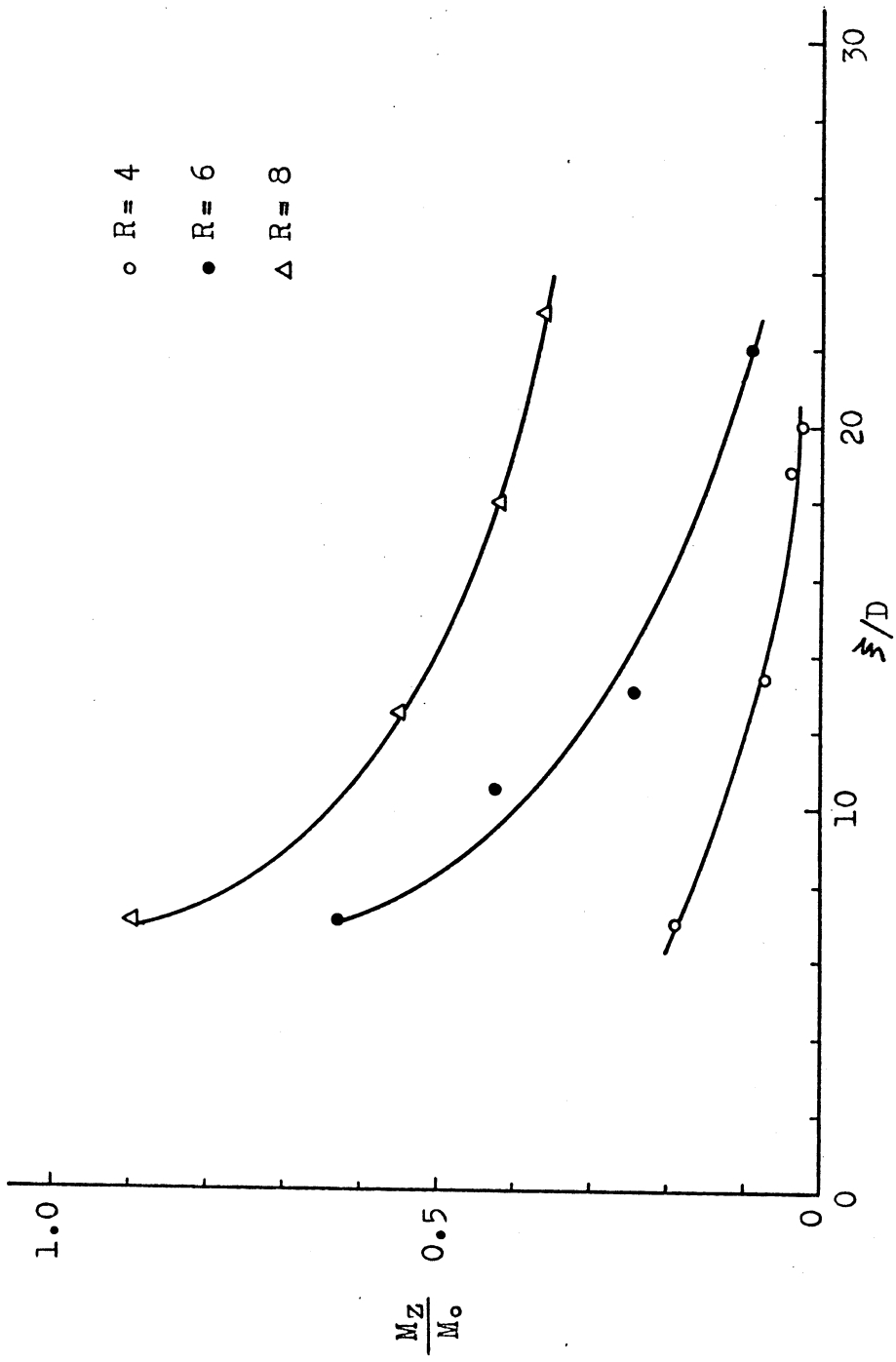

Figure 30. Distribution of Z-Momentum Flux

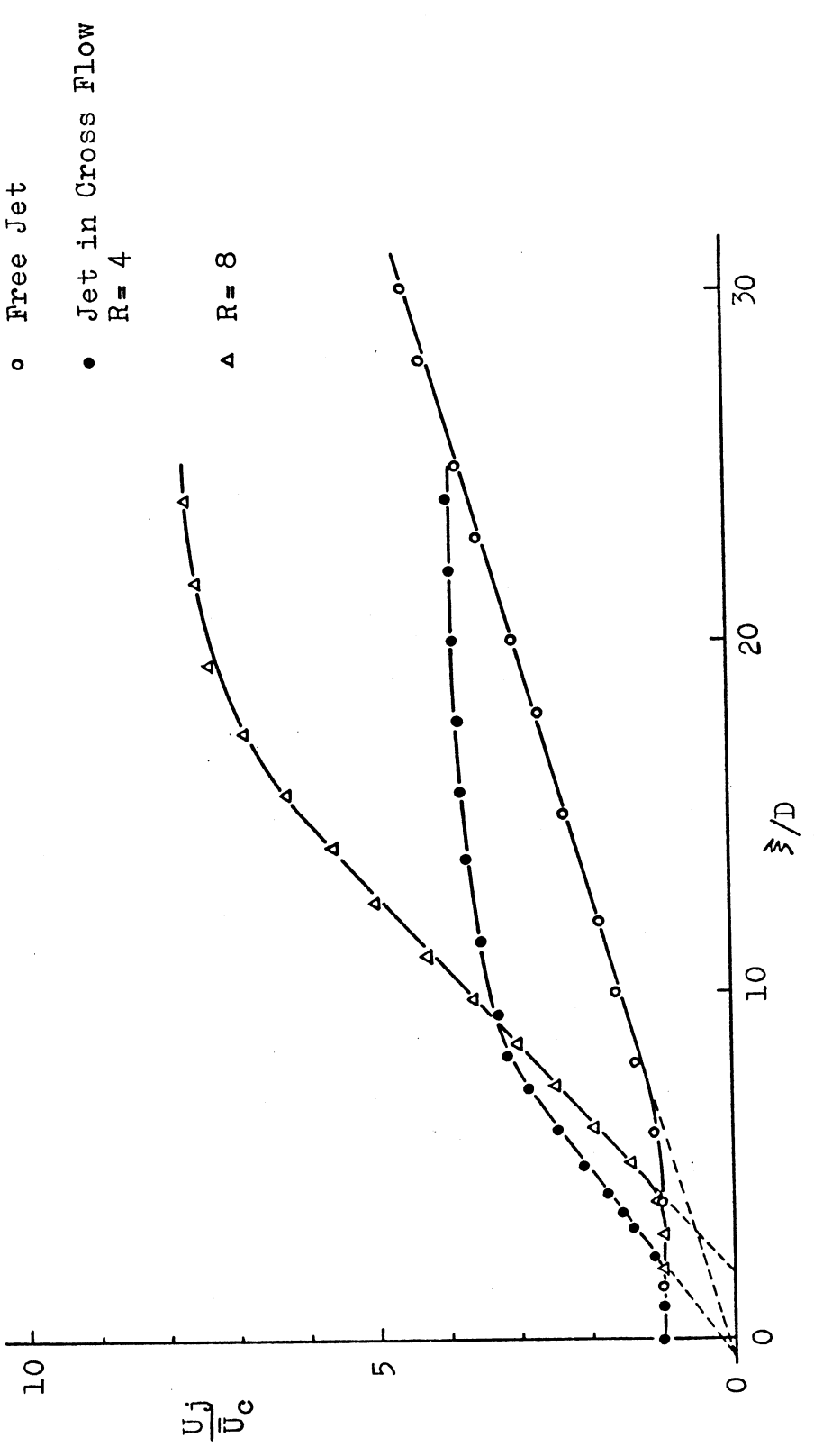

Figure 31. Distribution of Velocity along Jet Velocity Centerline

$$R = 4, \quad X/D = 15 \qquad C_{pt} = \frac{\overline{P_t} - P_{t_o}}{\frac{1}{2}\rho U_o^2}$$

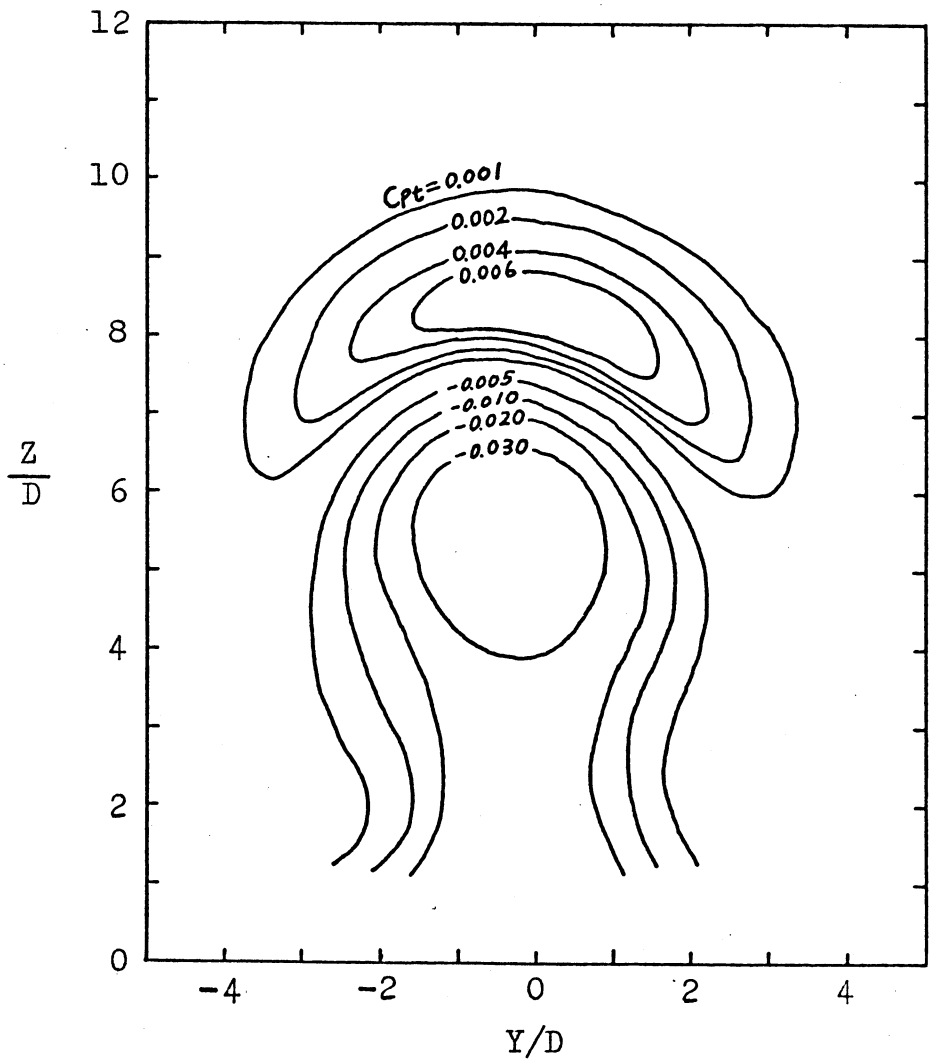

Figure 32. Total Pressure Distribution

Referenced on pg 35

$$R = 4, \quad X/D = 15, \quad C_p = \frac{\overline{P_s} - P_{s_o}}{\frac{1}{2}\rho U_o^2}$$

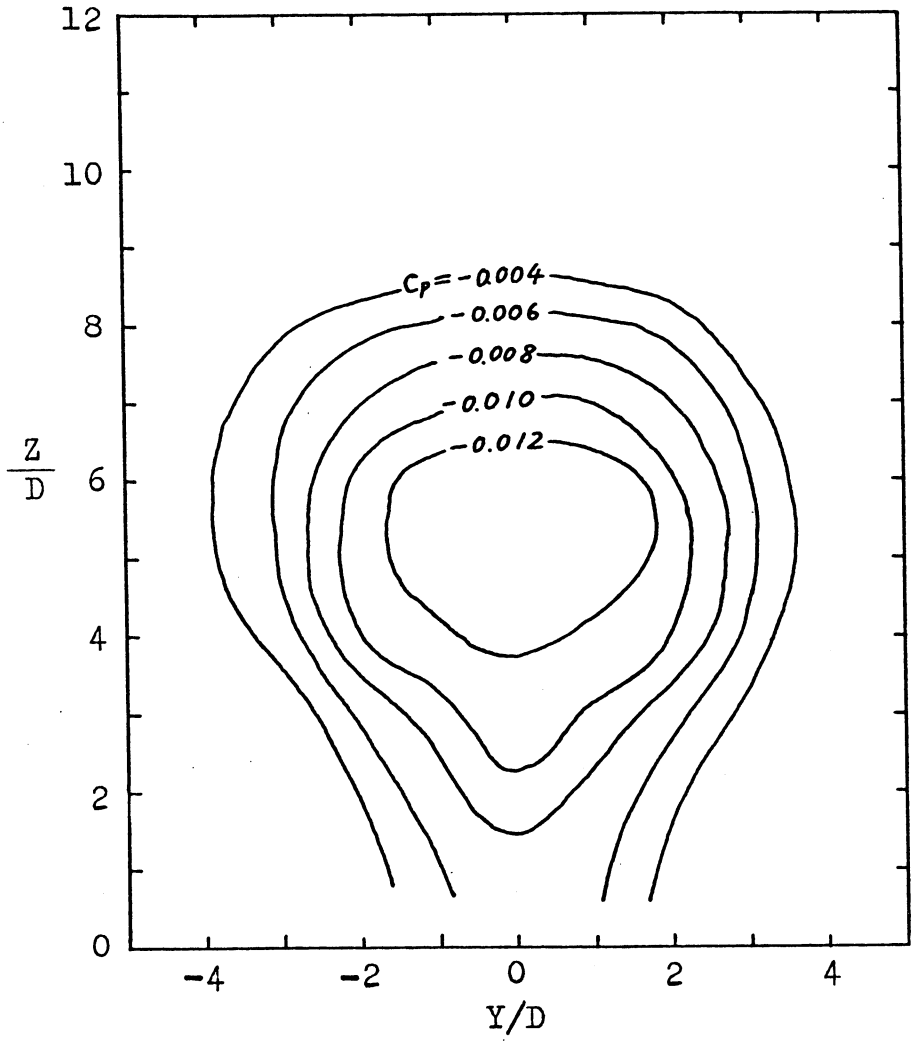

Figure 33. Static Pressure Distribution

R= 4, ξ/D= 20

$\frac{X}{D}$=16.5

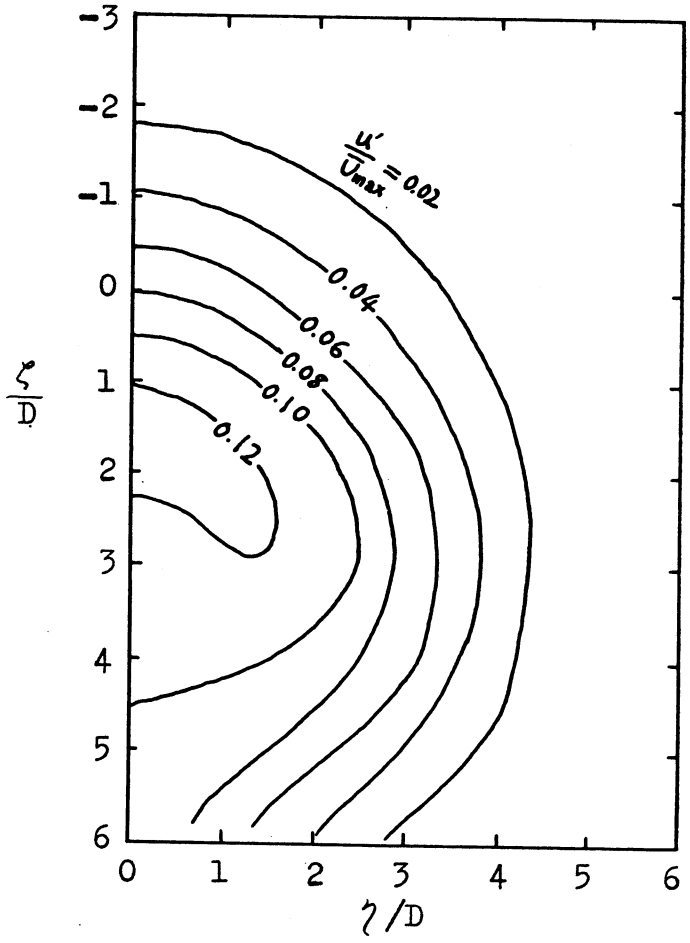

Figure 34. Distribution of Turbulence Intensity

R= 8, ξ/D= 23

$\frac{X}{D}$ = 14.25

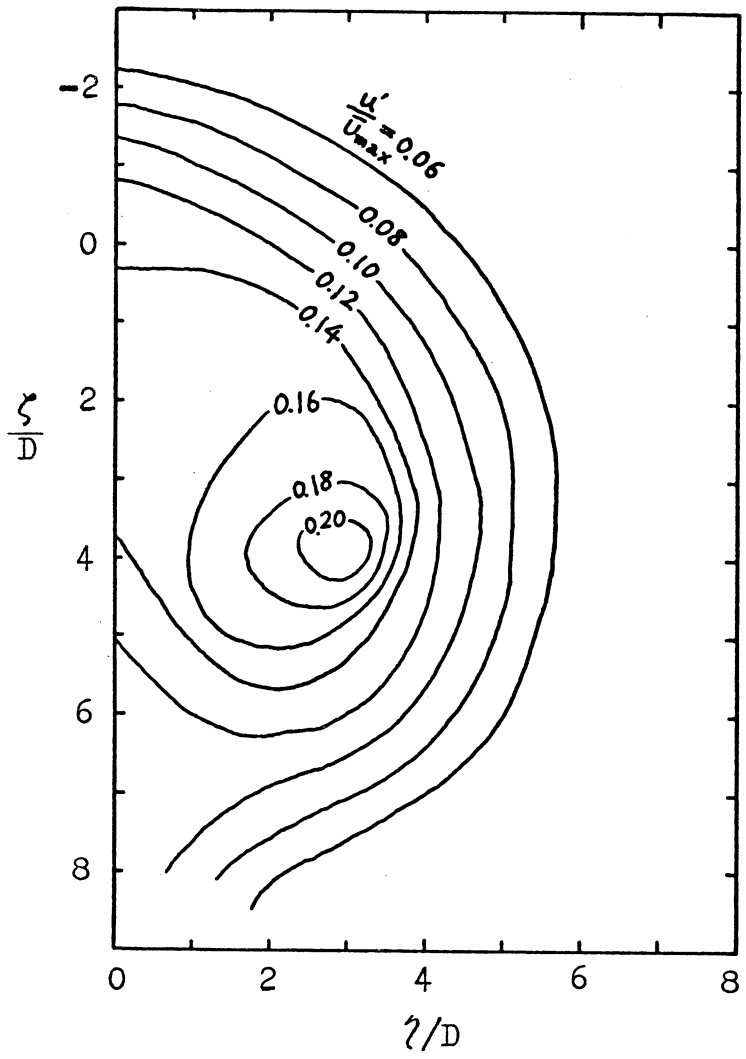

Figure 35. Distribution of Turbulence Intensity

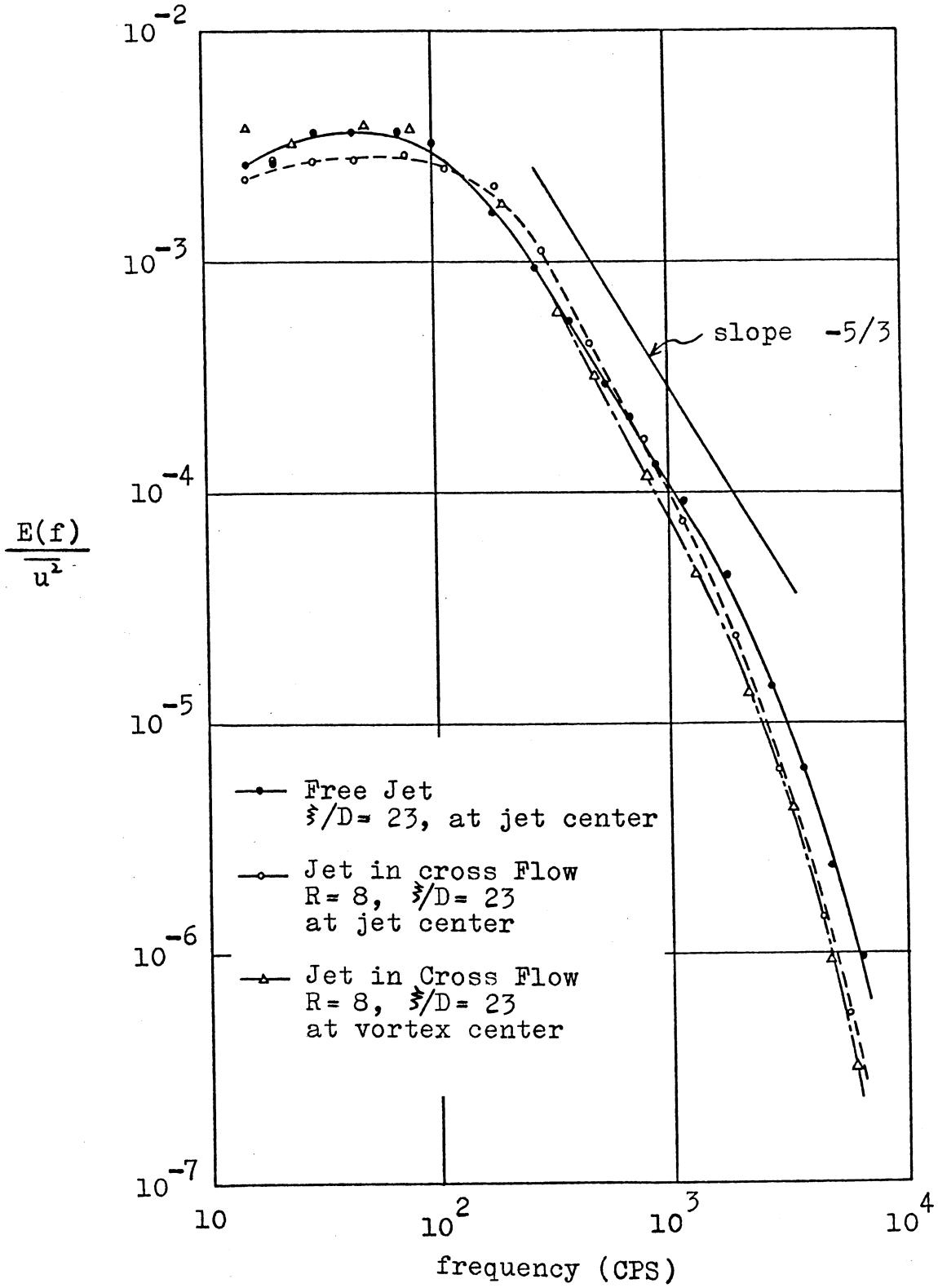

Figure 36. Energy Spectra of Turbulence in Jets

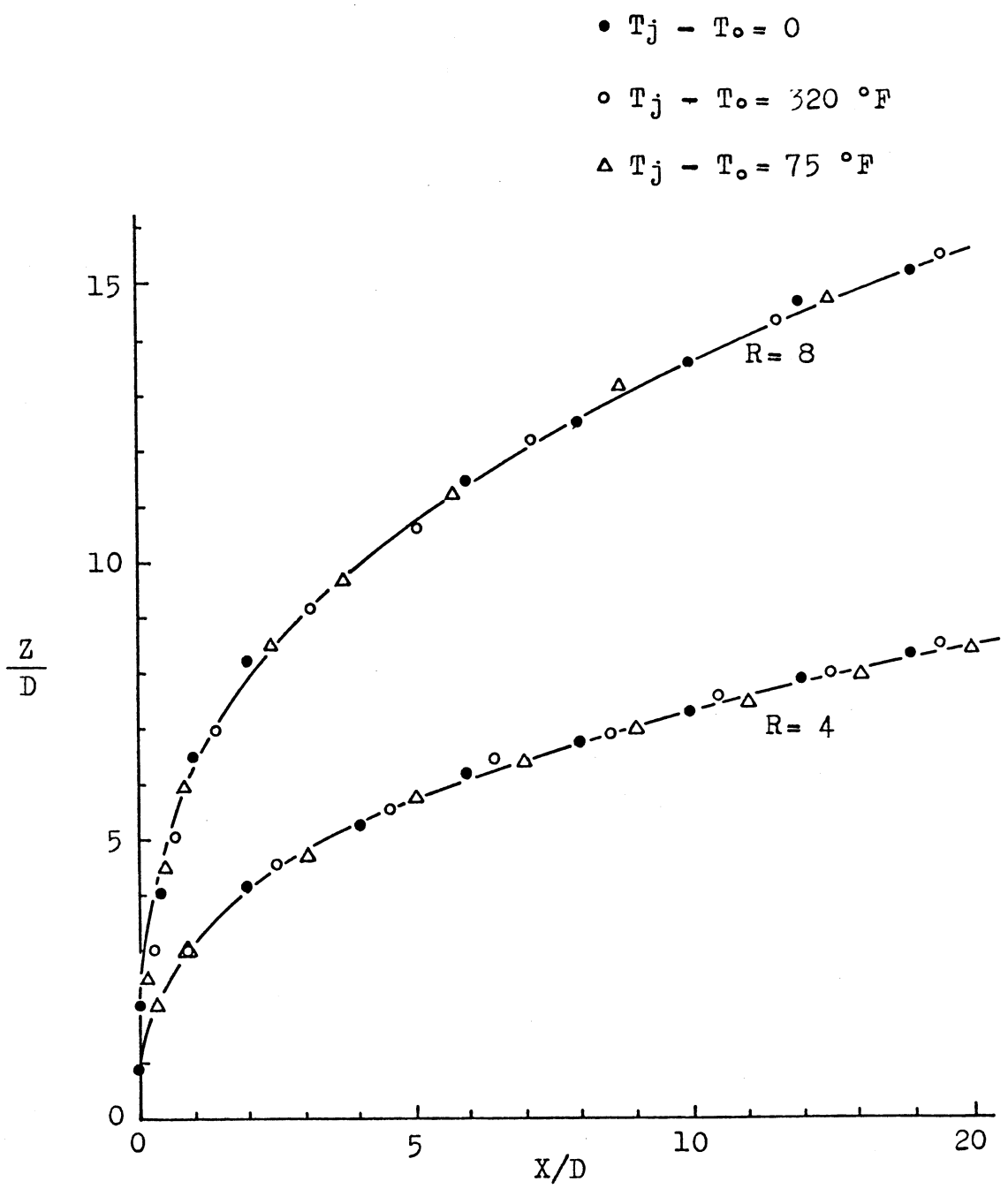

Figure 37. Centerline Location of Heated and Unheated Jets

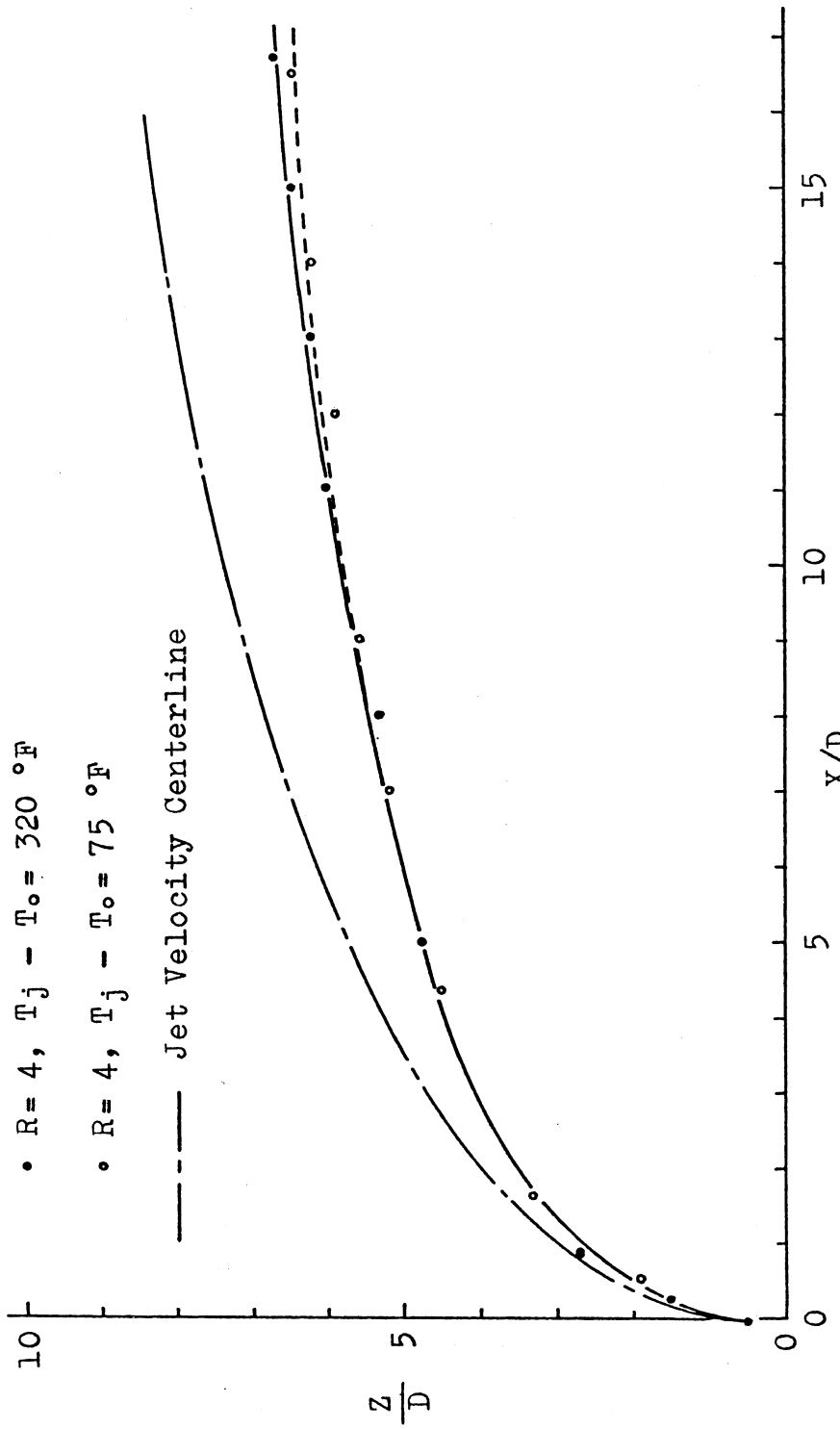

Figure 38. Location of Temperature Centerline (R= 4)

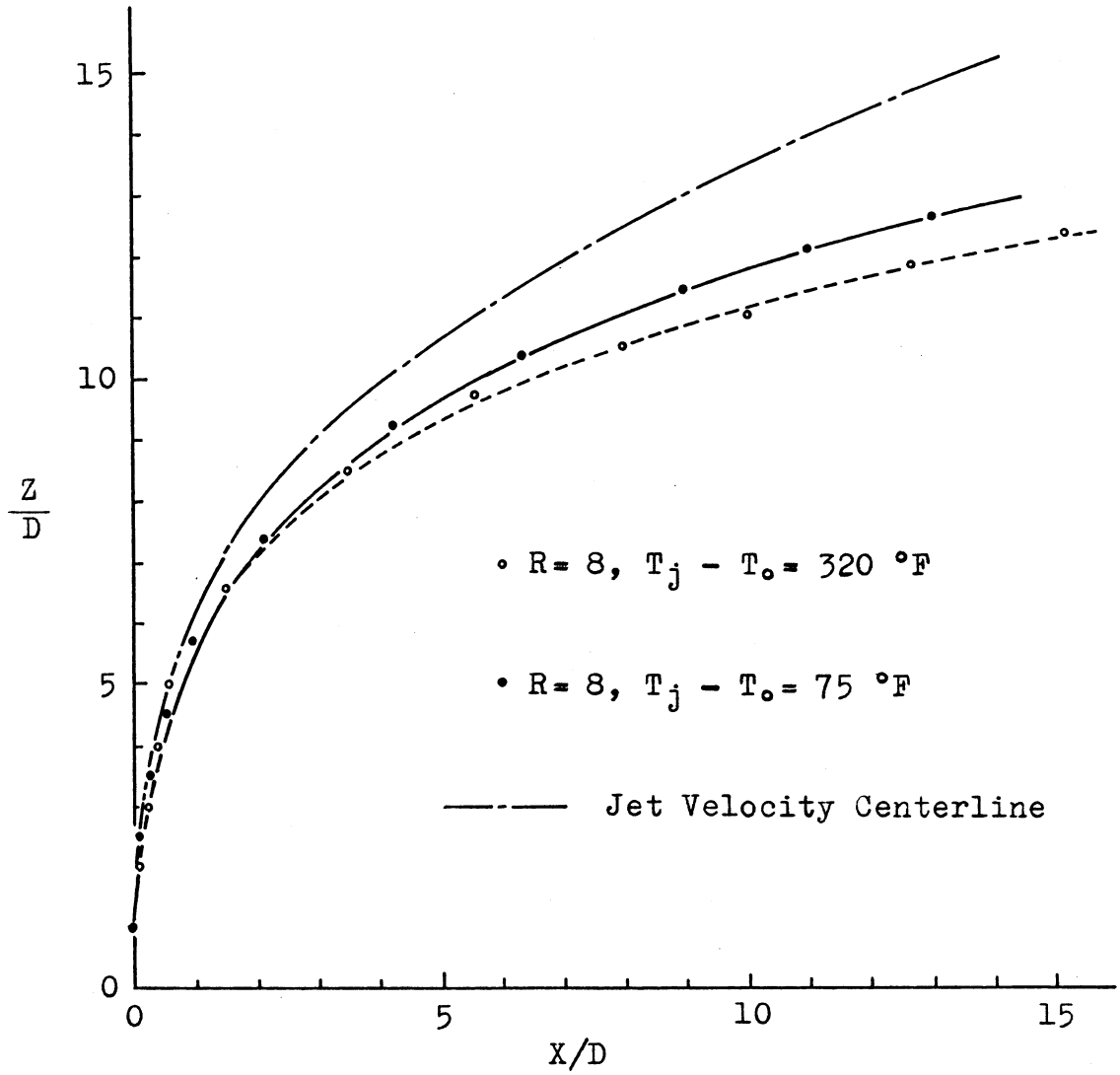

Figure 39. Location of Temperature Centerline (R= 8)

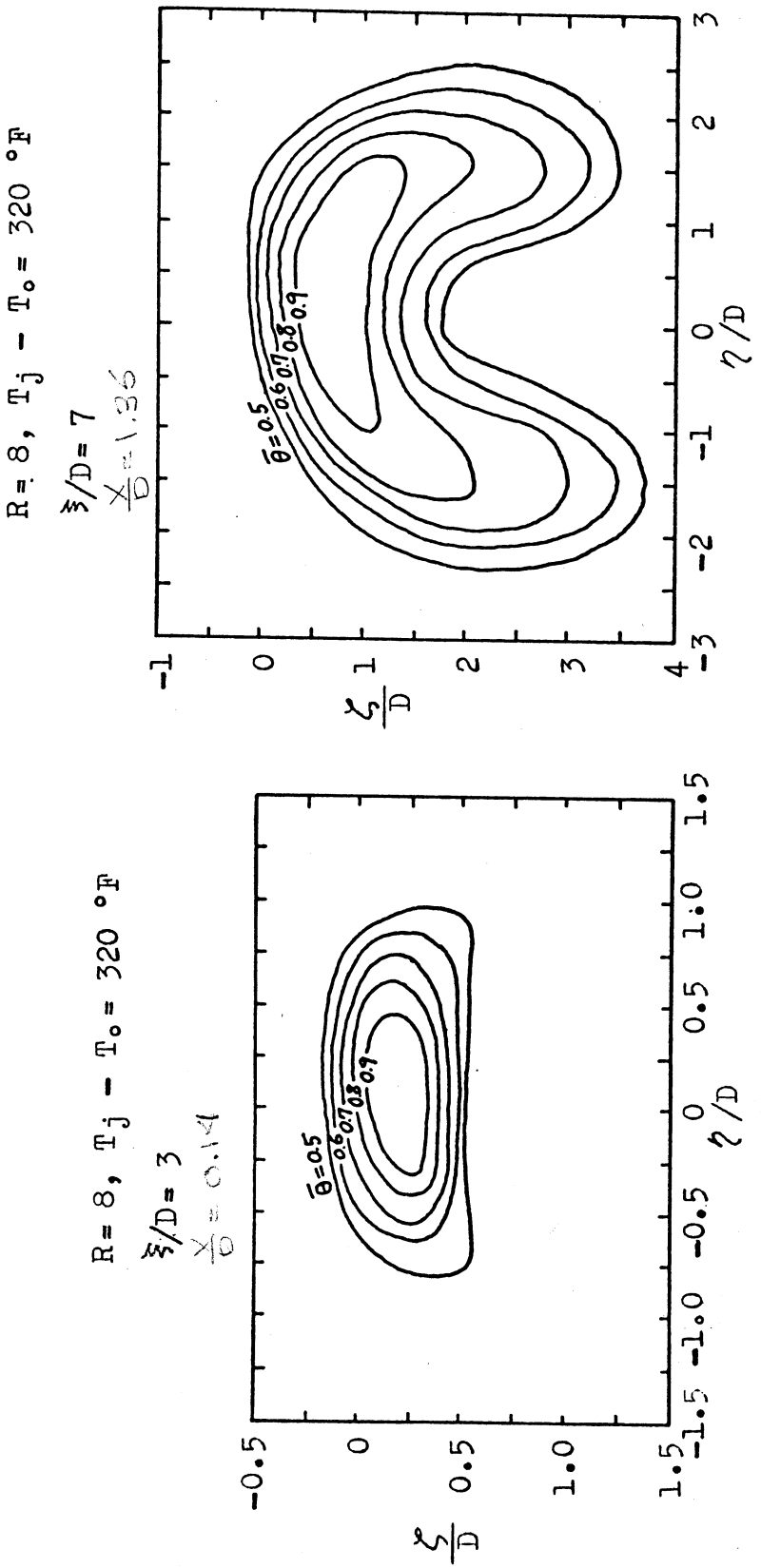

Figure 40. Contours of Constant Temperature

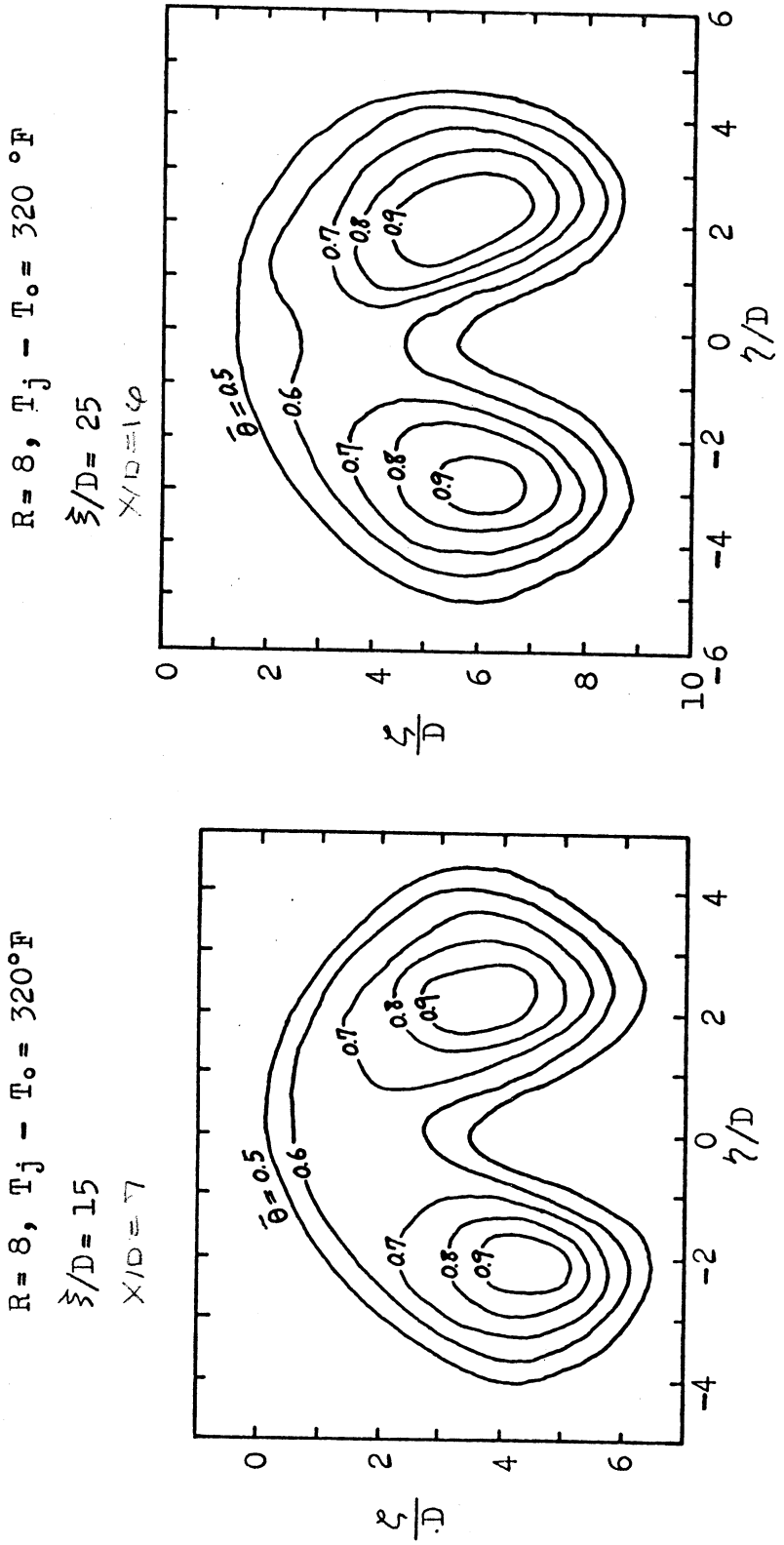

Figure 41. Contours of Constant Temperature

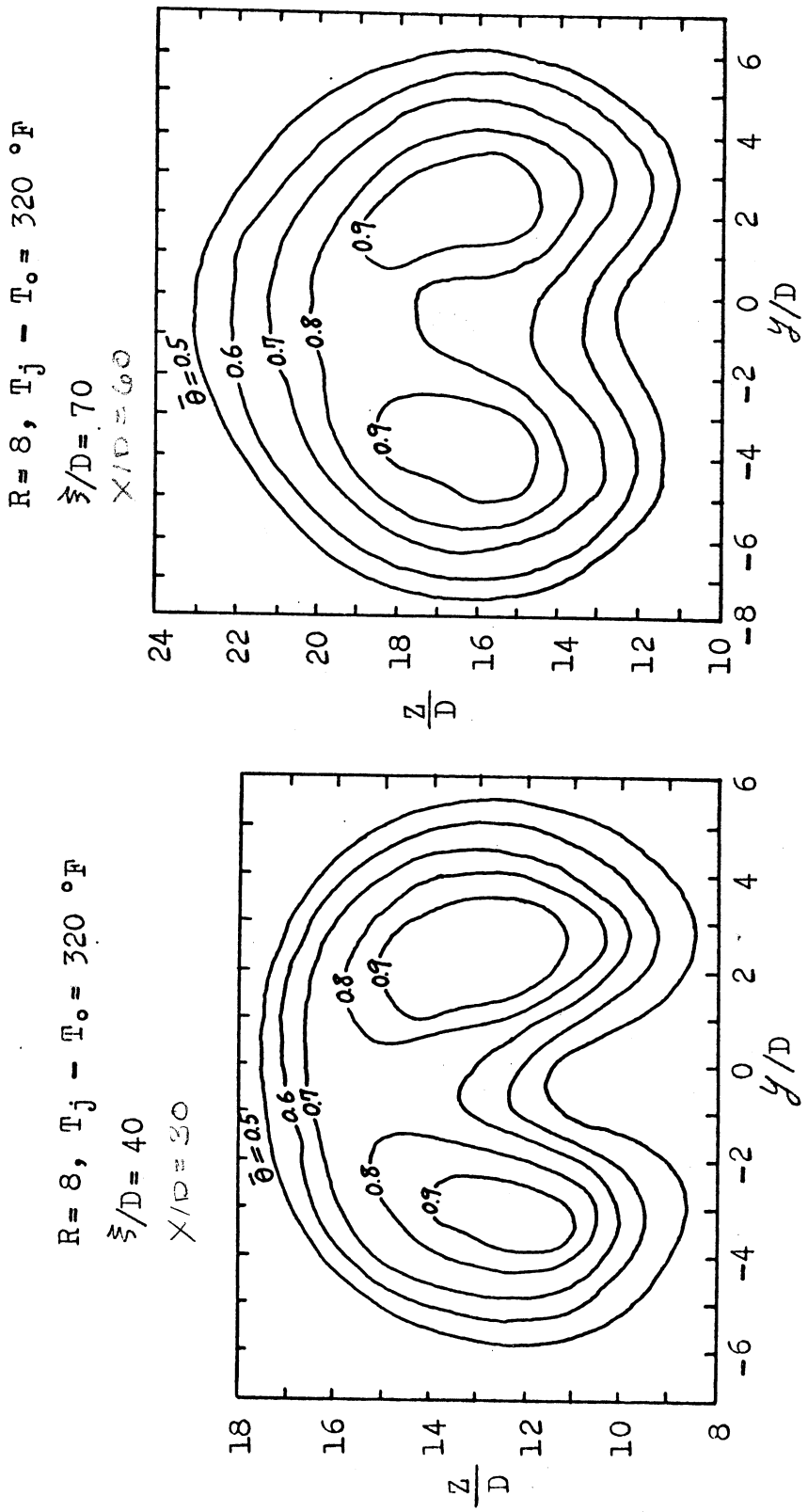

Figure 42. Contours of Constant Temperature

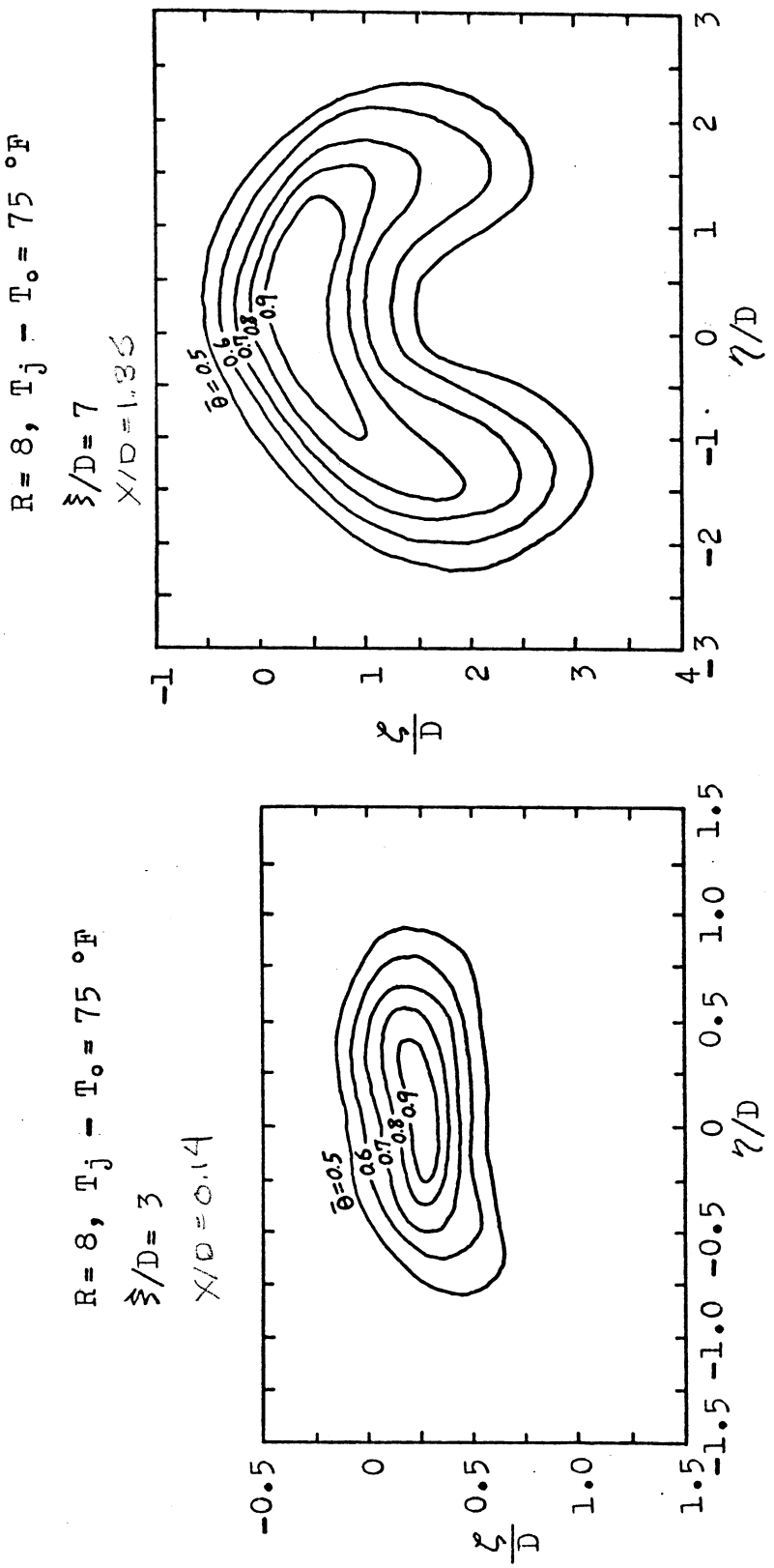

Figure 43. Contours of Constant Temperature

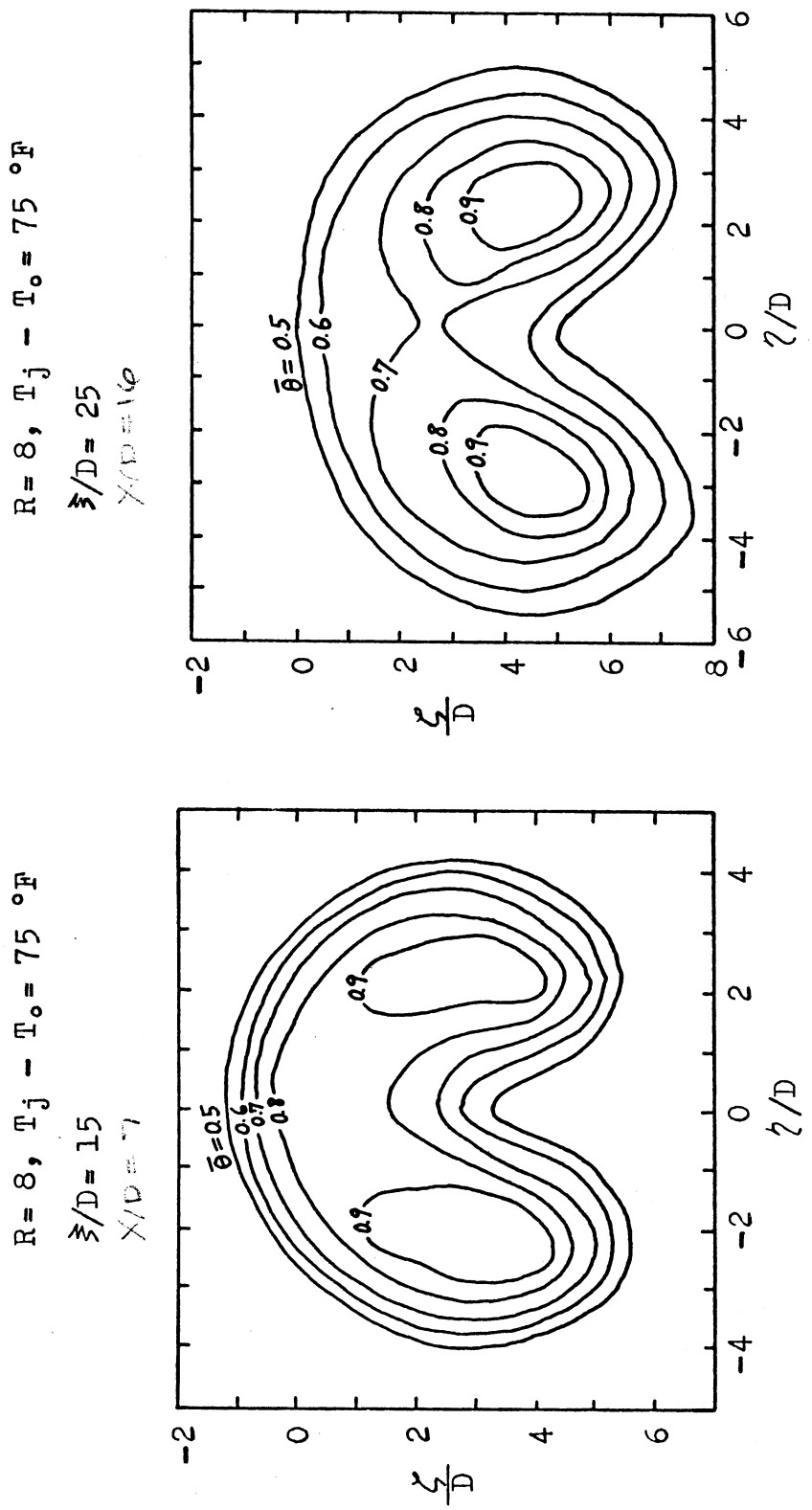

Figure 44. Contours of Constant Temperature

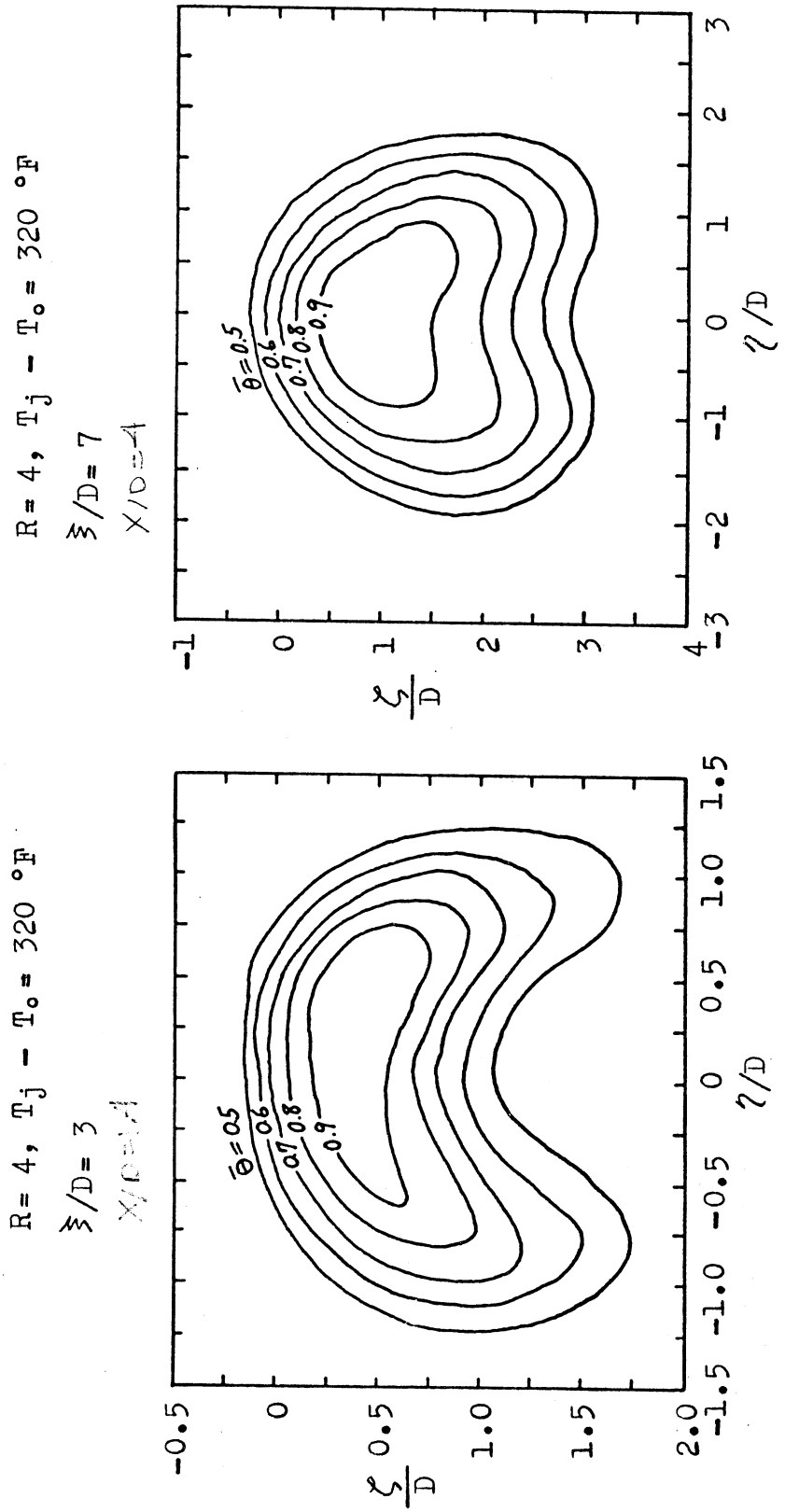

Figure 45. Contours of Constant Temperature

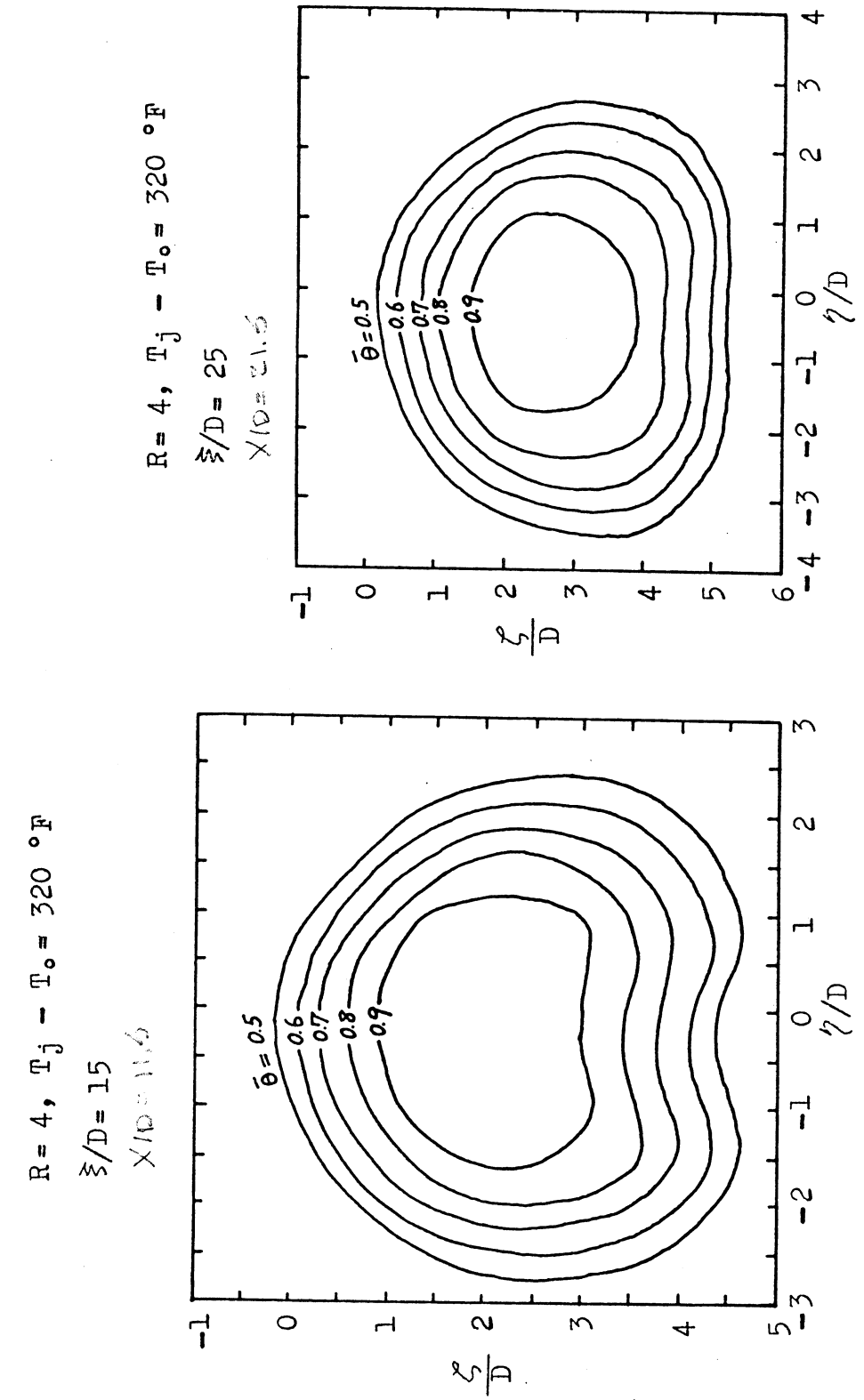

Figure 46. Contours of Constant Temperature

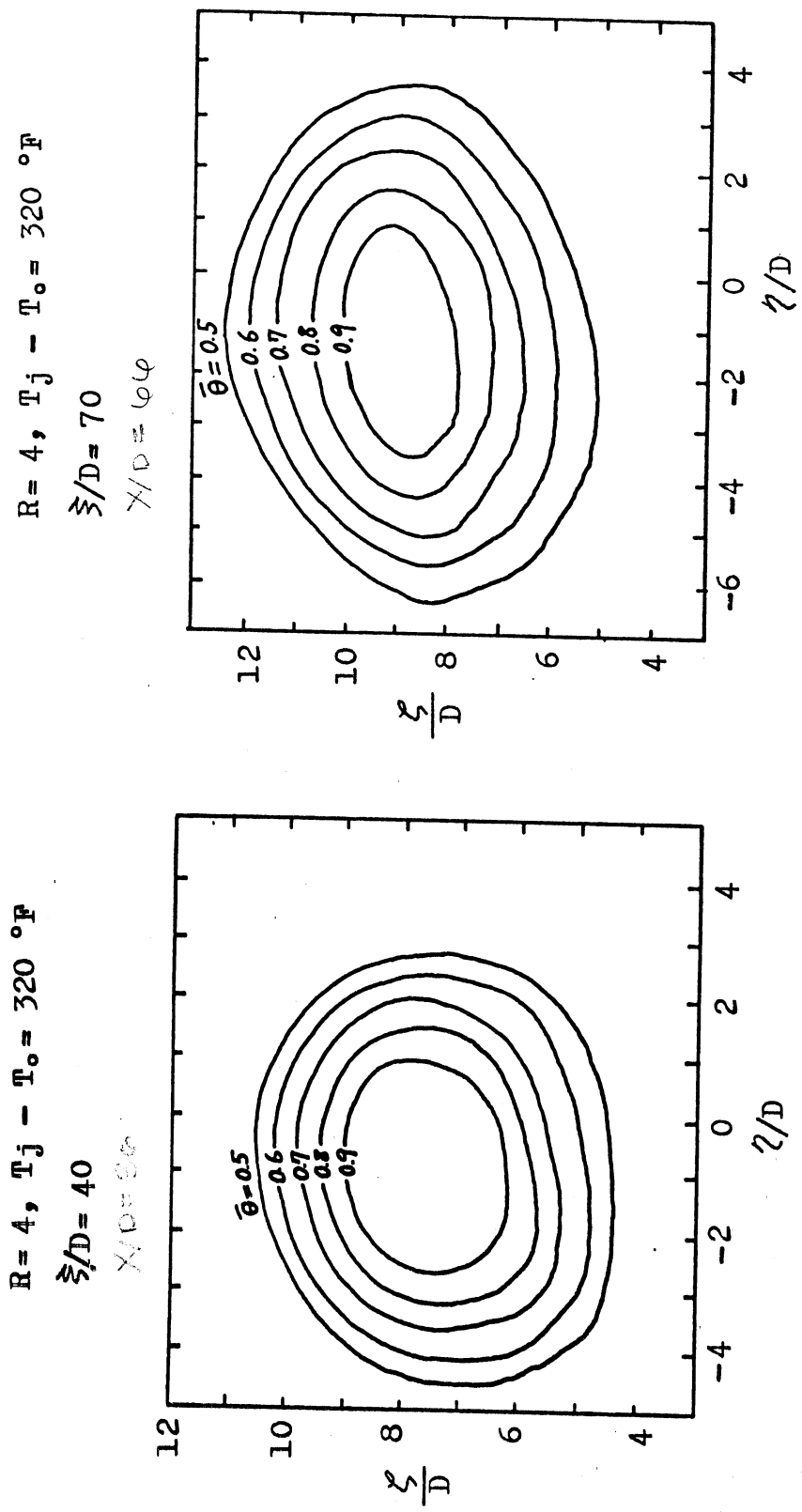

Figure 47. Contours of Constant Temperature

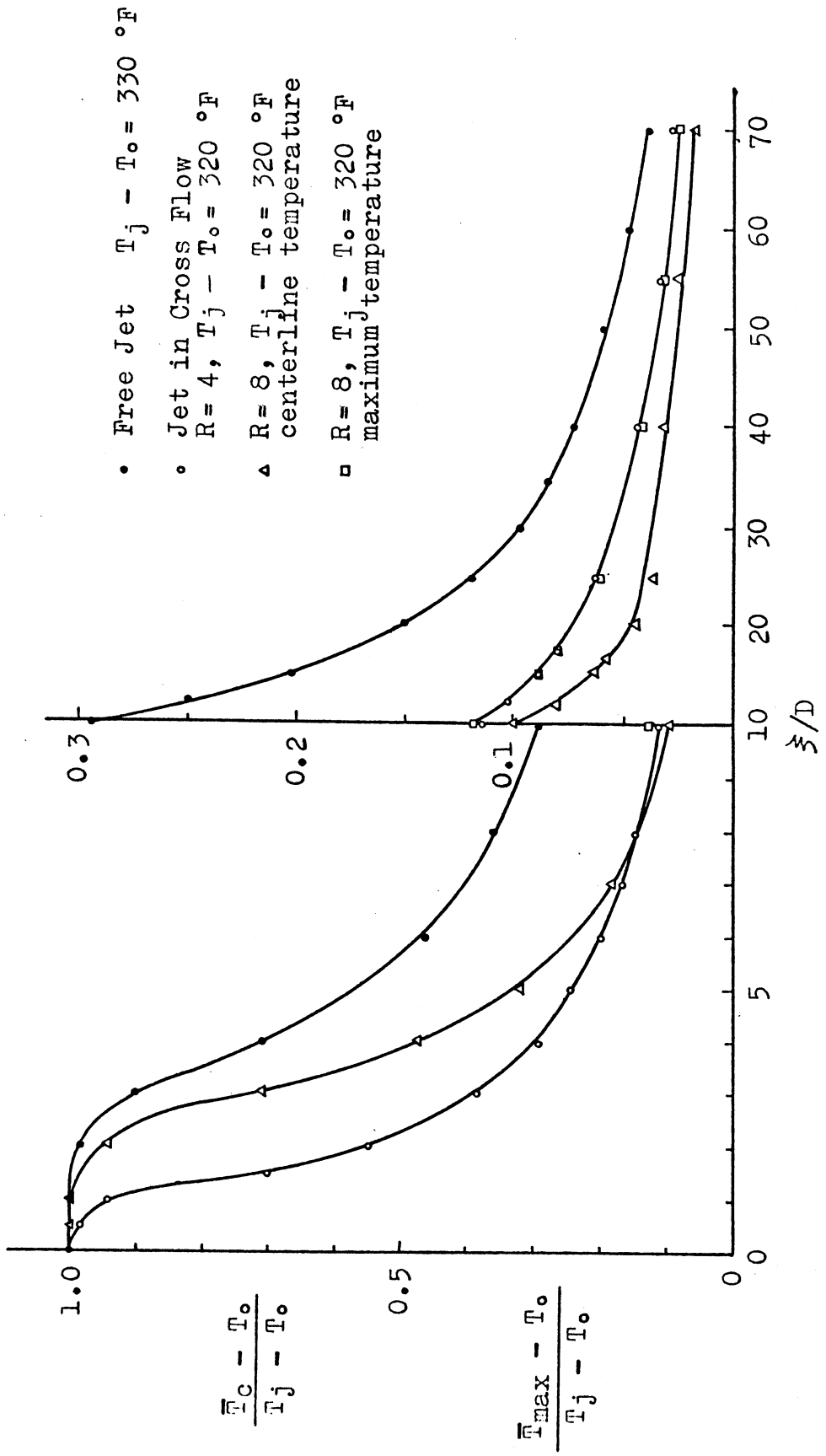

Figure 48. Distribution of Maximum and Centerline Temperature

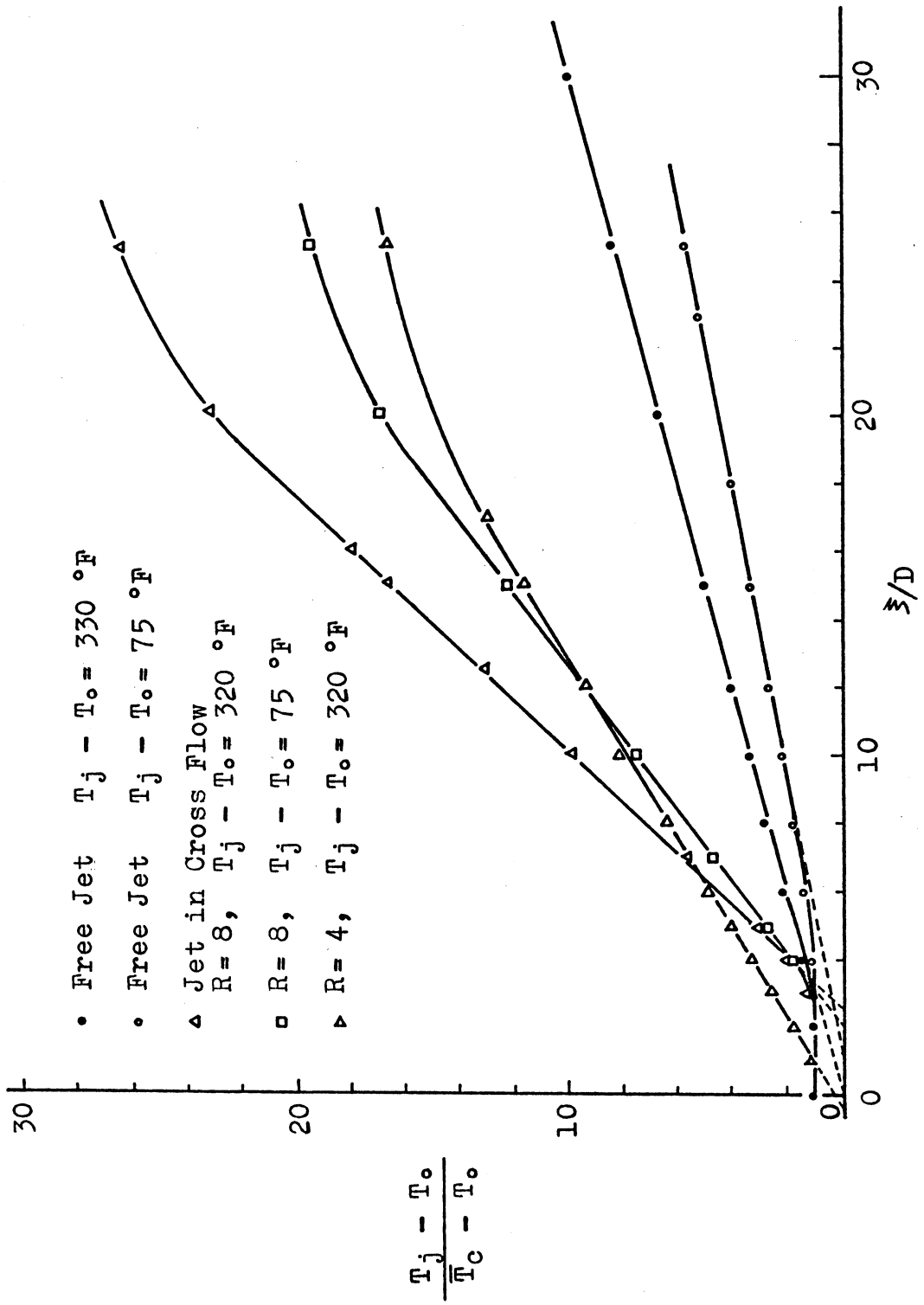

Figure 49. Temperature Distribution along Temperature Centerline

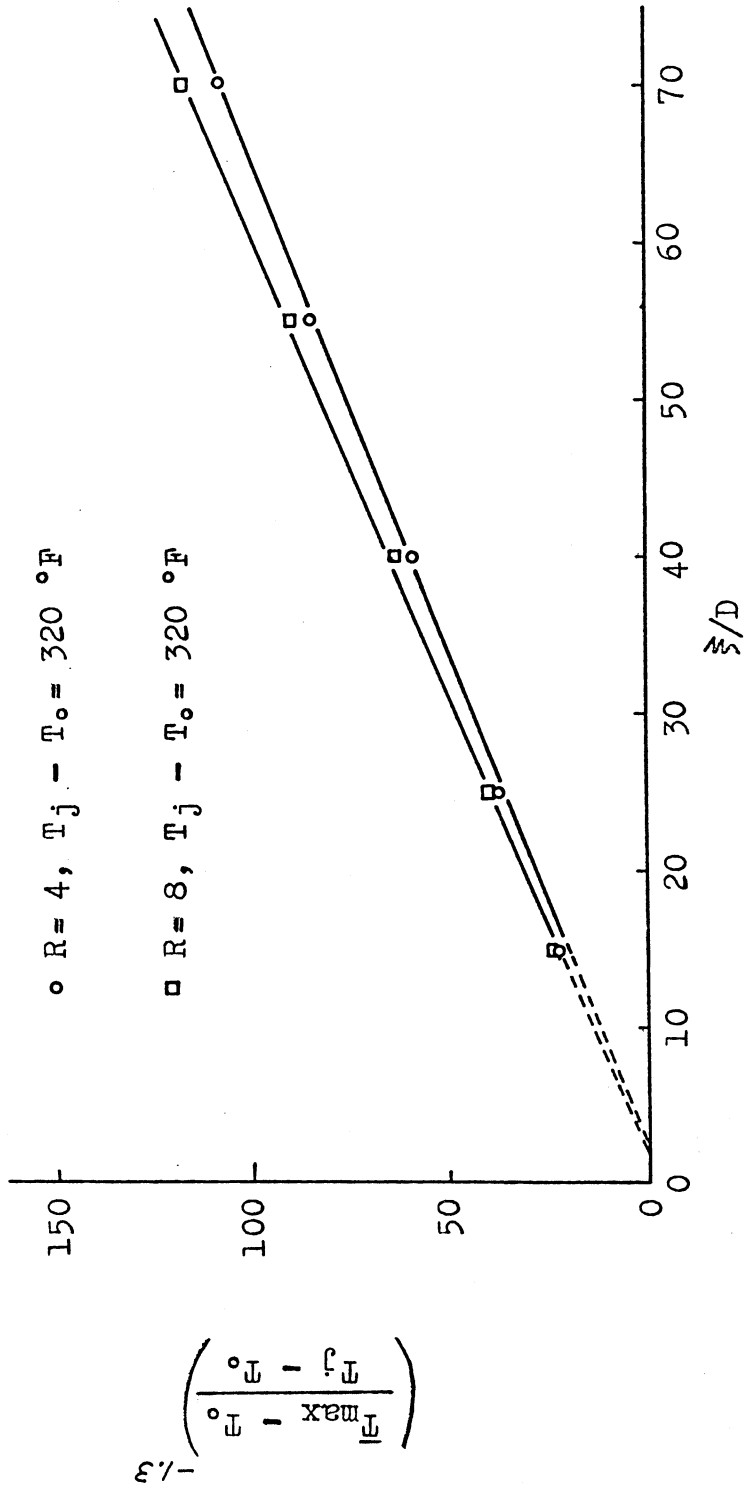

Figure 50. Temperature Distribution in Far Downstream Region

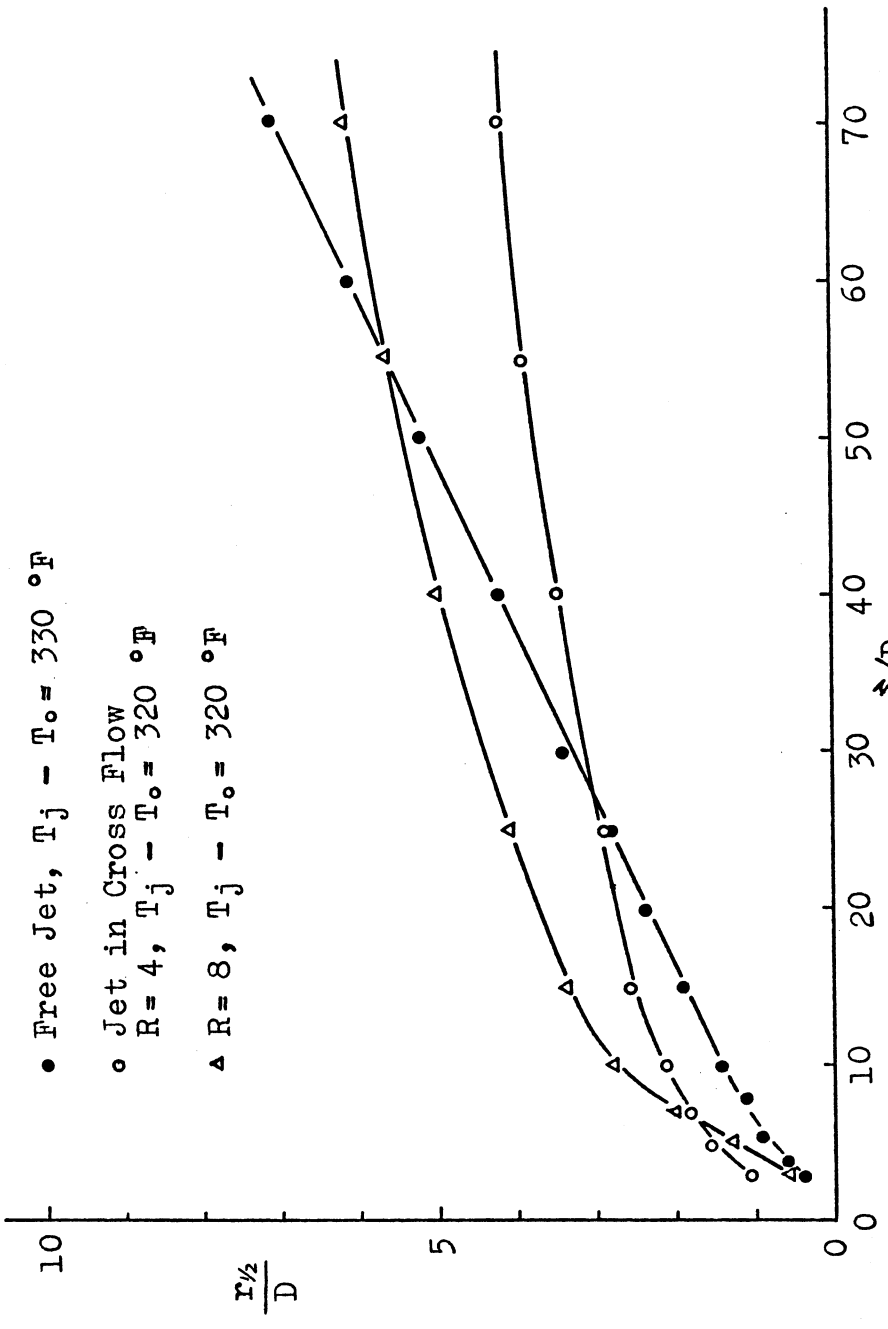

Figure 51. Diffusion of Temperature in Jets

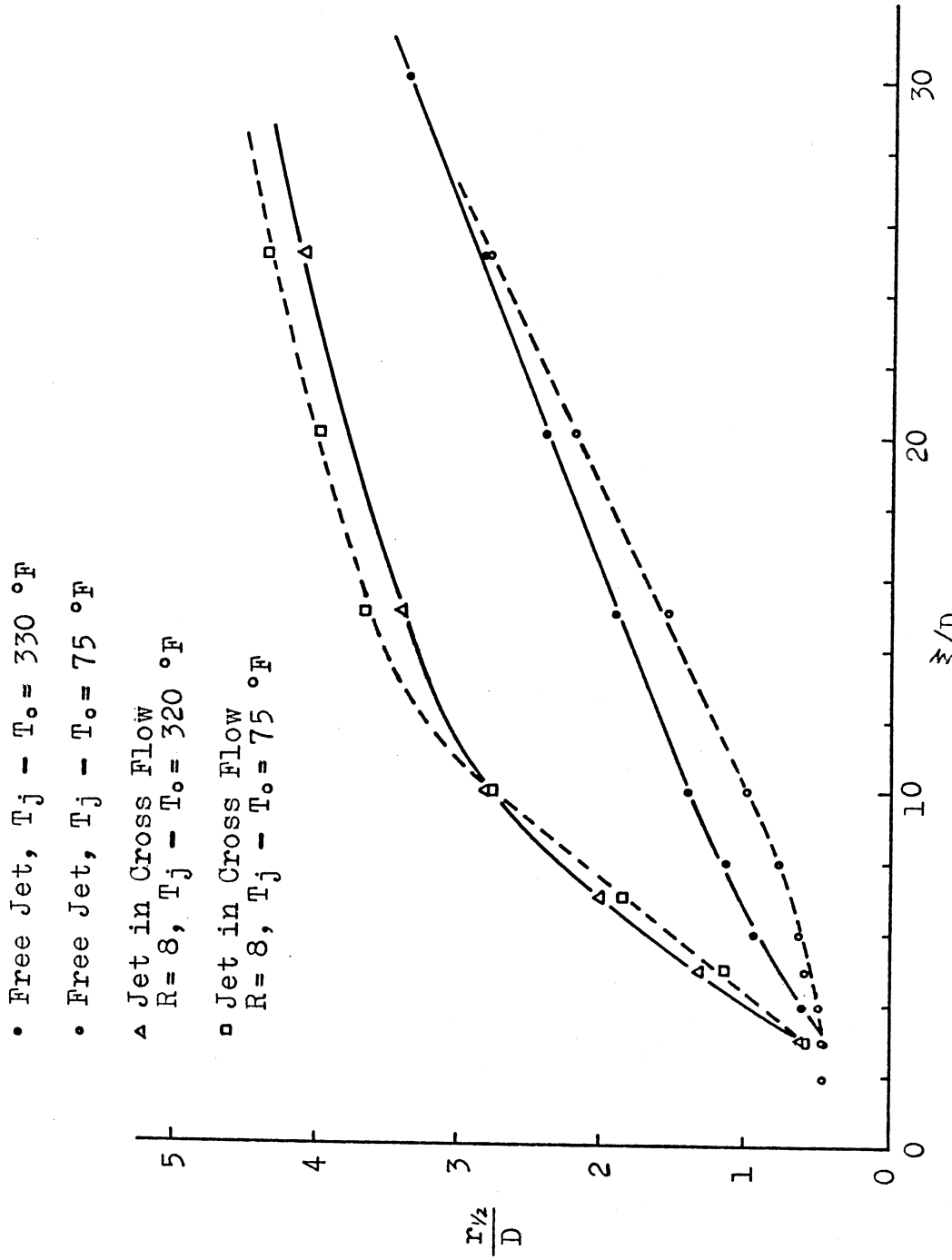

Figure 52. Diffusion of Temperature in Jets

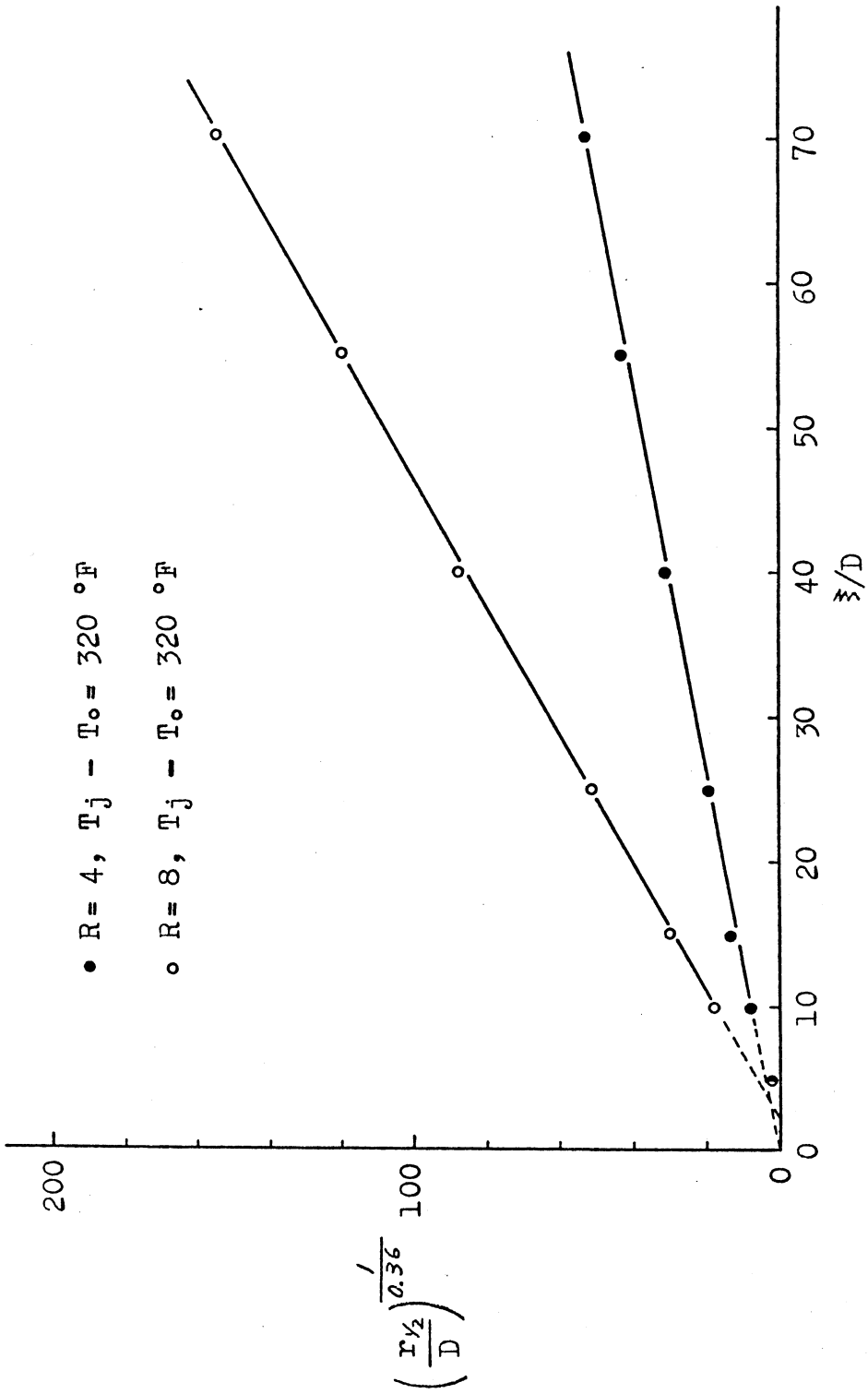

Figure 53. Diffusion of Temperature in Far Downstream Region

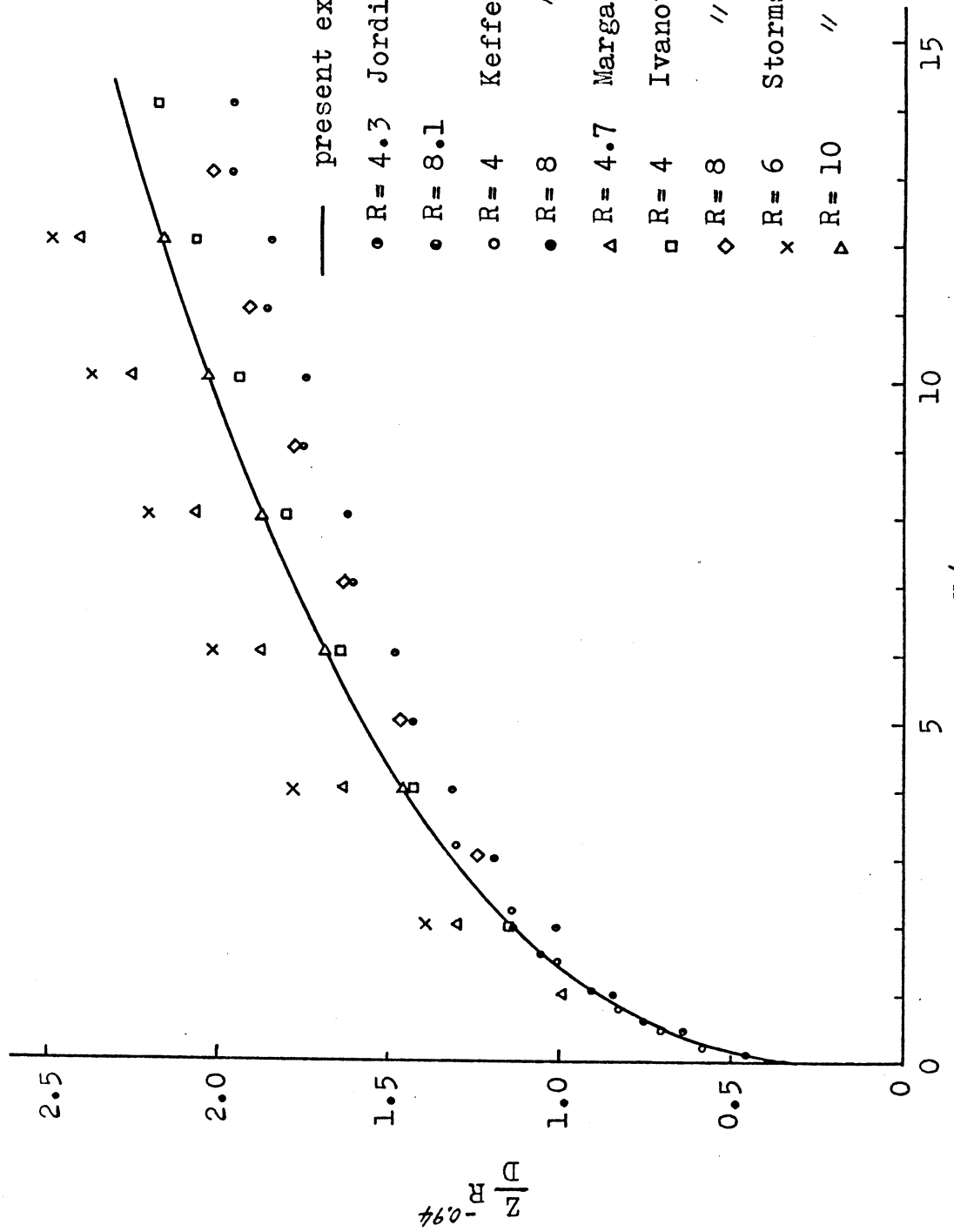

Figure 54. Comparison of Jet Centerline Location

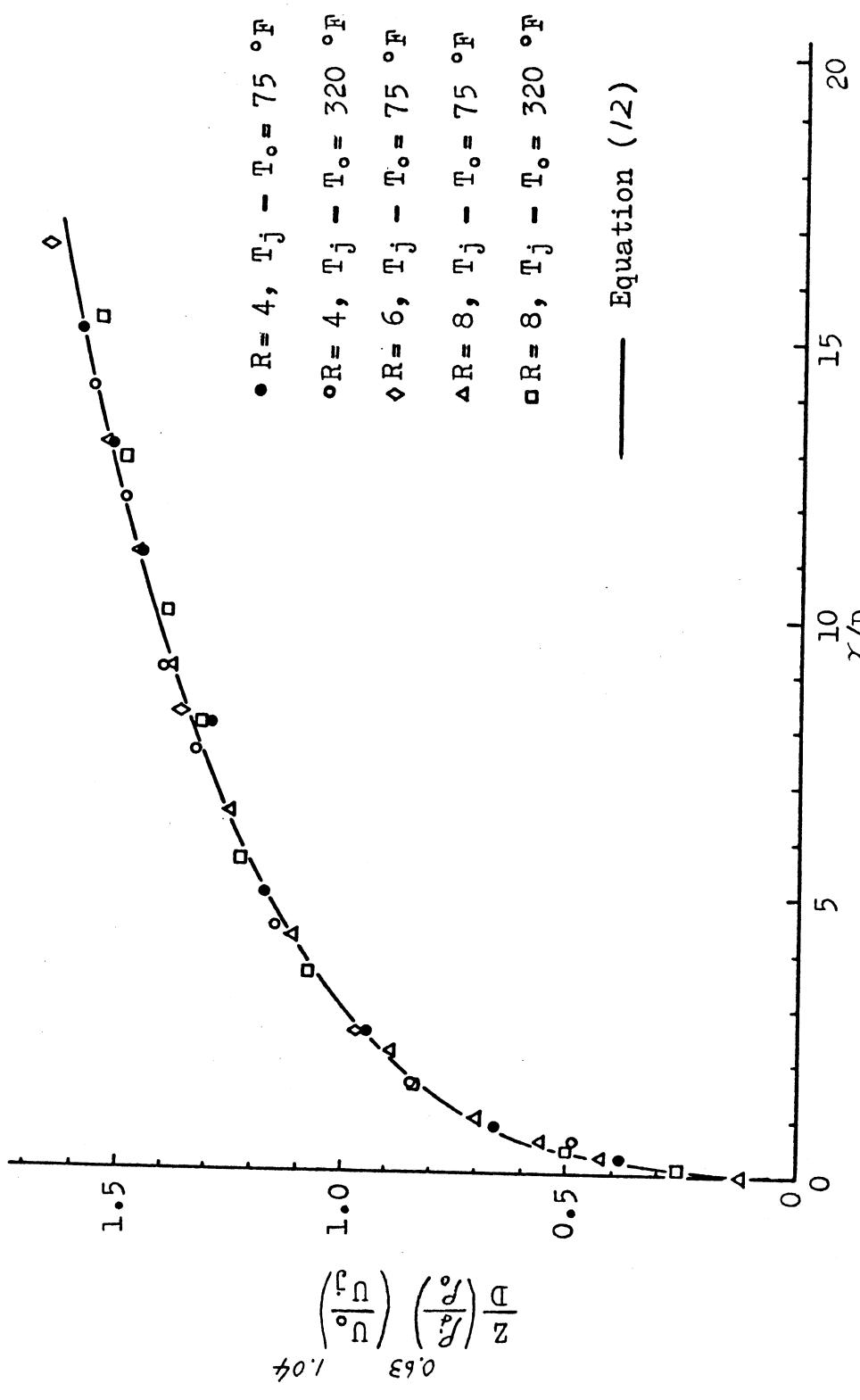

Figure 55. Correlation of Temperature Centerline Location

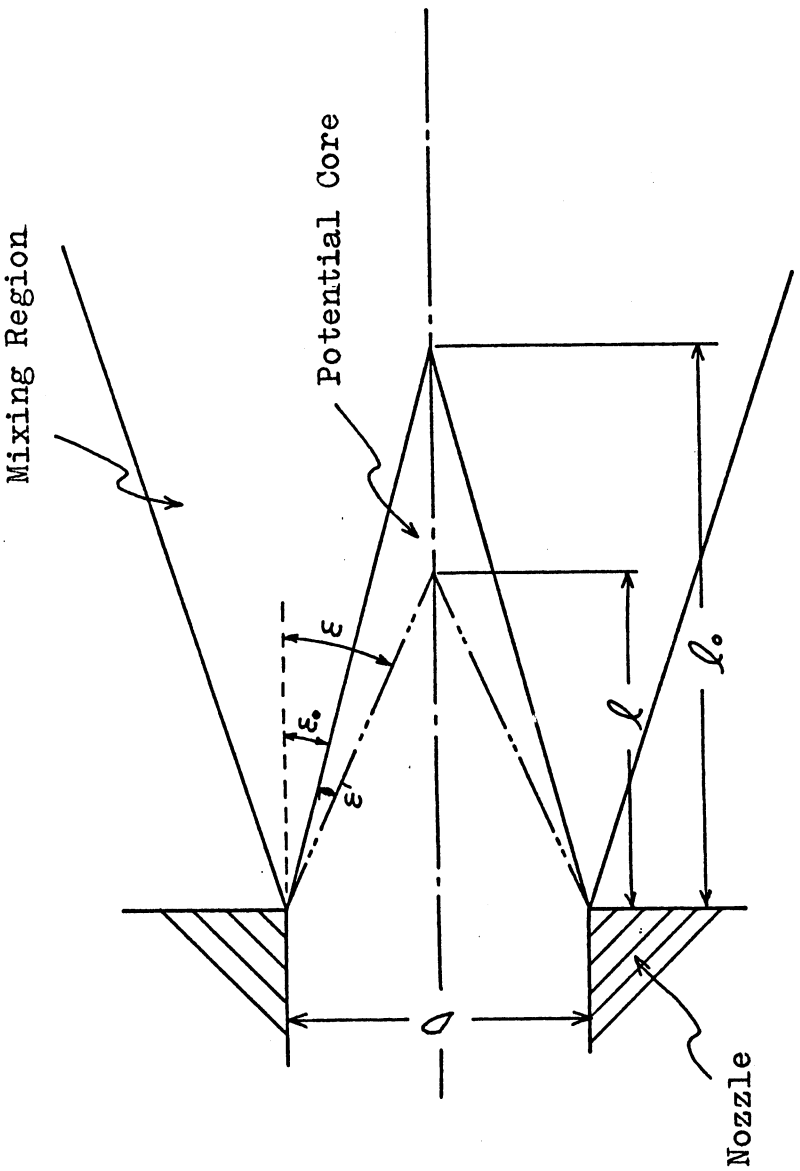

Figure 56. Potential Core Coordinates

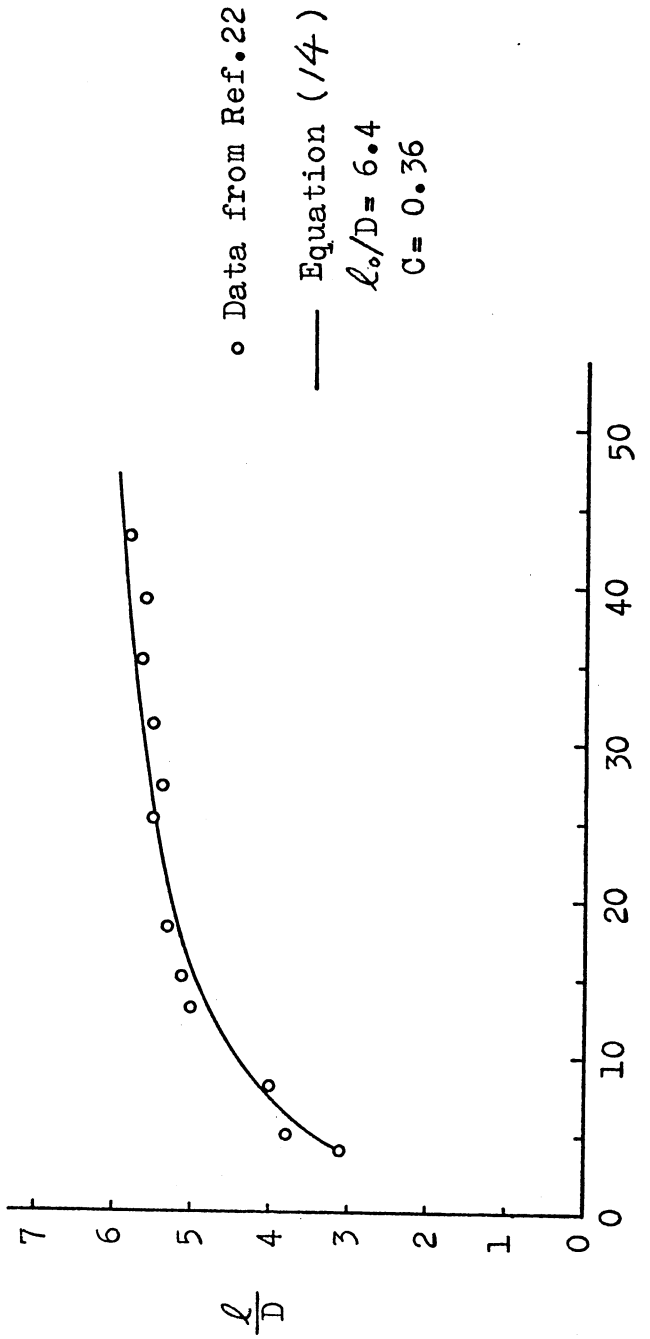

Figure 57. Potential Core Length of Jet in Cross Flow

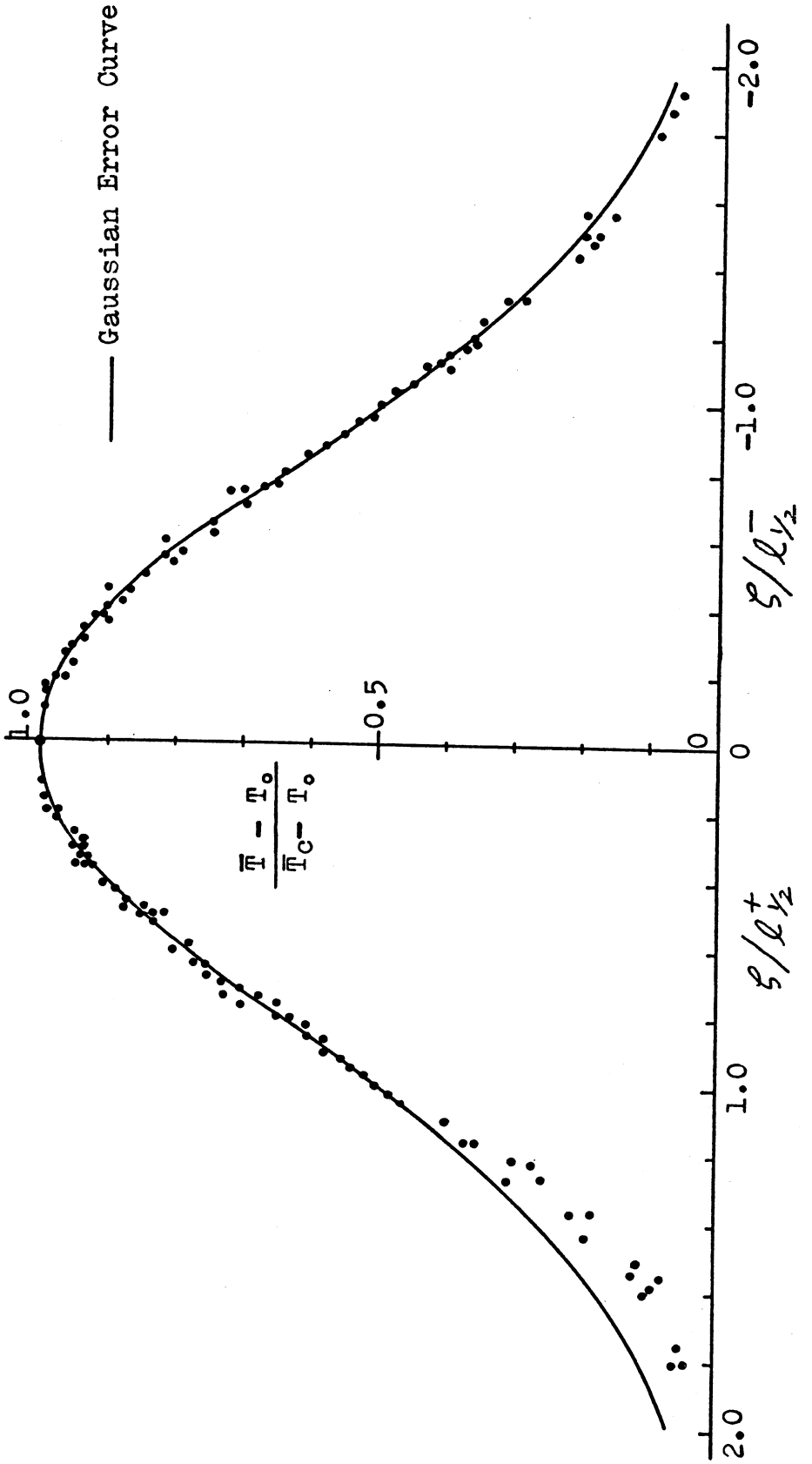

Figure 58. Temperature Distribution in the Plane of Symmetry

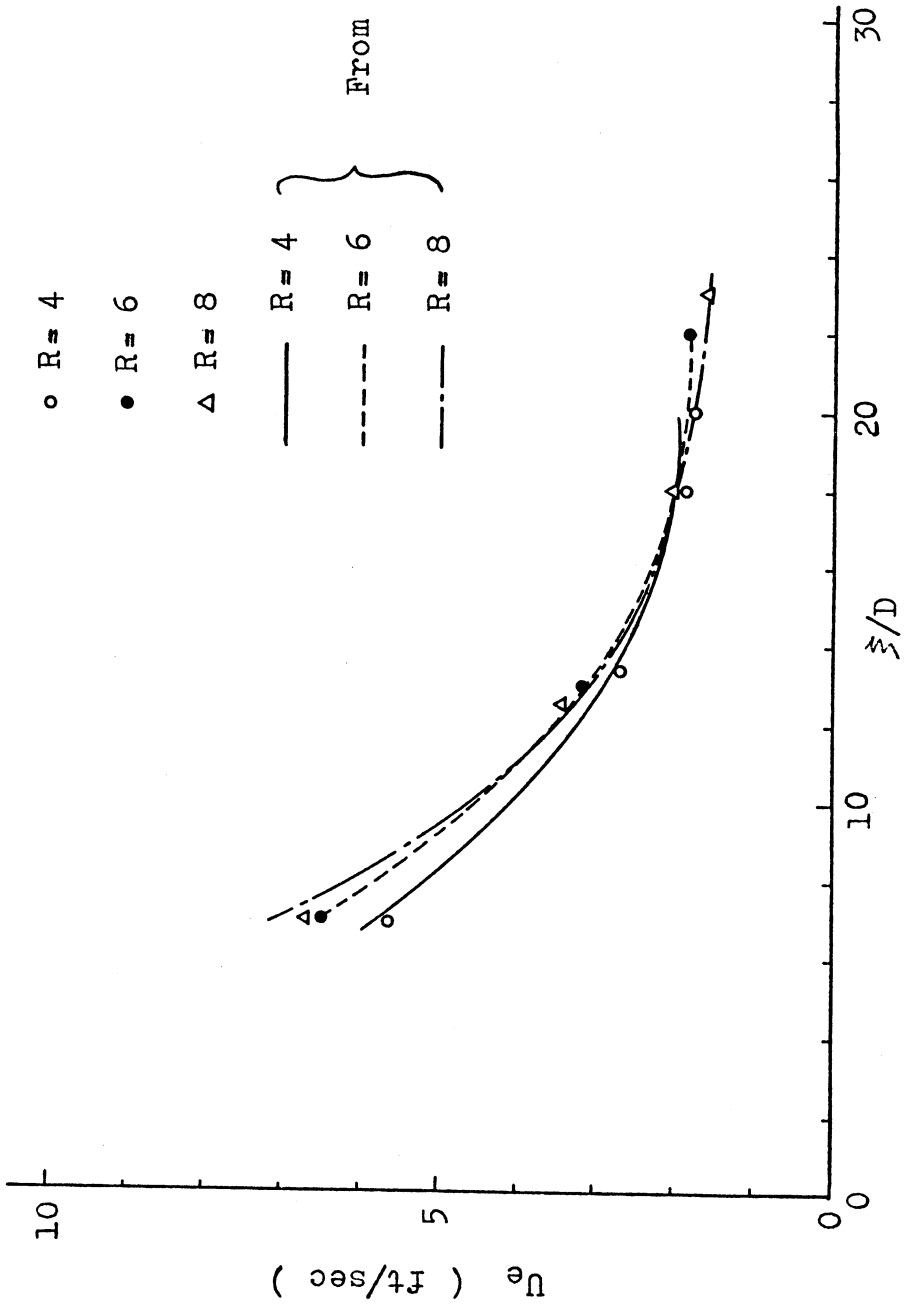

Figure 59. Distribution of Entrainment Velocity

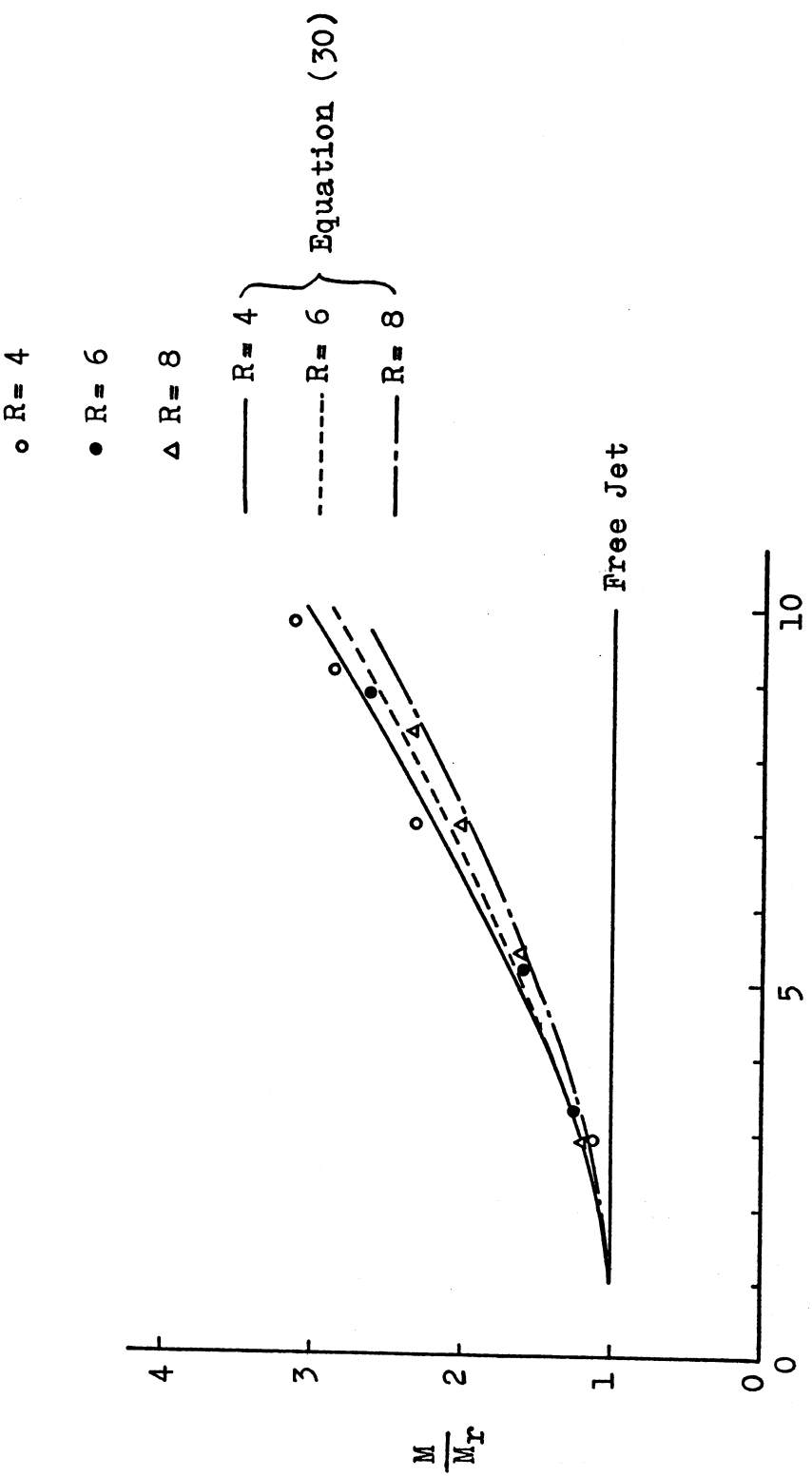

Figure 60. Mass - Momentum Flux Diagram

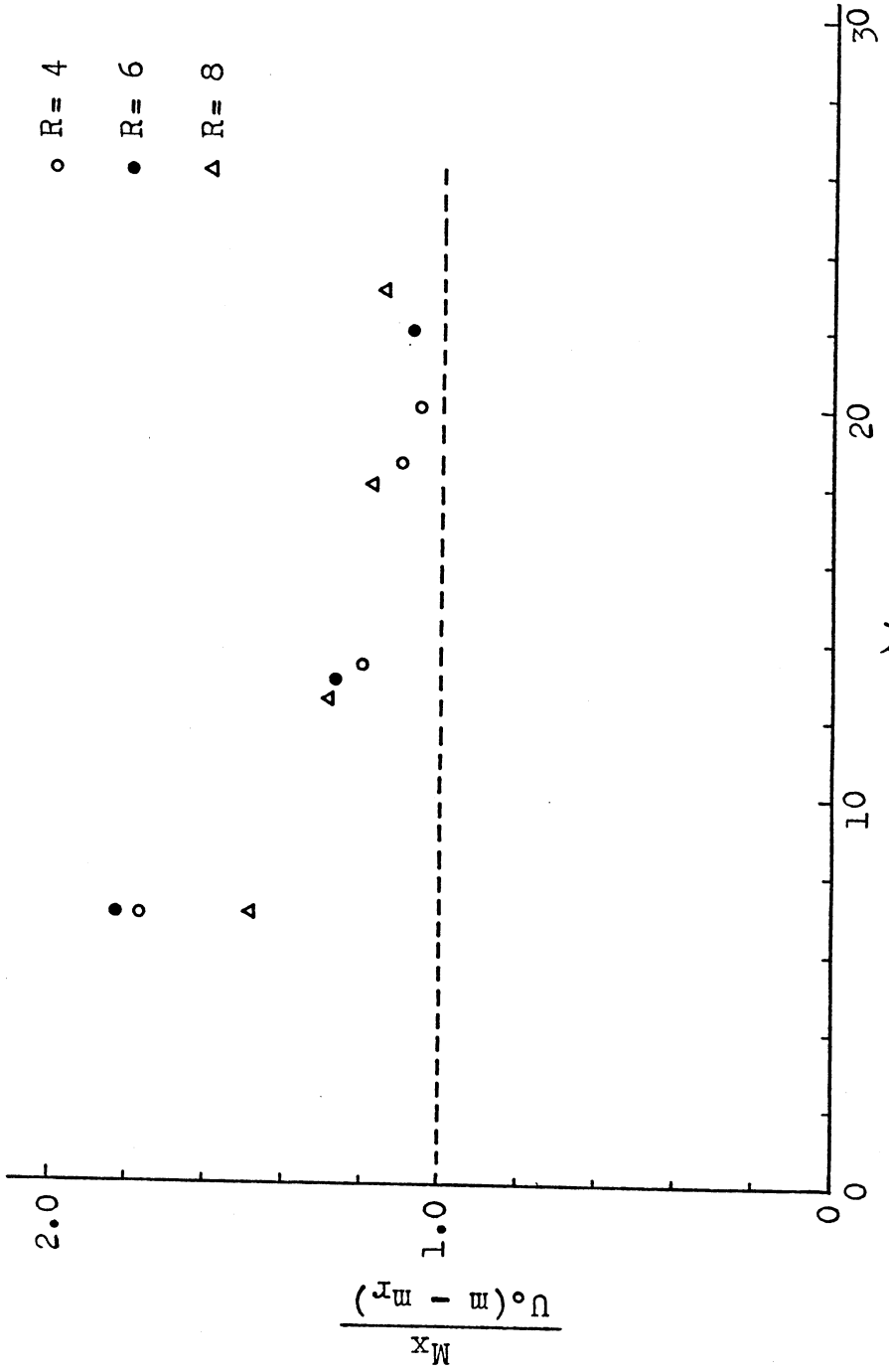

Figure 61. Mass and Momentum Flux in Cross Flow Direction

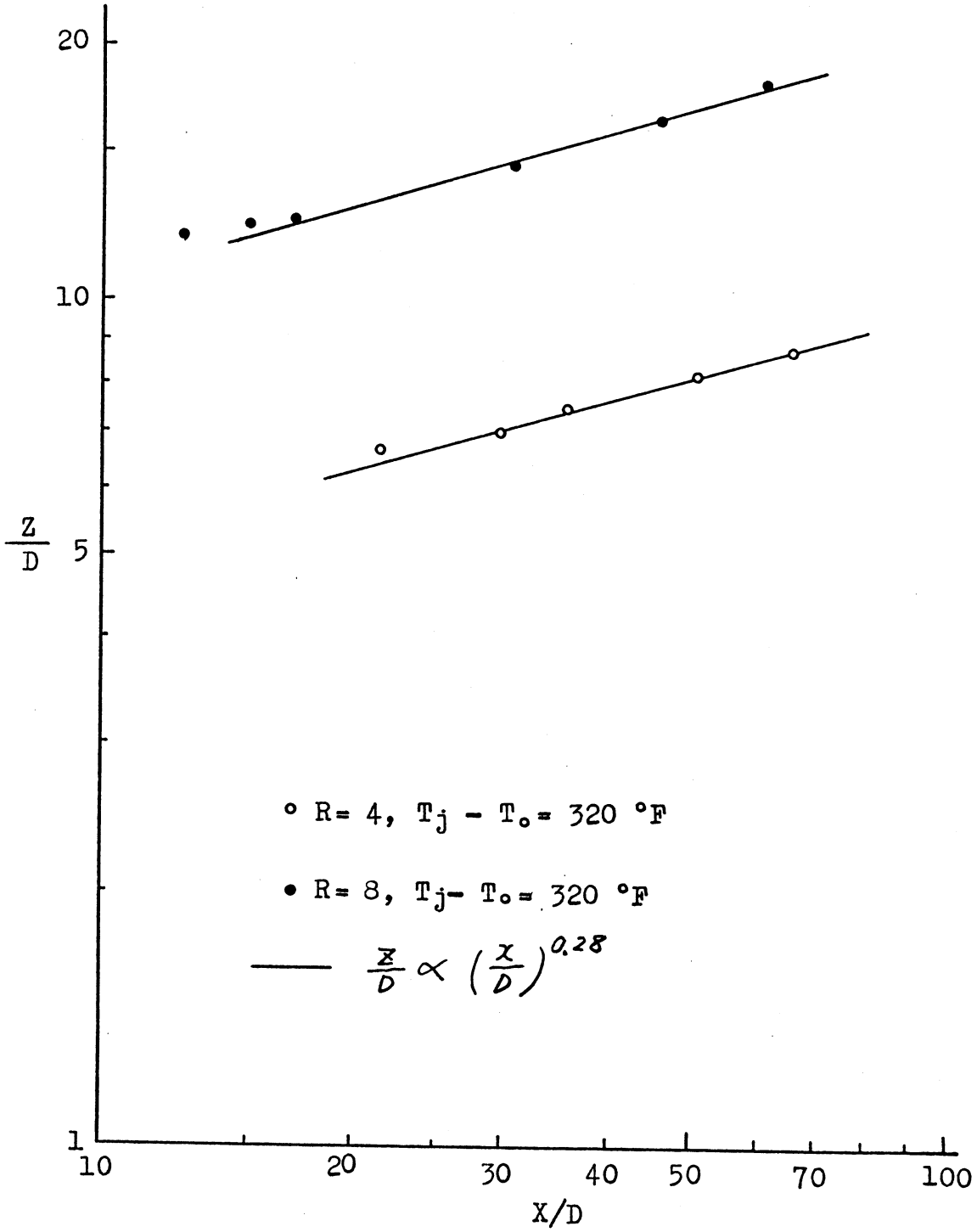

Figure 62. Temperature Centerline Location in Far Downstream Region

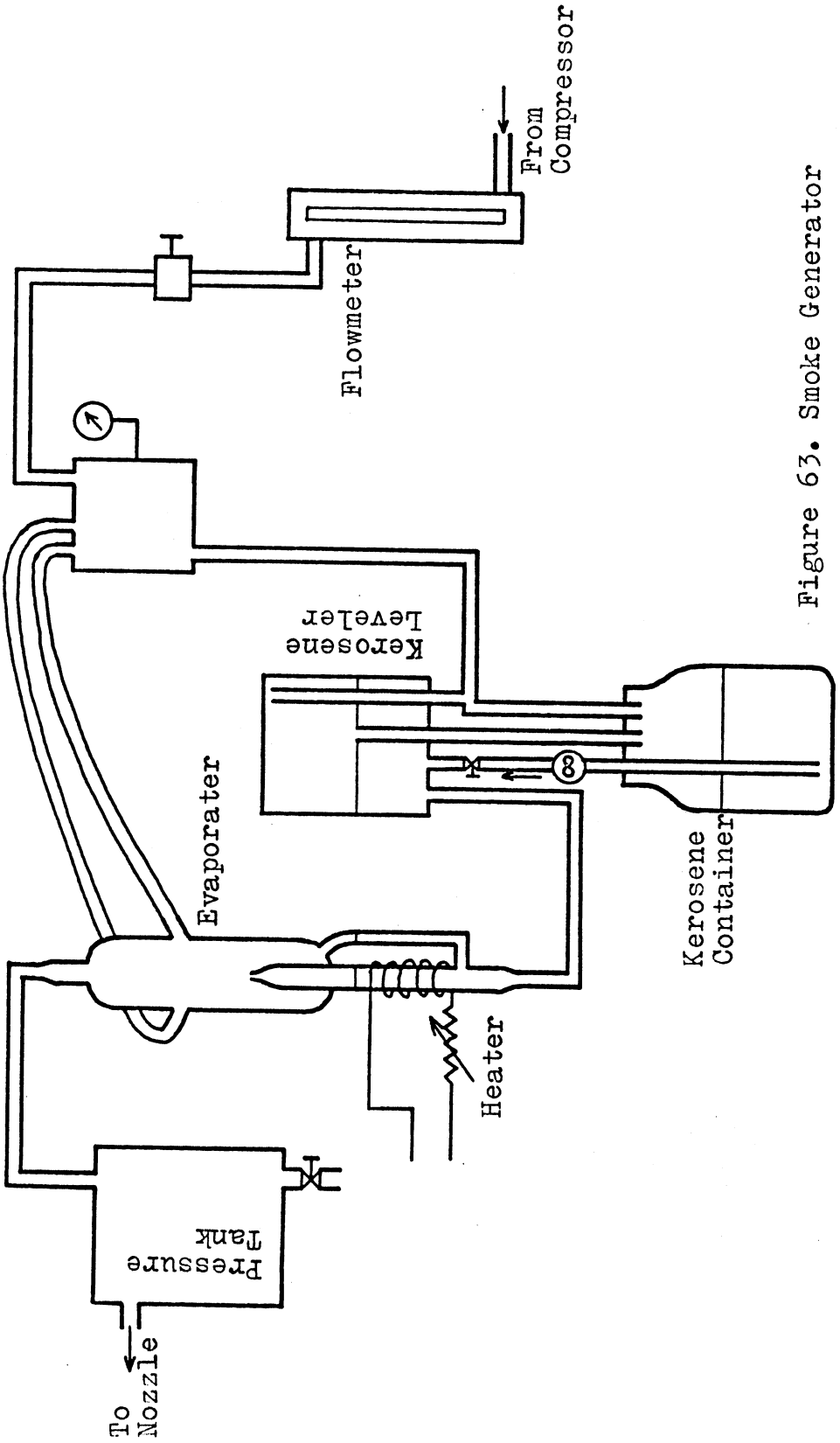

Figure 63. Smoke Generator

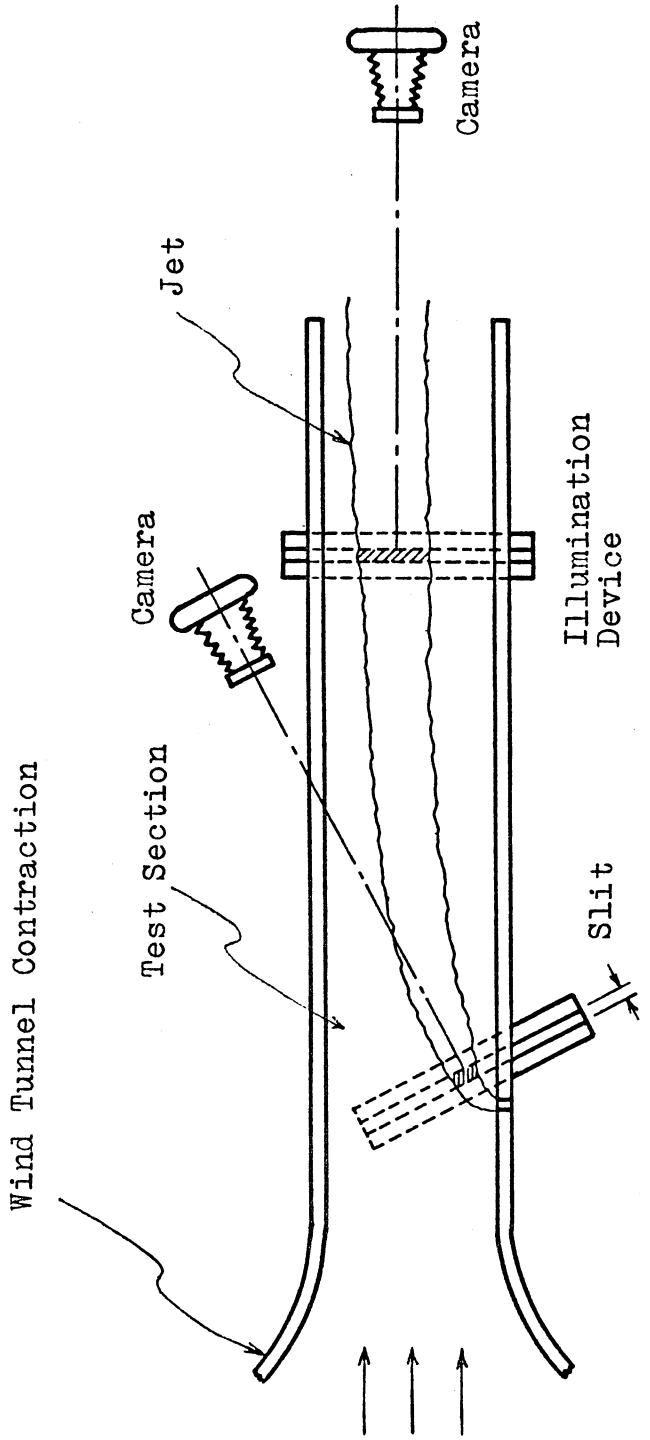

Figure 64. Photographic Arrangement

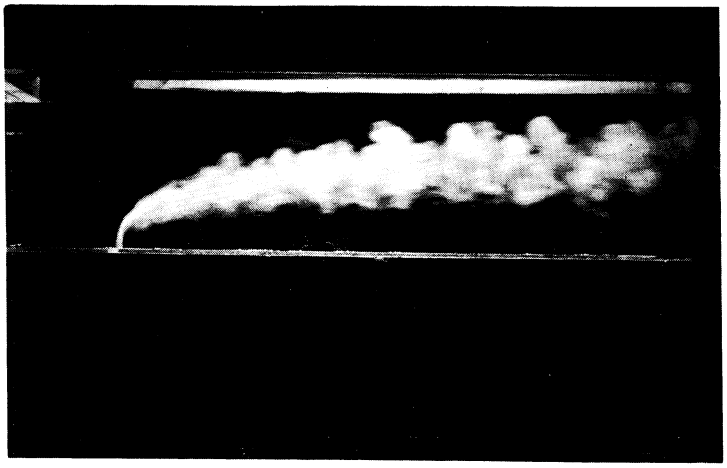

Figure 65. General View of Jet in Cross Flow

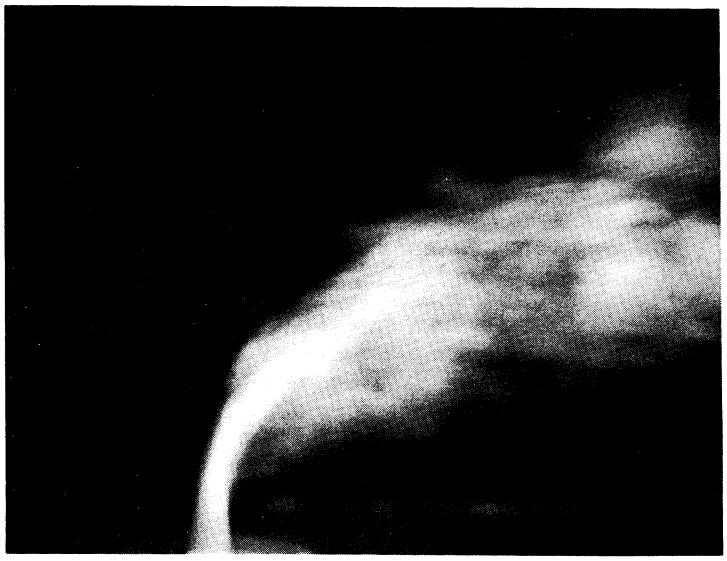

Figure 66. Close-up View

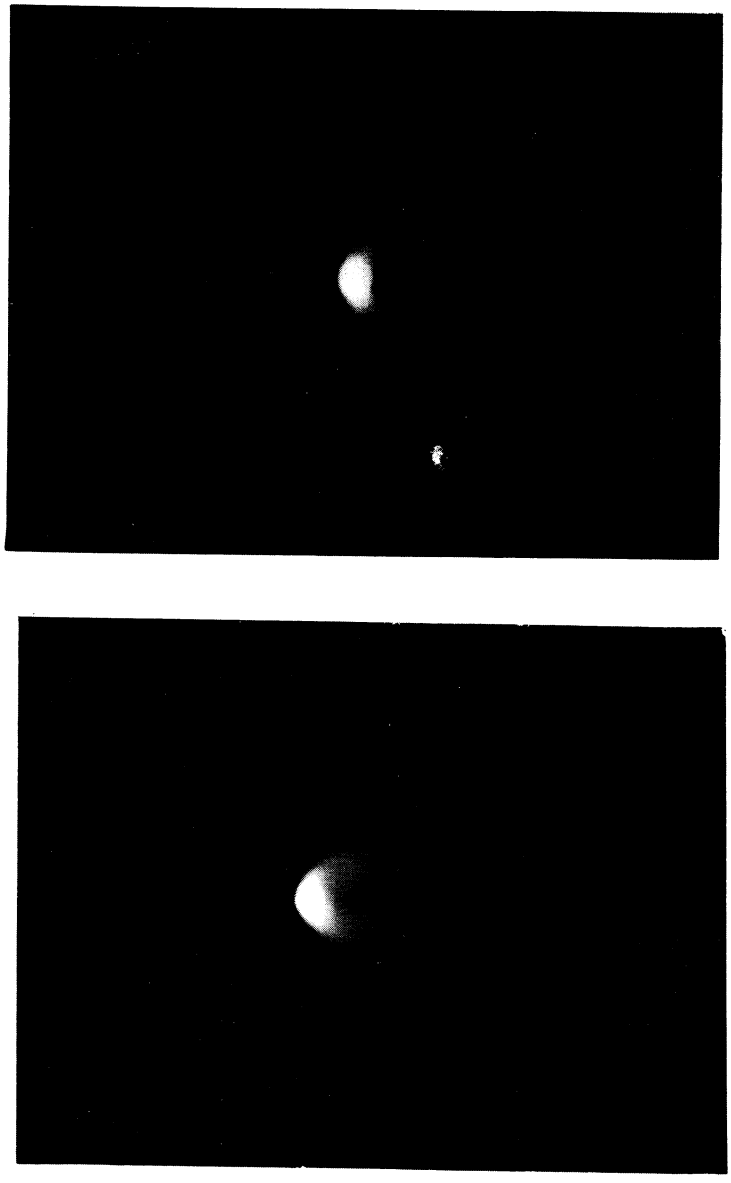

$R = 4,\ s/D = 2$

Figure 67. Jet Cross-section

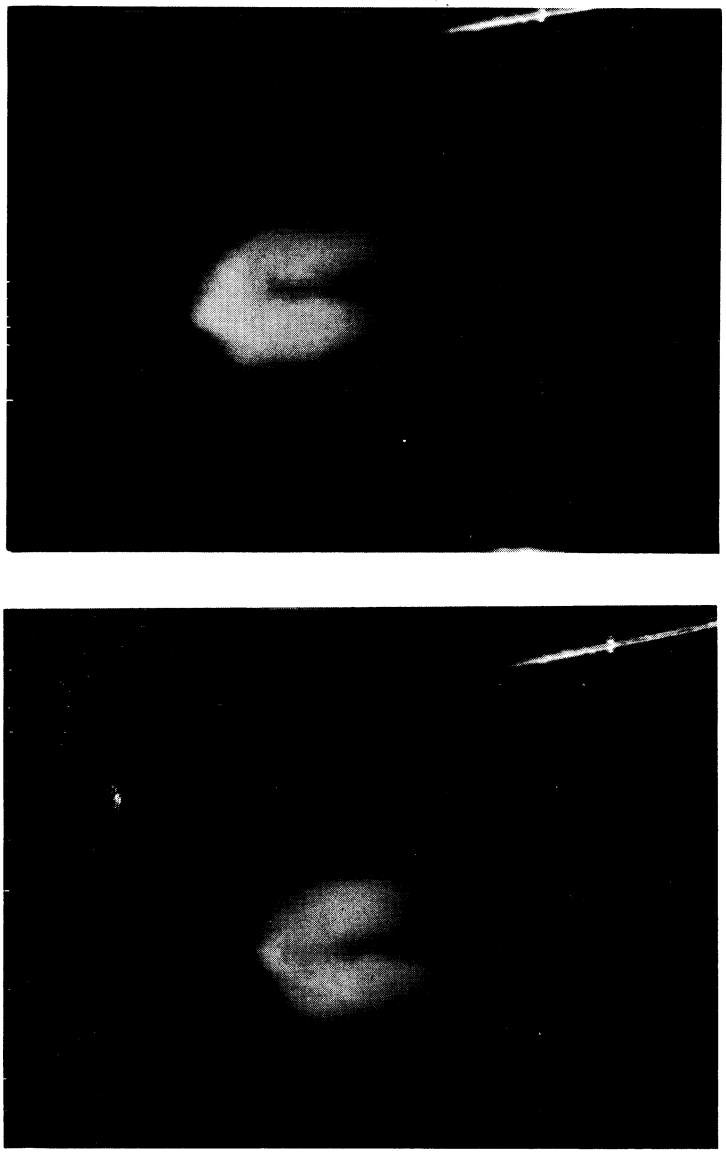

$R = 4,\ z/D = 5$

Figure 68. Jet Cross-section

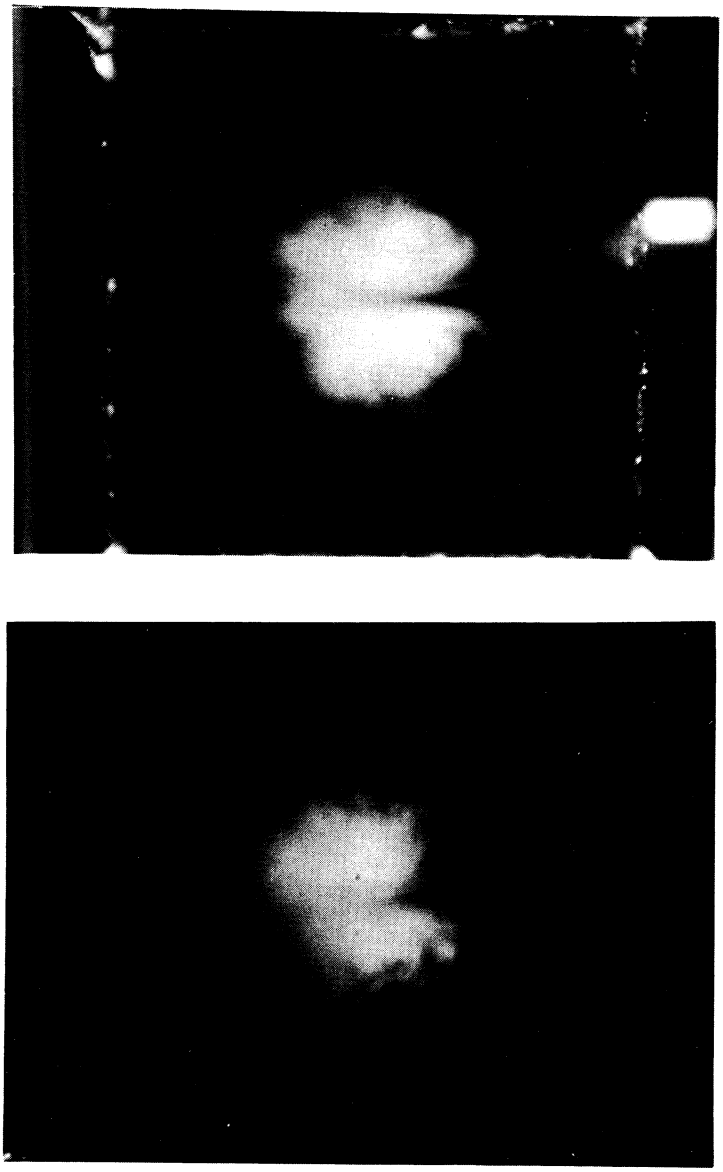

$R = 4,\ s/D = 20$

Figure 69. Jet Cross-section

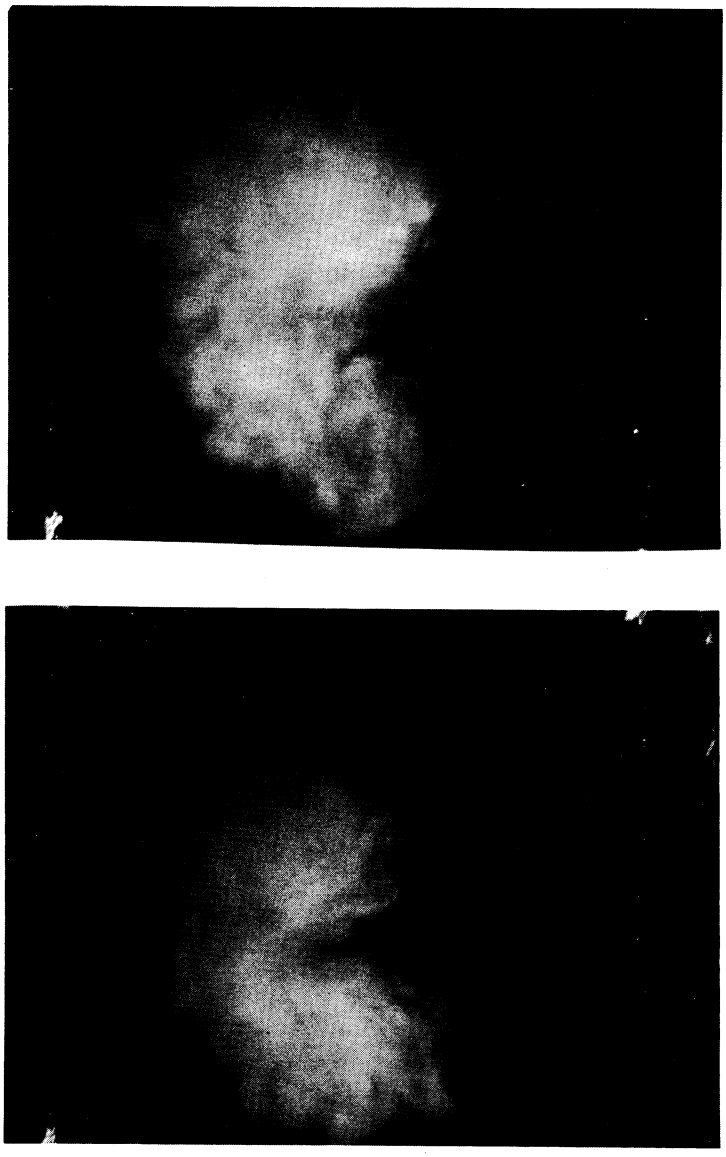

$R = 4, \; x/D = 70$

Figure 70. Jet Cross-section

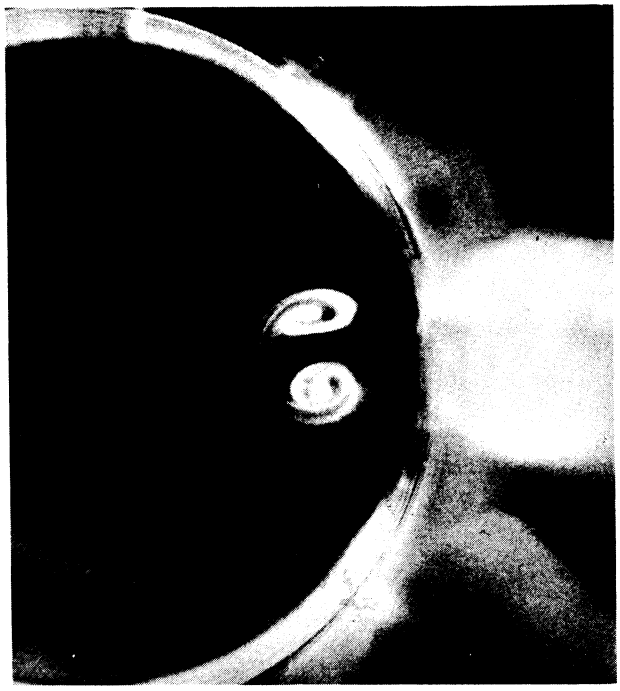

Figure 71. Vortex Motion in Laminar Jet

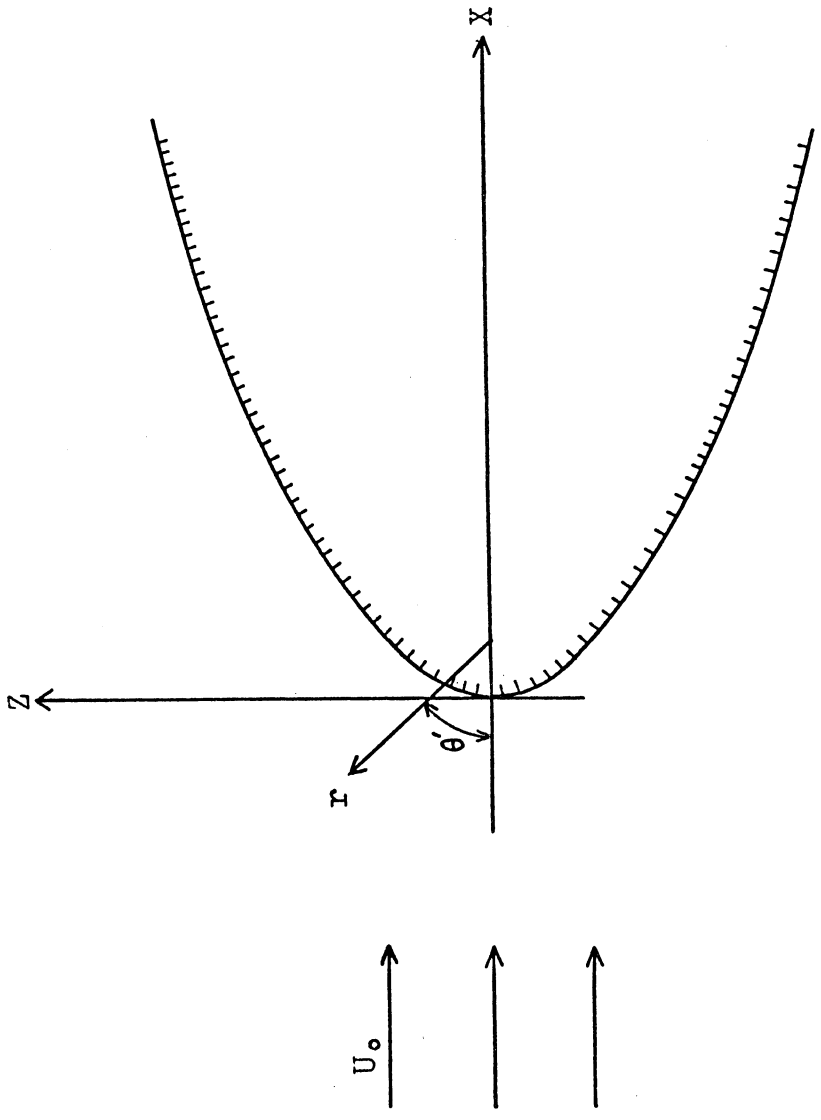

Figure 72. Coordinate System for Flow around Parabolic Cylinder

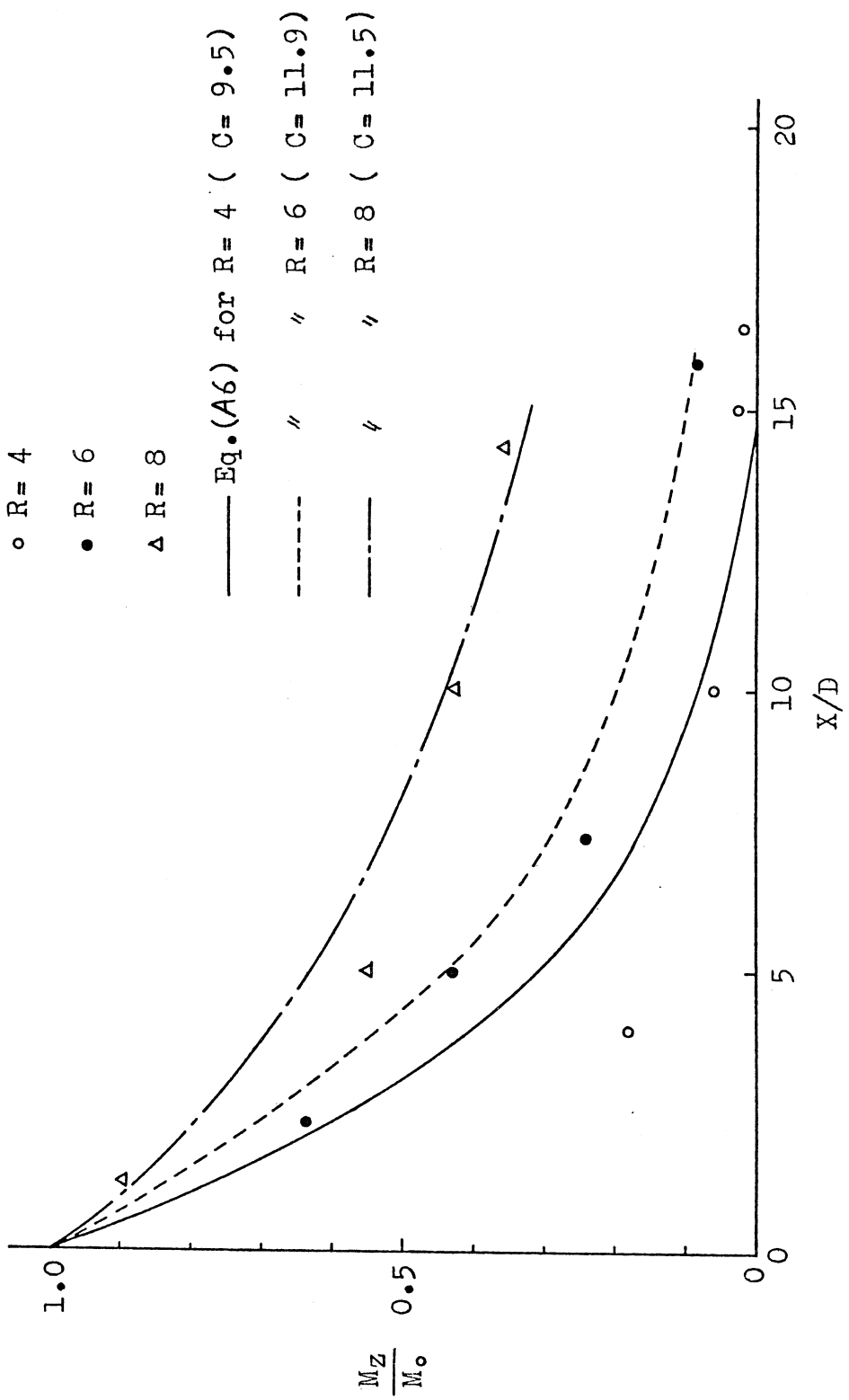

Figure 73. Z - Momentum Flux Distribution

R	$T_j - T_o$ (°F)	ρ_j/ρ_o	U_j/U_o	$\rho_j U_j^2/\rho_o U_o^2$	Re	F_r
4	0	1.00	3.91	15.3	1.62×10^4	———
	75	0.877	4.18	15.3	1.30	1.60×10^5
	320	0.625	4.95	15.3	0.95	0.52×10^5
8	0	1.00	7.73	59.6	2.14	———
	75	0.877	8.25	59.6	1.71	2.76×10^3
	320	0.625	9.77	59.6	1.25	1.27×10^3

$$Re = \frac{U_j D}{\nu} \quad , \quad F_r = \frac{U_j^2}{\beta g D (T_j - T_o)}$$

Table 1. Summary of Experimental Conditions

APPENDIX A

Pressure Force Acting on Jet in Cross Flow

There are two important effects which the jet gives to the cross flow. One is the entrainment effect, and the other is the blockage effect. The former has been explained in detail in Chapter VI. The latter situation is similar to the case in which a solid object is put in a uniform flow. The flow is disturbed by such an object, and the object itself experiences an aerodynamic drag. In the present experiments, the drag in the cross direction acts to deflect the jet, whereas the force in the Z-direction (the direction of jet injection) reduces the jet initial momentum. As has been explained in Chapter VI, the jet is deflected mainly by the entrainment effect in the far downstream region; however in the region near the nozzle the pressure drag is also important. The decrease of the jet initial momentum can be seen in Fig. 30. In order to explain the effect of the pressure force analytically, a simplified, two-dimensional potential flow model is considered here. Since the cross-section is very much flattened, a two-dimensional model seems to be not too bad an approximation.

Consider the potential flow around a parabolic cylinder which is set normal to the flow as shown in Fig. 72. Using the coordinate system in the figure, the cylinder is expressed by the equation

$$\frac{r}{a} = \sec^2 \frac{1}{2}\theta' \qquad \text{(A1)}$$

or

$$Z^2 = 4aX$$

where 2a is equal to the radius of curvature at $\theta' = 0$. The velocity potential is given by

$$\phi = -U_0 r \cos\theta' + 2U_0 a^{1/2} r^{1/2} \cos\tfrac{1}{2}\theta' \qquad \text{(A2)}$$

The pressure distribution on the surface of the cylinder is then

$$\begin{aligned} P - P_0 &= \tfrac{1}{2}\rho U_0^2 \cos^2\tfrac{1}{2}\theta' \\ &= \tfrac{1}{2}\rho U_0^2 \frac{a}{a+x} \end{aligned} \qquad \text{(A3)}$$

where P_0 is the pressure of the undisturbed flow. It is assumed that the nearly same pressure is acting on a suitably defined surface of the three-dimensional jet. To calculate the total pressure force acting in the negative z -direction, it is necessary to consider the projection of the jet on the xy -plane. According to the flow visualization experiment, the projected area has nearly a rectangular shape. Thus assume that the area is given by

$$S(x) = Cx \qquad \text{(A4)}$$

where the constant C represents the width of the rectangle, and its value is slightly different for the different momentum ratio. Therefore the total pressure force in the negative z -direction is

$$P = \int_0^x (p - p^*)\, ds$$

where p^* is the pressure in the wake region. Generally, $p^* \doteqdot p_0$. Then the jet initial momentum decreases as

$$M_z(x) = M_{j0} - P = M_{j0} - \tfrac{1}{2}\rho U_0^2 a \int_0^x \frac{ds}{a+x} \qquad \text{(A5)}$$

where $M_{j0} = \tfrac{1}{4}\pi D^2 \rho U_j^2$.

According to the profiles of the jet centerline

$$a \doteqdot \frac{R^2 D}{16} .$$

Consequently

$$\frac{M_z}{M_{j0}} = 1 - \frac{C}{8\pi} \ln\left(1 + \frac{16}{R^2}\frac{x}{D}\right). \qquad \text{(A6)}$$

Eq. (A6) is compared with the data in Fig. 73.

As can be seen in the figure the change of the vertical momentum flux nearly follows Eq. (A6). For R = 4, the agreement is not so good for small $\frac{x}{D}$ but this is mainly due to the method of calculating M_z. The value of M_z has been obtained by integrating $\rho \overline{U}^2$ in the arbitrarily defined jet region which is a rather small part of the whole turbulent region for R = 4 except in the region near the nozzle.

APPENDIX B

List of Symbols

A	;	a constant
C	;	a constant
D	;	nozzle exit diameter
D_T	;	eddy diffusivity
E, E_1, E_2	;	entrainment coefficients
$E(f)$	;	spectrum function of turbulence kinetic energy
F_r	;	Froude number
G	;	transfer function of hot wire amplifier
K, K'	;	constants
$M(\bar{x})$	;	total momentum flux of jet at $\bar{x}$
M_r	;	total momentum flux of jet at reference point
M_{j0}	;	total momentum flux of jet at nozzle exit
P, P_s	;	pressures
P_t	;	total pressure
P_1, P_2	;	pressures measured by yaw meter
P_r	;	Prandtl number
R	;	effective velocity ratio $\equiv (\rho_j U_j^2 / \rho_o U_o^2)^{\frac{1}{2}}$
Re	;	Reynolds number
$S(x)$	;	projected area of jet on xy -plane
S_T	;	cross-sectional area of turbulent region
$S_{1/2}$	;	area occupied by the contour $\bar{\theta} = 0.5$
T	;	temperature
T_c	;	maximum temperature in the plane of symmetry at a given jet section

T_{max}	;	maximum temperature at a given jet section
U	;	velocity
U_b	;	velocity at which turbulence-non-turbulence interface is moving
U_c	;	maximum velocity in the plane of symmetry at a given jet section
U_e	;	entrainment velocity
$\bar{U}_m$	;	velocity component in xz-plane
$\bar{U}_{max}$	;	maximum velocity at a given jet section
$\bar{U}_{meas}$	;	measured value of velocity by hot wire
$\bar{U}_n$	;	velocity component - normal to jet section
U_{on}	;	normal component of cross flow velocity
$\bar{U}_p$	;	parallel velocity components
V, V'	;	normal velocity components of kerosene particle
a	;	a constant
b	;	a constant
c_p	;	specific heat of air at constant pressure
$\overline{e^2_{out}}$	;	mean square output voltage of wave analyzer
f	;	frequency
Δf	;	filter bandwidth of wave analyzer
g	;	gravitational acceleration
k	;	heat conductivity of air
m	;	total mass flux of jet
m_r	;	total mass flux of jet at reference point
m_T	;	average mass flux in turbulent region
n	;	a constant

$\hat{n}$; unit vector normal to jet section

$\ell^{+}_{1/2}, \ell^{-}_{1/2}$; values of ζ (measured from temperature center in the plane of symmetry) at which temperature is equal to 1/2 ($\overline{T_c} + T_o$)

$\overline{q^2}$; twice kinetic energy of turbulence

$r_{1/2}$; half value radius $\equiv \left(S_{1/2}/\pi \right)^{\frac{1}{2}}$

r^* ; effective radius of the region occupied by the contour $\tilde{u}_n = 0.1$

r_T^* ; effective radius of turbulend region

S ; sensitivity of hot wire

u, v, w ; turbulence velocities

$\tilde{u}, \tilde{u}_n$; dimensionaless velocities

$$\tilde{u} \equiv \frac{\overline{U} - U_o}{\overline{U}_{max} - U_o}, \quad \tilde{u}_n \equiv \frac{\overline{U}_n - U_{on}}{\overline{U}_{n,max} - U_{on}}$$

(x, y, z) ; Cartesian coordinate system

z_o ; effective source of jet deflection

α' ; flow direction in xz-plane

β' ; flow direction in xy-plane

γ ; intermittency factor

γ' ; mean flow direction with respect to xy-plane

δ ; angle between $\overline{U}_p$ and parallel component of U_o

ε ; spreading angle of mixing layer of jet in cross flow

ε' ; difference between ε and ε_o

ω ; angle between yaw meter and mean flow direction

θ ; deflection angle of jet velocity centerline

$\bar{\theta}$; dimensionless temperature

$$\bar{\theta} \equiv \frac{\bar{T} - T_0}{\bar{T}_{max} - T_0}$$

μ ; dynamic viscosity

ν ; kinematic viscosity

ξ_0 ; location of jet virtual origin

ρ ; density

ρ' ; density fluctuation

τ ; similarity variable

$\phi(f)$; energy/cps of wave analyzer input voltage

(ξ, η, ζ) ; jet defined coordinate system

$\overline{(\quad)}$; time-mean value

subscript ; quantity of undisturbed cross flow

subscript ; quantity of initial jet

FINAL REPORT DISTRIBUTION LIST FOR NASA CR-72893 GRANT NGR 36-027-008

1. NASA-Lewis Research Center
   21000 Brookpark Road
   Cleveland, Ohio 44135

Attention:			
	Report Control Office	MS 5-5	1
	Technology Utilization	3-19	1
	Library	60-3	2
	Fluid Systems Components Division	5-3	1
	W. L. Stewart	77-2	1
	J. Howard Childs	60-4	1
	L. Schopen	77-3	1
	J. B. Esgar	60-4	1
	H. H. Ellerbrock	60-4	1
	W. T. Olson	3-16	1
	R. R. Hibbard	3-5	1
	J. F. Dugan, Jr.	501-2	1
	Seymour Lieblein	100-1	1
	R. E. Jones	60-6	1
	Jack Grobman	60-6	1
	Maj. R. C. Chaplin	501-3	1
	Lt. Col. G. S. Weden	500-317	1
	John S. Clark	60-6	1
	James D. Holdeman	60-6	10
	James A. Albers	100-1	1
	F. S. Stepka	60-6	1
	Robert S. Ruggeri	5-9	1

2. S. C. Fiorello
   Aeronautical Engine Laboratory
   Naval Air Engineering Center
   Philadelphia, Pennsylvania 19112 — 1

3. Aerospace Research Laboratory
   Wright-Patterson AFB, Ohio 45433
   Attention: Dr. R. G. Dunn — 1

4. NASA Scientific and Technical Information Facility
   P. O. Box 33
   College Park, Maryland 20740
   Attention: NASA Representative
   RQT-2448 — 6

5. FAA Headquarters
   800 Independence Avenue, S. W.
   Washington, D. C. 20533
   Attention: R. W. Pinnes SS-120 — 1
   Library — 1

6. NASA Headquarters
600 Independence Avenue, S. W.
Washington, D. C. 20546
Attention: N. F. Rekos (RAP) 1
W. H. Roudebush (RAA) 1

7. Department of the Army
U. S. Army Aviation Material Laboratory
Propulsion Division (SAUFE-PP)
Fort Eustis, Virginia 23604
Attention: J. White 1
E. T. Johnson 1

8. United Aircraft of Canada, Ltd
P. O. Box
Lonquenil, Quebec, Canada
Attention: Miss Mary Cullen 1

9. Air Force Office of Scientific Research
1400 Wilson Boulevard
Arlington, Virginia 22209
Attention: SREP 1

10. Defense Documentation Center (DDC)
Cameron Station
5010 Duke Street
Alexandria, Virginia 22314 1

11. Department of the Navy
Bureau of Naval Weapons
Washington, D. C. 20025
Attention: Robert Brown, RAPP14 1

12. Department of the Navy
Bureau of Ships
Washington, D. C. 20360
Attention: G. L. Graves 1

13. NASA-Langley Research Center
Langley Station
Technical Library
Hampton, Virginia 23365
Attention: Mark R. Nichols 1
John V. Becker 1
Richard J. Margajon MS 404 1

14. United States Air Force
Aero Propulsion Laboratory
Area B, Bldg. 18D
Wright-Patterson A.F.B.
Dayton, Ohio 45433
Attention: Robert E. Henderson — 1

15. United Aircraft Corporation
Pratt & Whitney Aircraft Division
400 Main Street
East Hartford, Connecticut 06108
Attention: G. Andreini — 1
Library — 1
R. Marshall — 1

16. United Aircraft Research
East Hartford, Connecticut
Attention: Library — 1

17. Detroit Diesel Allison Division
Department 8894, Plant 8
P. O. Box 894
Indianapolis, Indiana 46206
Attention: J. N. Barney — 1
G. E. Holbrook — 1
Library — 1

18. Northern Research & Engineering Corp.
219 Vassar Street
Cambridge, Massachusetts 02139
Attention: K. Ginwala — 1

19. General Electric Company
Flight Propulsion Division
Cincinnati, Ohio 45215 — 1
Attention: J. S. McBride — H-44 — 1
F. Burggraf — H-32 — 1
S. N. Suciu — H-32 — 1
C. Danforth — H-32 — 1
Technical Information Center — N-32 — 1
D. Bahr — 1

20. General Electric Company
1000 Western Avenue
West Lynn, Masachusetts 01905
Attention: Dr. C. W. Smith
Library Building — 2-40M — 1

21. Curtiss-Wright Corporation
Wright Aeronautical Division
Wood-Ridge, New Jersey 07075
Attention: D. Wagner 1
W. Walker 1

22. Air Research Manufacturing Company
402 South 36th Street
Phoenix, Arizona 85034
Attention: Robert O. Bullock 1

23. Air Research Manufacturing Company
9851 Sepulveda Boulevard
Los Angeles, California 90009
Attention: Dr. N. Van Le 1

24. AVCO Corporation
Lycoming Division
550 South Main Street
Stratford, Connecticut
Attention: Claus W. Bolton 1
Charles Kuintzle 1

25. Continental Aviation & Engineering Corporation
12700 Kercheval
Detroit, Michigan 48215
Attention: Eli H. Bernstein 1
Howard C. Walch 1

26. International Harvester Company
Solar Division
2200 Pacific Highway
San Diego, California 92112
Attention: P. A. Pitt 1
Mrs. L. Walper 1

27. Goodyear Atomic Corporation
Box 628
Piketon, Ohio
Attention: C. O. Langebrake 1

28. George Derderian AIR 53622 B
Department of the Navy
Bureau of the Navy
Washington, D. C. 20360 1

29. The Boeing Company
Commercial Airplane Division
P. O. Box 3991
Seattle, Washington 98124
Attention: G. J. Schott — MS 80-66 — 1

30. The Boeing Company
Missile and Information Systems Division
224 N. Wilkinson Street
Dayton, Ohio 45402
Attention: Warren K. Thorson — 1

31. Aerojet-General Corporation
Sacramento, California 95809
Attention: M. S. Nylin — 1
Library — 1

32. Cornell Aeronautical Laboratory
4455 Genessee Street
Buffalo, New York 14221 — 1

33. Marquardt Corporation
16555 Saticoy Street
Van Nuys, California — 1

34. Thompson Ramo Wooldridge
23555 Euclid Avenue
Cleveland, Ohio — 1

35. Aro, Incorporated
Arnold Air Force Station
Tennessee — 1

36. Prof. J. M. Beer
Dept. of Chem. Eng. & Fuel Tech.
University of Sheffield,
Mappin Street - Sheffield S1 3JD - Yorkshire
Great Britain — 1

37. Cummings Engine Co.
Cummings Technical Center
1900 McKinley Avenue
Columbus, Indiana 47201
Attention: Curt Dasbach
Mail Code 50142 — 1

38. Garrett/AiResearch Co.
402 South 36th Street
Phoenix, Arizona 85034
Attention: John M. Haasis — 1

39. Pratt & Whitney Aircraft
Florida Research & Development Center
Box 2691
West Palm Beach, Florida 33402
Attention: J. Chamberlain — 1
J. Dykslag — 1
J. Shadowen — 1
G. Lewis — 1

40. Professor A. H. Lefebre
The Cranfield Institute of Technology
Cranfield, Bedford
Great Britain — 1

41. Aerojet General Corporation
Sacramento Facility
P. O. Box 15847
Sacramento, California 95813
Attention: C. E. Tedmon — 1
Dave Kors — 1

42. Parker Hannifin Co.
17325 Euclid Avenue
Cleveland, Ohio 44112
Attention: Harold C. Simmons — 1

43. Eaton Yale and Towne Research Center
26201 Northwestern Highway
Southfield, Michigan 48075 — 1

44. Rocketdyne
North American Rockwell
6630 Canoga Avenue
Canoga Park, California 91304
Attention: S. D. Clapp
Manager
Propulsion Technology Research Division — 1

45. Dept. of Mechanical Engineering
201 Engineering Building
Michigan State University
E. Lansing, Michigan 48823
Attention: Dr. John F. Foss — 1
Mr. Stanley J. Kleis — 1

46. Mechanical Engineering Dept.
University of Minnesota
Minneapolis, Minnesota 55455
Attention: Prof. R. J. Goldstein 1
Mr. J. P. Bouchez 1